Development of a highly sensitive and versatile mass spectrometer system for laboratory and atmospheric measurements

Dissertation

zur Erlangung des Grades

Doktor der Naturwissenschaften (Dr. rer. nat.)

von

Sascha Albrecht

vorgelegt am

5. Juni 2014

an der

Das Leben ist eine lange Segeltour auf unruhigen Gewässern. Ich danke allen die während dieser Doktorarbeit mit mir unterwegs waren und geholfen haben den Kurs zu halten, bei Wind und Wetter.

Mein herzlichster Dank gilt ...

- Dr. Fred Stroh, mein Betreuer, der viele abwegige Ideen, nicht ganz so abwegig fand und geholfen hat die besten Ideen um zu setzen.
- Prof. Dr. Thorsten Benter, mein Doktorvater, der mich und meine Arbeit inspiriert hat.
- Prof. Dr. Martin Riese, der das Institut auf Kurs hält und auch meine Stelle bewilligt hat.
- Jochen Barthel, der viel Zeit in die mehr als erfolgreiche Konstruktion der CIMS Transferstufe investiert hat und immer ein offenes Ohr für andere Belange hatte.
- Heinz Rongen und Markus Dick, die die Elektronik für die beiden Ionenfunnel realisiert und optimiert haben.
- Prof. Dr. Astrid Kiendler-Scharr, die mir als interne Mentorin sehr hilfreiche Ratschläge gegeben hat.
- “Lee” Mauldin, der als externer Mentor zur Verfügung stand.
- Vicheith Tan, der immer ein offenes Ohr für Fragen zur Elektronik hatte.
- Armin Afchine, der sich die Zeit genommen hat die fluiddynamischen Rechnungen zu modellieren.
- Joachim Borchardt, der so nett war mir das Elektrometer zur Verfügung zu stellen.
- Meinen Mitdoktoranden am Forschungszentrum Jülich und an der Uni Wuppertal, die ich nicht alle aufzählen kann, mir aber doch ans Herz gewachsen sind.

- Valerie Derpmann, Sebastian Klopotowski, Walter Wissdorf, Hendrick Kersten, Klaus Brockmann und Sonja Klee, mit denen ich sehr erfolgreiche Diskussionen im “Cafe Brockmann” geführt habe.
- Sarah Peters, Saskia Springmann, Sascha Liedtke und Nicole Karpensky, die mit mir das Büro an der Uni geteilt haben und viel Abwechslung in meinen Alltag gebracht haben.
- Marc von Hobe, mit dem ich das Büroteilen durfte, vor allem fürs aufrecht Erhalten der Kaffeepause.
- Ronald Giese, der mit mir das “ClusterTOF” realisiert hat und mit seiner jahrelangen Erfahrung eine Bereicherung bei der Konstruktion war.
- Den Mitarbeitern der dem Institut angeschlossenen Werkstatt, der Hauptwerkstatt des Forschungszentrums und der Werkstatt der physikalischen Chemie Wuppertal, die Blut und Schweiß in die Fertigung der Transferstufen gesteckt haben.
- Der physikalischen Chemie, die mich das erste Jahr meiner Arbeit aufgenommen hat.
- Dem Institut IEK-7: Stratosphärenchemie, bzw. Allen die es bevölkern und mit Leben füllen.
- und natürlich meinen Eltern, die mich immer bestärkt haben meinen Weg zu gehen.

Abstract

Trace gases in the upper troposphere and the lower stratosphere (UTLS) strongly influence our climate and even can affect tropospheric weather. Therefore a better understanding of the processes governing trace gas distributions and transport is crucial. Sensitive and accurate atmospheric measurements are thus essential to improve and verify Chemical Climate Models (CCM's) and ultimately enable more reliable forecasts of future climate.

Two especially important trace gases in the UTLS are sulphuric acid, H_2SO_4 and its precursor SO_2. Although H_2SO_4 is present at sub-ppt mixing ratios it plays a central role in the formation of the stratospheric aerosol layer, which is a crucial component of the global radiative budget [52]. Very selective and sensitive measurements of H_2SO_4 and many other trace species are possible using mass spectrometers in combination with chemical ionization (CI) at atmospheric pressure (AP). However, to reach a favorable detection limit, improvements of the ion source and the ion transfer stages are needed. Therefore the ion transmission through each transfer element needs to be optimized. Additional sensitivity may be gained using a "brilliant" ion source.

The cluster chemistry in the ion source and transfer stage plays an important role for the sensitivity and the reliability of the measurement. In order to gauge the impact of cluster chemistry a transfer stage was developed that provides realistic mass spectrometer measurements of ion bound clusters and their reactions in the ion source. This transfer stage with tunable electrostatic fields provides full control of the ion energy, to the extent that additional reactions, induced by heating the ions in electrostatic fields, can be prevented.

A thermally sampling atmospheric pressure ionization mass spectrometer has been constructed. The ion transfer stage offers the capability to sample cluster ions at thermal equilibrium. Fundamental processes in the transfer stage possibly affecting the cluster distribution can be readily identified. The performance of the setup is demonstrated with regard to the proton-bound water cluster system. The omnipresent water cluster chemistry occurs in every AP ion source and is also part of most AP CI reaction cascades. The transfer stage combines optional collision induced dissociation (CID) analysis of the

cluster composition with thermal equilibrium sampling of clusters. Further on, the instrument allows the identification of fragmentation and protonation reactions caused by CID. The observed processes help to design and improve transfer stages and to understand cluster ion reactions in ion mobility tubes and atmospheric pressure ion sources.

For highly sensitive atmospheric trace gas measurements a prototype chemical ionization mass spectrometer was constructed from a chemical ionization mass spectrometer (CIMS) transfer stage optimized for high transmission and a brilliant dielectric barrier discharge (DBD) ion source. A new transfer stage concept using two ion funnels was developed. The first ion funnel is working at 100 hPa. To our knowledge, no other CIMS has been reported with an ion funnel working at such an high pressure. At this pressure it allows to perform the chemical ionization of the analyte directly in the ion funnel and enables a higher gas throughput, which leads to an efficient ion transfer and high sensitivity. Ions are picked-up by a second ion funnel working at 5 hPa, which also provides high transmission. Further downstream a segmented quadrupole at 10^{-2} hPa focus the ion stream into the mass spectrometer. The transfer elements are configured employing combined fluid dynamic and electrostatic simulations using Ansys CFX and Simion. To further improve the detection limit of the instrument a brilliant ion source employing a dielectric barrier discharge has been developed and optimized. It replaces the logistically very challenging standard radioactive ion source. The prototype instrument has been tested and characterized and provides the basis for the development of an highly sensitive airborne instrument.

Zusammenfassung

Spurengase in der oberen Troposphäre und unteren Stratosphäre (UTLS) beeinflussen entscheidend unser Klima und haben Einfluss auf das Wetter in der Troposphäre. Daher ist es nötig, die zentralen Prozesse der Verteilung und des Transports der Spurengase zu verstehen. Hierzu werden empfindliche und genaue atmosphärische Messungen benötigt, um Chemie-Klimamodelle (CCMs) zu überprüfen, zu verbessern und so verlässliche, langfristige Klimaprognosen zu ermöglichen.

Eins der wichtigsten Spurengase in der UTLS ist die Schwefelsäure, H_2SO_4. Obwohl sie nur in sub-ppt Mischungsverhältnissen vorliegt, spielt sie eine wichtige Rolle bei der Aerosolbildung in der Stratosphäre, die das Strahlungsbudget der Erde entscheidend beeinflusst. [52] Sehr selektive und sensitive Messungen der Schwefelsäurekonzentration und vieler anderer Spezies sind mit der Kombination von chemischer Ionisation (CI) bei Atmosphärendruck und einem Massenspektrometer (MS) möglich. Um die bestmöglichen Nachweißgrenzen zu erreichen, ist die Optimierung der Ionenquelle und der Ionentransferstufe unerlässlich. Hierzu wird die Transmission eines jeden Transferelements optimiert. Zusätzliche Gewinne bei der Sensitivität können durch die Nutzung einer brillanten Ionenquelle erzielt werden.

Auch die Clusterbildung und Ionenchemie in der Ionenquelle spielt eine entscheidende Rolle für die Sensitivität und die Zuverlässigkeit der Messung. Dazu wurde eine Transferstufe entwickelt, die die Ionencluster und ihre Reaktionen realistisch abbildet. Diese Transferstufe ermöglicht es, die Stärke der elektrostatischen Felder zu regeln, um die Energie der Ionen gezielt zu steuern. So können Reaktionen vermieden werden, die durch die Zufuhr von kinetischer Energie durch elektrostatische Felder verursacht werden. Zu diesem Zweck wurde eine Transferstufe entworfen, die eine Probennahme von Ionenclustern im thermischen Gleichgewicht ermöglicht. Fundamentale Prozesse, die die Ionenclustergrößenverteilung beim Transfer beeinflussen, wurden identifiziert. Die Leistungsfähigkeit dieser Transferstufe wurde charakterisiert, wobei der Schwerpunkt der Betrachtung auf protonengebundenen Wasserclustern lag. Die Wasserclusterchemie ist in in jeder Atmosphärendruck-Ionenquelle (API)

vorzufinden, und daher Teil vieler chemischer Ionenreaktionen. Um die im thermischen Gleichgewicht gesammelten Ionen zu identifizieren, kann optional die kollisionsinduzierte Dissoziation (CID) genutzt werden. Mit den gesammelten Informationen zur CID können zudem Fragmentierungs- oder Protonierungsreaktionen identifiziert werden. Die beobachteten Prozesse können genutzt werden, um zukünftige Transferstufen zu verbessern und um Clusterreaktionen bei Ionenmobilitätsmessungen oder in APIs besser zu verstehen.

Um empfindliche atmosphärische Spurengasmessungen zu ermöglichen, wurde zusätzlich ein Prototyp für ein Massenspektrometer mit chemischer Ionisation (CIMS) konstruiert. Die Transferstufe wurde auf hohe Transmission optimiert. Hierzu wurde ein neues Transferstufen-Konzept entwickelt, das mit zwei Ionentrichtern arbeitet. Der erste Ionentrichter wird bei 100 hPa betrieben. Nach unserer Kenntnis wurde noch kein CIMS Gerät beschrieben, das einen Ionentrichter besitzt, der bei solch hohem Druck betrieben werden kann. Bei 100 hPa kann die chemische Ionisation direkt im Ionentrichter durchgeführt werden. Somit können die Primärionen direkt in das erste Transferelement gegeben und höhere Gaslasten bewältigt werden. Dies ermöglicht eine sehr hohe Empfindlichkeit. Darauf folgt ein zweiter Ionentrichter der bei 5 hPa betrieben wird. Bei 10^{-2} hPa wird der Ionenstrahl mit einem segmentierten Quadrupol gebündelt und dem MS zugeführt. Design und Optimierung der Transferstufe erfolgten durch die Kombination von strömungsdynamischen Rechnungen, anhand des Ansys CFX Programmpakets und elektrostatischer Simulationen mit Kollisionsmodellen anhand des SIMION Programmpakets. Zur weiteren Steigerung der Empfindlichkeit wurde eine brillante, dielektrische Plasmaentladungs-Ionenquelle entwickelt und optimiert. Diese ersetzt die bisherige radioaktive Ionenquelle, die ein Sicherheitsrisiko darstellt und beim Transport erhebliche logistische Probleme bereitet. Der Prototyp wurde getestet, charakterisiert und ist die Grundlage für die Entwicklung eines hoch sensitiven, flugzeuggetragenen Instruments.

Table of Contents

List of Figures

List of Tables

List of Acronyms

AC alternating current

AP atmospheric pressure

API atmospheric pressure ionization

APLI atmospheric pressure laser ionization

APPI atmospheric pressure photo ionization

CI chemical ionization

CID collision induced dissociation

CIMS chemical ionization mass spectrometry

DA dopant assisted

DBD dielectric barrier discharge

DC direct current

DPSS diode pumped solid state

EI electron ionization

Fig figure

GND ground

HPLC high pressure liquid chromatography

HV high voltage

ID inner diameter

IR infrared

m/z mass to charge ratio

MCP multi channel plate

MS mass spectrometer

PEEK polyether ether ketone

REMPI resonance enhanced multi photon ionization

RF radio frequency

TIC total ion count

TOF time of flight

UTLS upper troposphere and lower stratosphere

UV ultraviolet

VUV vacuum ultraviolet

Chapter 1

Introduction

1.1 Atmospheric background

Trace gases in the atmosphere with mixing ratios of ppmv to ppqv can have global impact. A prominent example is the OH-radical (with approximately 0.1 pptv mixing ratio), which oxidizes the bulk of organic trace gases in the troposphere [53]. Another example are organic bromine species (in total approximately 20 pptv) that can cause up to 30 % of the total ozone loss in the stratospheric ozone hole [120]. Trace gases in the upper troposphere and lower stratosphere (UTLS) strongly couple to climatic change and can affect tropospheric weather [114, 124]. Therefore a better understanding of the processes governing trace gas distribution and transport are needed. This offers the opportunity to improve and verify atmospheric models and to enable more reliable forecasts of a future climate.

Two other highly discussed trace gases in the UTLS are sulphuric acid, H_2SO_4 and its precursor SO_2 [45]. They play a central role in the formation of the stratospheric aerosol layer, which is a crucial component of the global radiative budget. Current topics are formation of the Junge layer [57], geoengineering [e.g., 110], impact of the Asian monsoon [e.g., 11], volcanic aerosol [e.g., 132] and polar stratospheric clouds [e.g., 120]. The particles generated can be carried up to the mesosphere and also change the concentration of e.g. sulfuric acid in the troposphere by sedimentation [113]. For a better understanding of these processes in-situ measurements are of high importance. Only few flight campaigns with in-situ sulfuric acid measurements have been performed in the

past 20 years) [92, 21, 148, 147].

1.2 Airborne time of flight-mass spectrometers

The typical airborne mass spectrometers are equipped with a quadrupole mass analyzer. There are fully characterized setups, which can be operated at relatively high background pressure compared to e.g. time of flight (TOF) instruments. A quadrupole has a duty cycle of up to 100 % when only one specific mass is monitored but the duty cycle scales inversely with the number of masses analyzed. The TOF can analyze a broad range of masses at once, typically a number of ions is analyzed in each time step. The duty cycle of a TOF instrument is typically 10 to 20 %.

To analyze the time of flight of the ions a flight path without collisions is needed. The TOF analyzer is thus operated at pressures below 10^{-6} hPa. Therefore an additional transfer element is needed compared to the quadrupole analyzer which can be operated at up to 10^{-4} hPa.

In the last years TOF instruments have been miniaturized, e.g., the Tofwerk AG (Thun, Switzerland) offers a small TOF ("CTOF") of the size of a shoe box with a mass resolution of 800. Additionally, the TOF offers much better diagnostics of the ion chemistry, since several product ions (and related ions) are measured in parallel.

1.3 Chemical Ionization

Chemical ionization mass spectrometry (CIMS) enables sensitive and selective measurements of gaseous analytes. CIMS uses dopant ions to initiate reaction cascades resulting in specific thermodynamically controlled product ion distributions measured in the mass spectrometer (MS). The presented work is the initiation of the development of an airborne CIMS instrument for measurements in the UTLS. Therefore stratospheric analytes, e.g. H_2SO_4, OH, SO_2, HNO_3, etc. are of special interest. A universal high transmission transfer stage and an improved ion source are presented. The instrument performance is characterized employing a laboratory prototype. Future research includes the development of an online calibration and the modification and integration

to the aircraft.

Two complete transfer stages are developed and characterized. The first transfer stage provides thermal sampling of clusters and is used for the analysis of the complex cluster chemistry in the ion source. The second transfer stage is developed for high transmission and will be used for measurements at the detection limit. Chemical ionization will be used in combination with the second transfer stage, while the first transfer stage will help to understand the reaction cascade in the ion source. Additionally the first transfer stage can help to identify new detection schemes for atmospherically relevant analytes. Relatively new and selective dopants for the chemical ionization (e.g. I^-, CO_3^-) are discussed that are promising for the measurement of species such as NO_3, SO_2, HCN and BrO.

At atmospheric pressure (AP) conditions ion-molecule-reactions, e.g. charge transfer, addition, and substitution, are inevitable, thus they represent important processes to understand and optimize AP ion sources. One of the most important but often neglected process is the formation of ion bound clusters by polar species, in particular the omnipresent water molecules, with both negative and positive ions [59]. Siegel et al. reported the detection of water ion clusters in a MS operated with high purity nitrogen containing only a few ppmv of water [126]. Under no circumstances this clustering should be neglected since important thermodynamic parameters as proton affinities deviate significantly from the bare ions to the corresponding ion bound clusters. For instance, the proton affinities of water clusters, often used as reactants in atmospheric pressure ionization (API), have been shown to increase with the number of coordinated water molecules [59, 76]. Therefore the role of ion cluster formation in AP ion sources must be reasonably well understood in order to correctly interpret the measured mass spectra and optimize the ion source performance. This is especially true with respect to quantitative analysis.

The size distribution of water clusters and ion clusters adjusts fast to the local temperature, electrical fields and concentration changes. Modern API instruments always lead to energetic collisions, particularly in intermediate-pressure regions. A voltage difference of only 20 V between the skimmers in the presented instrument causes the dissociation of the water clusters. Such features are calling for a well characterized thermally sampling instrument for

further investigations.

The minimum transit time of ions from an AP ion source to the collision-free region is of the order of tens of ms resulting in at least 10^7 collisions of individual ions with background molecules [63], offering enough time to generate a thermal equilibrium distribution of the clusters. In order to avoid congested mass spectra induced by cluster formation most API MS purposefully employ electric fields to push ion cluster equilibria toward the bare ions by collision induced dissociation (CID) on passage through the pressure reduction stages [13]. CID increases the ion temperature [106] and thus may induce further reactions in combination with the destruction of clusters. A further increased ion temperature results in the fragmentation of ions [16]. However, this affects the transmission efficiency of the analyzer and may lead to cross-sensitivities on the calibration factor in quantitative analysis. The present setup potentially gives us further insights of the chemistry driven in the CIMS instruments. Especially clustering reactions and dissociation reactions driven by electrical fields are important details of the reaction cascade of the CIMS process.

The performance of this setup is demonstrated with regard to the proton-bound water cluster system. A study of the role of cluster formation in negative ion MS, employing the ion optics and MS analyzer presented here, was published by Derpmann et al. [24]. Further cluster chemistry observed in the positive mode measurements is discussed by Klee et al. [68]. The fundamental processes in the instrument have recently been published [1] and are likewise discussed in chapter 3.

1.4 Structure of the Thesis

An introduction to the topic of CIMS is given in chapter 2 where also the general stages of the mass spectrometer are discussed. Consideration has been given to various aspects improving the performance of a mass spectrometer, which are dealt within the next three chapters: In chapter 3 the performance of the thermodynamic equilibrium cluster transfer stage is demonstrated, which is a potent tool for analyses of the ion chemistry in the ion source. Chapter 4 is about the inlet and the ion source of the CIMS instrument, which is a prototype for the flight instrument. Finally chapter 5 characterizes the CIMS transfer

stage, which uses a new transfer concept, before the results are summarized in chapter 6.

Chapter 2

Fundamentals of chemical ionization mass spectrometry

Figure 2.1 shows a scheme of the typical CIMS instrument. The instrument consists of an ion source, where ions of a specific species are generated, also termed “dopant”. The dopant reacts with the analyte to generate analyte-ions. In the downstream transfer elements the ions are concentrated while the neutral gas molecules are pumped away. Because mass analyzers need low pressure the transfer stages are needed. Typical mass analyzers are e.g. time of flight-, quadrupole-, or ion-trap-mass spectrometers.

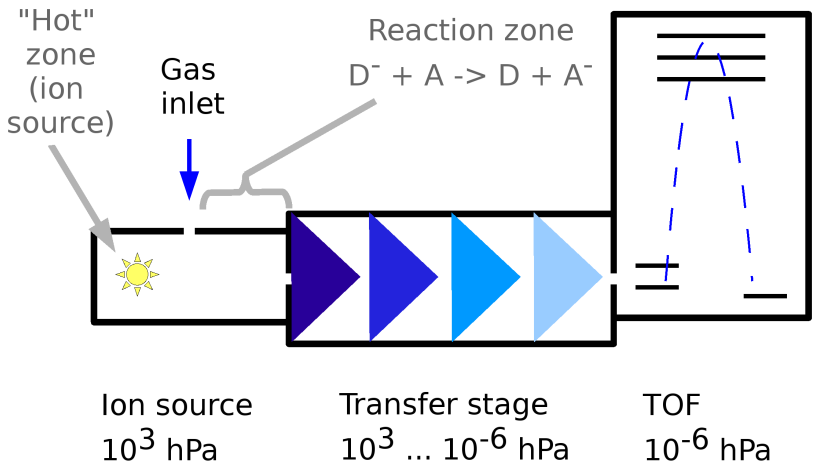

Figure 2.1: A schematic drawing of a chemical ionization (time of flight) mass spectrometer.

2.1 Mass spectrometeric domains

The general CIMS can be broken down into five domains, which will be discussed in this section.

Domain 1: The "hot" domain of ion generation

In the ion source highly energetic species, such as metastables, α- or β-particles, produce ions. In some ion sources electrons, for example, generated in a plasma or light (UV- or VUV-light) are used to generate the ions. Light may also be produced as byproduct in a plasma from excited state atoms or molecules. These processes often generate ions in most cases primary ions of highly abundant molecules in the gas phase are produced, e.g. N_2^+ and O_2^- in air.

Domain 2: Atmospheric pressure ion chemistry

Only a short distance away from domain 1 the ions and radicals produced relax to their electronic ground state and the primary ions react with the trace gases to thermodynamically more stable ions and ion clusters. The addition of a dopant can drive the ion chemistry to a specific ion or a group of specific ion clusters. The charge is thus collected by the dopant ions and a defined ion chemistry is possible. In the optimum case this ion chemistry equilibrates to a high concentration of specific analyte ions or analyte ion clusters, which allows sensitive measurements. The described ion chemistry is thermodynamically driven.

Domain 3: The expansion

Pressure reduction is done by nozzles or capillaries. At the outlet of the sampling nozzle or capillary the pressure is lower by a few orders of magnitude, so an expansion forms. In the expansion the thermal energy is transferred into kinetic energy and upon adiabatic cooling comparably large ion clusters can form. Depending on the distance between this outlet and the next nozzle a Mach disk forms at the end of the collision free region of the expansion. Here the ion clusters collide with the background gas and are partly dissociated and

recombine. If the time and pressure downstream of the nozzle is sufficient a thermal equilibrium cluster distribution can be established.

Domain 4: Ion activation by electrostatic fields

The thermal cluster distribution is disturbed by electrostatic fields, which are used to guide the ions along the transfer elements while the neutral gas molecules are pumped away. An alternative is a sampling without electrostatic fields but this results in a high loss of ions. If electrostatic fields are present ions are accelerated and gain additional kinetic energy, which may induce reactions upon the next collisions at pressures higher than 10^{-5} hPa. So electrostatic fields add additional energy to the ion system, which may lead to further reactions and cluster breakdown.

Domain 5: Collision free flight

Below 10^{-5} hPa only few collisions are present because the mean free path is increasing to several meters. Without collisions also the domain of ion chemistry ends. So TOF analyzers are typically operated below 10^{-6} hPa where collisions on a flight path of meters become unlikely.

2.2 The time of flight mass analyzer

The time of flight mass spectrometer accelerates a package of ions by an orthogonal ion extractor also termed "pulser", see figure 2.2. The ions are injected into the flight tube onto a flight path with a defined length l. The velocity of the ions is a function of the mass m of the ions because the ions are in first approximation accelerated to a defined kinetic energy E. Using the time of flight t from the pulser to the multi channel plate (MCP) detector the mass of the ions is calculated using equation 2.1.

$$m = 2\,E\left(\frac{t}{l}\right)^2 \tag{2.1}$$

The MCP, which is labeled as "detector" in figure 2.2, is a plate of capillaries oriented in the direction of the ions flight path. The surface of the capillaries provides a high emission of secondary electrons if an ion or electron collides

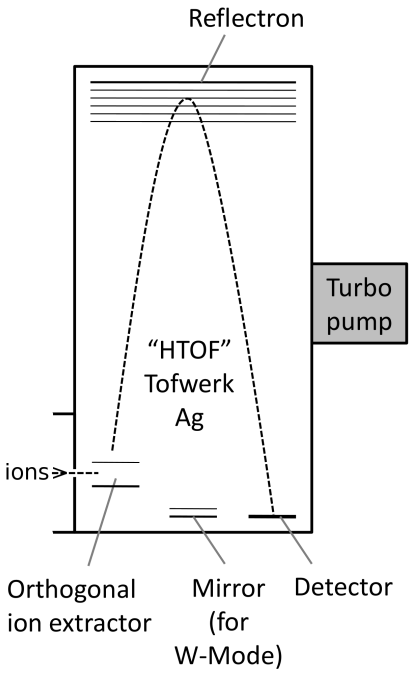

Figure 2.2: A schematic drawing of a time of flight mass spectrometer.

with the surface with sufficient energy. Through this electron multiplication a current pulse can be measured by a fast data acquisition system anytime an ion hits the MCP.

The minimum mass difference that can be resolved is limited by the data acquisition accuracy and (as in most mass spectrometers) by the accuracy of the initial flight velocities of the ions and differences in the flight path length by different starting points. The mass resolution R is defined as the measured mass divided by the minimum mass difference. The minimum mass difference of two peaks separated by a valley, is defined by the height of the valley, which is 50 % of the smallest peak height. With a mass resolution ($m/\delta m$) of 1000 masses 999 and 1000 or masses 1998 and 2000 can be distinguished.

To increase the mass resolution of the TOF frequently a reflectron is used. The reflectron is an ion mirror that provides an electrostatic field that increases from the entrance to the rear electrode. Depending on the energy of the ion it penetrates a variable distance into the reflectron and is reflected. So the spread of kinetic energy of the ions that results in different times of flight is compensated by the penetrate depth and the mass resolution is increased.

For the presented work a "HTOF" delivered by the Tofwerk AG, Thun, Switzerland is used. The "HTOF" time of flight mass spectrometer detects masses in the mass to charge ratio (m/z)-range >14 up to 750. With an electron ionization (EI) source even m/z 14 was detected with high intensity. All measurements presented here were obtained employing the V-mode, as shown in Fig. 2.2 with a mass resolution of 2500 [149].

2.3 Mass spectrometer assemblies

Two different custom made transfer stages have been combined with the "HTOF". The first assembly has been constructed for reactive and fragile molecules and clusters. It enables measurements of thermal equilibrium cluster distributions. This assembly is addressed in chapter 3.2. The second assembly is a high transmission transfer stage. This assembly is described in detail in chapter 5.2 and is a prototype for a flight instrument to be build in the future. It is dedicated to sensitive CIMS measurements.

Some parts of these assemblies are similar and are described in the following chapters. The transfer elements are numbered from 1 to 3 in the first assembly, where 1 is the transfer element behind the inlet and 3 is the transfer element upstream of the TOF analyzer. Since the second assembly has one more transfer element, the numbering starts at 0, which is the ion funnel driven at 100 hPa.

2.3.1 Chemical ionization at AP

The atmospheric pressure chemical ionization (APCI) may use reagent ions (dopant ions) to drive selective ion chemistry. Primary multiple ion species X are generated in the hot zone of the ion source. Adding the dopant D in access primary dopant ions are generated, cf. equation 2.2. Equation 2.3 shows a simplification of the dopant chemistry in the negative mode. The dopant ion reacts with the analyte A (equation 2.3 or 2.4) and produce an analyte ion. Often a cluster of the analyte and the dopant is generated, which can easily be identified because the mass of the product ion is the sum of the reactant masses (equation 2.4).

These reactions can be driven in the ion source but this expose the analyte to the hot zone of the ion source, which may lead to the fragmentation of the

analyte or other side reactions. So it is beneficial to drive the generation of the dopant seperated ions in the ion source mixing the dopant and the analyte in the following stage.

$$X^- + D \longrightarrow D^- + X \tag{2.2}$$

$$D^- + A \longrightarrow A^- + D \tag{2.3}$$

$$D^- + A \longrightarrow AD^- \tag{2.4}$$

2.3.2 Pumping stages

The number of ions generated in the ion source decreases upon passage through the pressure reduction stages. Without further measures this reduction is proportional to the pressure drop at the nozzles. Ion density is gained when the ions are focused to the nozzles by electrostatic fields. Therefore ion funnels or quadrupoles are frequently used.

In the first assembly (cf. Fig. 3.2) a glass capillary with an inner diameter of 0.5 mm and a length of 18 cm acts as the first gas flow restricting element. The first pumping stage is evacuated by a $16\,m^3\,h^{-1}$ rotary vane pump (Oerlikon Leybold Vacuum, Cologne Germany, Trivac D16B) and optionally by a $505\,m^3\,h^{-1}$ high-capacity roots blower (Oerlikon Leybold Vacuum, Cologne Germany, Ruvac Wsu 501) in combination with a $70\,m^3\,h^{-1}$ rotary vane pump (Pfeiffer Vacuum GmbH, Asslar, Germany, Duo 65 C). A downstream pressure control system consisting of a butterfly valve (MKS Instruments Deutschland GmbH, München, Germany, MKS 253) with a built in valve controller and a capacitance manometer (MKS 626) ensures constant pressures in the range from 1 to 50 hPa in the first pumping stage, independent of the upstream gas flow. The following two pumping stages are equipped with aluminum skimmers with an inner diameter of 0.8 mm each. Both skimmers have a solid angle of 90° at the outer face. The nozzles are positioned at a distance of 24.7 mm. Skimmer 1 is mounted on an insulating disk and can be electrically biased while skimmer 2 is tied to ground potential. The differential pumping stage is equipped with a $1250\,L\,s^{-1}$ turbo pump (Pfeiffer Vacuum, Asslar, Germany, TPU 1201 PC)

achieving a pressure reduction to 10^{-3} hPa in the second pumping stage. The ion transfer element downstream of the second skimmer is equipped with a 250 L s^{-1} turbo pump (Pfeiffer Vacuum GmbH, Asslar, Germany, TMH 261 YP) establishing a sustained background pressure $< 10^{-5}$ hPa. This stage features an ion transfer lens system, which is described in detail in the following section. Downstream of the transfer stage the ions enter the TOF analyzer through an orifice of approx. 3 mm diameter. The TOF is evacuated by a 250 L s^{-1} turbo pump (Pfeiffer Vacuum, Asslar, Germany, TMH 261 YP) and operates at pressures $< 10^{-6}$ hPa.

The second assembly (cf. Fig. 5.2) has an additional transfer element, therefore an oil-free 28 m^3 h^{-1} multi-stage roots pump (Pfeiffer Vacuum, Asslar, Germany, ACP 28) is used to pump an ion funnel operated at 100 hPa. The remaining part of the pumping system is similar for both assemblies. The rotary vane pumps are replaced by two oil free pumps (Pfeiffer Vacuum, Asslar, Germany, ACP 40). The turbo pumps are all pumped by one of the ACP 40 pumps. The second ACP 40 pump is used for the region with an ion funnel driven at 5 hPa. The pressure for both ion funnels is controlled by a butterfly valve system, as described for the first assembly.

2.3.3 Transfer element 3

Tube lens

To guide the ions from skimmer 2 to the direct current (DC) voltage ion optical stage at the entrance of the TOF a Einzel lens was designed employing the simulation software Simion [127]. A schematic of the lens is shown in Fig. 2.3 including simulated ion trajectories. The lens consists of three tube electrodes with an inner diameter of 12 mm, which are mounted to one fixture. Each tube electrode is connected to a voltage source. For ease of installation a movable tube lens extension is mounted on the first electrode to enhance ion collection efficiency.

Additionally the lens system is surrounded by four electrodes, allowing an adjustment of the ion beam in x- and y-direction. The Simion simulations show that this way a skewed installation of less than one degree of the lens system can be corrected without any intensity loss. If the tube lens is properly

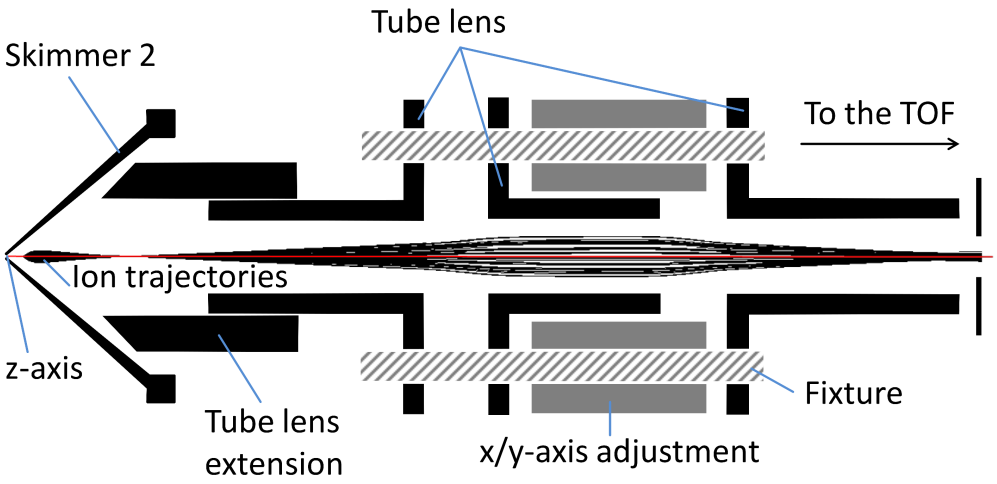

Figure 2.3: A cut through the Simion geometry with ion trajectories in the transfer lens system. The trajectories correspond to the following values; Skimmer 2 and x/y-axis adjustment 0 V; tube lens −70, −20, −70 V; positive ions (m/z 100) starting with a solid angle of 45° and 0.1 eV.

adjusted these four electrodes can be grounded.

Collisions do not play a significant role in this pumping stage (cf. section 3.3.9) and thus are neglected in the simulation. With the local pressure $<10^{-5}$ hPa the probability of collisions is low and transmission reaches 1 with DC optics. Additionally the Einzel lens provides a mass discrimination-free transfer, thus no significant changes of the ion trajectories in the typical mass range (m/z = 20 to 700) are expected. The optimum voltages in the simulation fit well with the optimum in the experiments (Δ 2 V).

RF-only Quadrupole

If operated with a nonselective EI-ion source a RF-only quadrupole with implemented notch filter can optionally be inserted. The quadrupole is operated as transfer device in a RF-only mode at 5.6 MHz with up to 400 V_{pp} and a background pressure of 10^{-5} hPa. It has an inner diameter of 5.2 mm, a rod diameter of 6 mm, and is 110 mm long. The quadrupole can filter out undesired ions (e.g. O_2^+ and N_2^+ ions when operating in air). By residual excitation [133] such ions inducing space charge effects are filtered, which can reduce the amount of ions reaching the detector dramatically [15]. Additionally a huge amount of ions may stress the MCP.

Since the observed transmission of the EI-ion source for ions generated at AP was very unfavorable the source was replaced by an einzel lens. Compared to the tube lens this quadrupole with the einzel lens shows similar transmissions and is used in the second assembly.

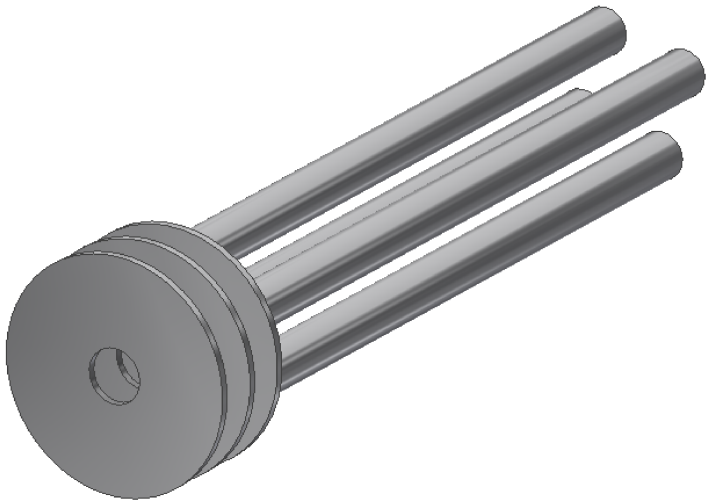

Figure 2.4: A schematic drawing of the quadrupole with the upstream einzel lens.

Chapter 3

Ion bound cluster measurements

3.1 Theory

As detailed in section 3.3 ion cluster chemistry plays an important role in domains 1 to 4 of typical mass spectrometers. A transfer stage for the study of ion clusters is presented and characterized.

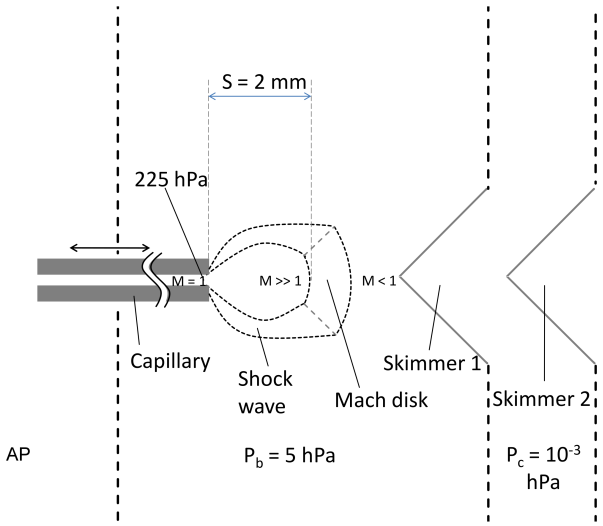

Figure 3.1: A schematic drawing of the capillary outlet and the differential pumping stage. The expansion with the position of the Mach disk is sketched. Additionally the pressures in the pumping stages are shown.

3.1.1 Gas expansions

Figure 3.1 shows a schematic of the first expansion at the capillary exit, the entire setup is shown in figure 3.2. The gas at the end of the capillary travels at the local speed of sound (Mach number, $M = 1$) at a pressure of about 250 hPa. Thus, a free jet forms at the exit of the capillary. Here, the internal energy and random translational energy of the molecules is converted into directed translational motion accompanied by adiabatic cooling of the molecules and a decrease of the speed of sound a, as follows from equation (3.1).

$$a = \sqrt{(\gamma\, R\, T)\,/m} \tag{3.1}$$

R denotes the universal gas constant, T the temperature of the expanded gas, m the molar mass, and γ ($\gamma = C_p/C_v$) the heat capacity ratio [121].

Since ions are efficient drivers of cluster chemistry rather large clusters can be produced in the expansion. The rate of formation is limited by the collision number. The number of bimolecular collisions in the expansion is proportional to $P_0 * d/T_0$, with T_0 as the temperature and P_0 as the pressure of the gas before the expansion, d is the inner diameter of the nozzle. For the clustering processes, termolecular collisions are required. A termolecular collision essentially includes two collisions; the first is the collision of the reaction partners and the second is the excited-state deactivation. In the expansion termolecular collisions are proportional to $P_0^2 * d/T_0^2$ [121]. However, the molecules move essentially collision free after a few nozzle diameters, where they remain in their energy state ("freeze in") [121]. This is caused by the transformation of thermal motion to directed kinetic energy. After the collision free zone a shock front forms where the expanding molecules collide with the background gas if the background pressure is high enough. The terminal Mach number M_t that is reached in the expansion is calculated with equation 3.2. The Knudsen number K_n is defined as the mean free path of the gas before expansion divided by the nozzle diameter [31].

$$M_t = 1.17\, K_n^{((1-\gamma)/\gamma)} \tag{3.2}$$

$$T_t = \frac{T_0}{1 + ((\gamma - 1)\, M_t^2)/2)} \tag{3.3}$$

	First expansion	Second expansion
Experimental parameters		
P_0 [hpa]	250	5
P_1 [hpa]	5	1×10^{-3}
λ_0 [mm]	3.1×10^{-4}	1.4×10^{-2}
d [mm]	0.5	0.8
γ	1.4	
T_0 [K]	295	
Calculated values		
S [mm]	2.3	39
K_n	6.2×10^{-3}	1.8×10^{-2}
M_t	8.3	3.0
T_t [K]	20	105

Table 3.1: The typical parameters of the first two expansions in the mass spectrometer.

The temperature T_t reached in an expansion at a certain Mach number is calculated using equation 3.3 [121]. It depends on the temperature T_0 of the gas before expansion, the terminal Mach number M_t and the heat capacity ratio γ.

The Mach disk is the shock area where the molecules collide with the background gas in the vacuum system (P_b in Fig. 3.1) and decelerate to a speed smaller than the speed of sound. The distance S of the Mach disk to the nozzle is given by the empirical equation 3.4 [121]:

$$S = 0.67\, d \left(\frac{P_0}{P_1}\right)^{1/2} \tag{3.4}$$

S depends on the nozzle diameter d and on the pressure before the expansion P_0 and the pressure after the expansion P_1. The Mach disk has a thickness on the order of the mean free path in the vacuum system. Within the Mach disk region fractions of the directed kinetic energy are converted back into thermal motion of the gas, and the static temperature of the gas increases. The typical parameters for both expansions in the present system are given in Table 3.1.

3.1.2 Thermal cluster distribution

A number of processes potentially change the cluster distribution in the transfer stage of a mass spectrometer, e.g., a "cold" expansion. To evaluate the measured cluster distribution a thermodynamic model for the conditions prevailing after the Mach disk was assembled. The parameters used for the thermodynamic models were calculated from the equilibrium constants determined by Lau et al [76] and Kebarle et al [59].

$$H_3O(H_2O)_n^+ + H_2O + M \longleftrightarrow H_3O(H_2O)_{n+1}^+ + M \tag{3.5}$$

$$\Delta G = \Delta H - T\,\Delta S \tag{3.6}$$

$$K_p = e^{\Delta G/RT} \tag{3.7}$$

$$K_c = K_p\,RT/N_A \tag{3.8}$$

$$log[H_3O(H_2O)_n^+] = \sum_{i=1}^{n} logK_i + (n-1)log[H_2O] + log[H_3O^+] \tag{3.9}$$

Using the enthalpy H and the entropy S, the Gibbs free energy G is calculated form equation 3.6 for a given temperature. The equilibrium constants used for the thermodynamic model are shown in Tab. 3.2. They are calculated from equation 3.7 and 3.8 using a temperature of 295 K. Here, K_p is the equilibrium constant based on the partial pressure of the species involved, K_c is the concentration based equilibrium constant, R is the universal gas constant, and N_A is the Avogadro constant. Equation 3.9 is derived from the equilibrium equations. It represents the cluster concentrations in thermal equilibrium starting with a known H_3O^+ concentration.

3.1.3 Cluster activation

In most API mass spectrometers additional energy is transferred to ions by electrical fields. These electrostatic fields accelerate the ions to kinetic energies exceeding their dissociation threshold, which may induce dissociation upon

n, n+1	ΔH [kcal mol^{-1}]	ΔS [cal K^{-1} mol^{-1}]	K_c (295 K) [cm^{-3}]
0, 1	31.6	24.3	5.08×10^{-2}
1, 2	19.5	21.7	2.04×10^{-10}
2, 3	17.9	28.4	4.56×10^{-13}
3, 4	12.7	23.4	7.93×10^{-16}
4, 5	11.6	25	5.43×10^{-17}
5, 6	10.7	26.1	6.72×10^{-18}
6, 7	11.7	29.6	6.36×10^{-18}
7, 8	10.3	27	2.16×10^{-18}

Table 3.2: The equilibrium constants used for the thermodynamic model of the water clusters estimated with ΔH and ΔS measured by Lau et al [76] and Kebarle et al [59]. The parameter n refers to equation 3.5.

the next collision. For cluster ions the dissociation threshold is comparably low. Elevated collision energy from the electrostatic fields may also drive additional reactions, e.g. the production of protonated species [134]. Collisions driven by electrostatic fields deliver energy to the chemical system causing an elevated effective ion temperature. Moreover, the ion velocity distribution becomes non-Maxwellian due to the directional character of electrostatic fields, hence only an effective temperature can be estimated [18]. The "critical" pressure region is located between two pressure regimes, where not enough collision partners are present (10^{-5} hPa [13]) and pressures, where the mean free path becomes to short for sufficient acceleration. This process is exploited for analytical purposes in the MS/MS experiments as well as for efficient declustering. However, moderate fields are also a viable tool for studying the composition of ion-bound clusters. For simplification the above mentioned processes are often summarized as CID.

The presented MS assembly enables to characterize the processes and chemistry driven by CID. Processes caused by the elevated ion temperature can be studied because electrical fields present in pressure regions sensitive for induced collisions can be tuned as well as completely switched off.

3.2 Experimental

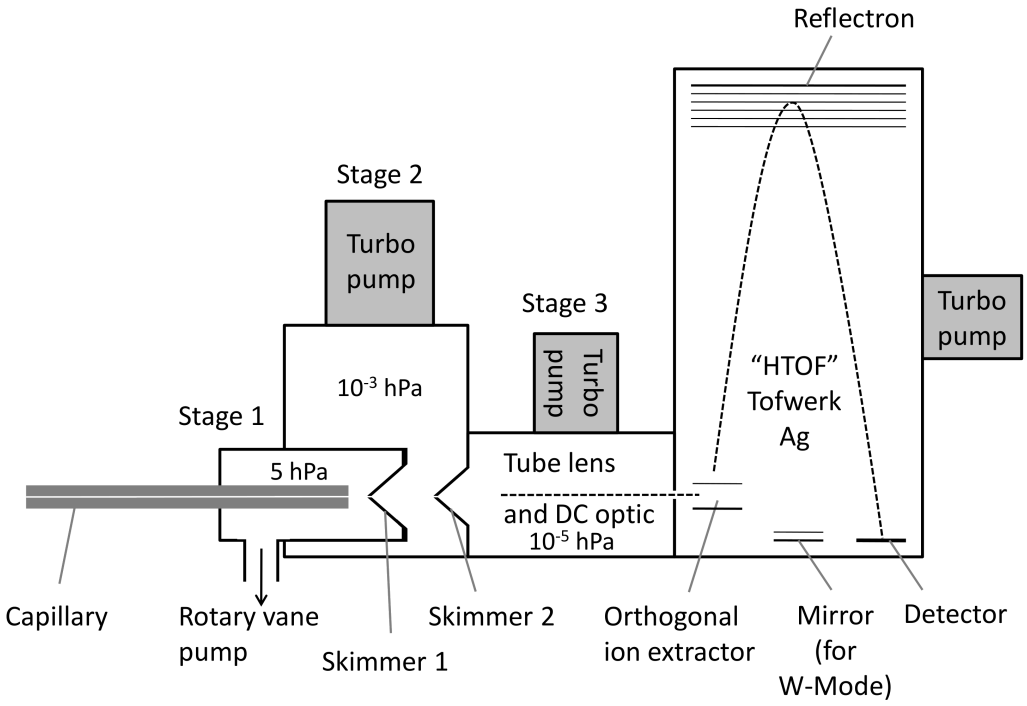

Figure 3.2: Schematic drawing of the mass spectrometer (first generation).

A schematic drawing of the employed mass spectrometer setup is shown in Fig. 3.2. It consists of an atmospheric pressure laser ionization (APLI) ion source, a custom transfer stage and the HTOF. The transfer stage receives the effluent from a capillary sampling from the ion source. It is operated with two skimmers (first generation) or with a skimmer nozzle arrangement (second generation).

3.2.1 Ionization

Proton transfer from the toluene radical cation to water molecules is for example described by Shijian et al. [79] employing deuterated toluene:

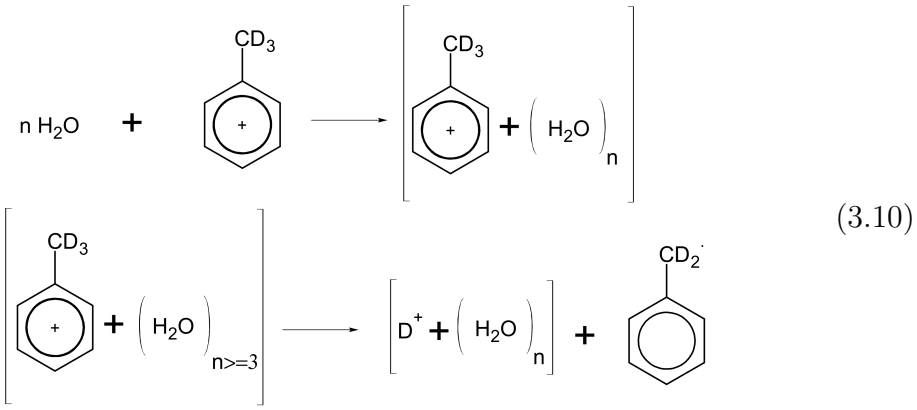

(3.10)

Toluene ions are produced via APLI in a laminar flow ion source [62], [6], consisting of a 10 cm long air-tight flow tube with an inner diameter of 1 cm. It is operated with flow rates of about $1\,\mathrm{L\,min^{-1}}$ leading to a laminar flow inside the ion source. The photon source is a diode pumped solid state (DPSS) laser operating at a wavelength of 266 nm (CryLas GmbH, FQSS 266-50), with a pulse duration of 1 ns, a pulse energy of 50 µJ, and a repetition rate of 100 Hz. The unfocused laser beam had a diameter of 1 mm. It was guided axially through a silica window into the ion source pointing into the glass capillary, which is the main ionization region. Alternatively ionization can be achieved by directing the laser beam perpendicularly into a silica capillary. In this case the signal is one to two orders of magnitude lower, but the cluster distribution remains identical. This indicates that the laser does not dissociate the generated clusters in the axial configuration.

For dopant assisted (DA)-APLI we used toluene, a common dopant in API, which reacts with the ion source matrix finally generating analyte ions. The primary toluene radical cations are generated in a two photon (1+1) resonance enhanced multi photon ionization (REMPI) process [115].

3.2.2 Chemicals

For all measurements described, toluene (Sigma Aldrich, high pressure liquid chromatography (HPLC)-grade, $\geq 99.9\,\%$) was added at the saturation pres-

sure to a flow of nitrogen (Linde, 99.999 %). The resulting gas flow carried a mixing ratio of 200 ppmv toluene. Furthermore, anisole (Sigma Aldrich, HPLC-grade, $\geq$ 99.9 %) and toluene-D8 (Sigma Aldrich, 99 % deuterated) were used as dopants. Purified water (Millipore purification system, Merck KGaA, Darmstadt, Germany), D_2O (Sigma-Aldrich, HPLC-grade, 99.9 % deuterated), methanol (Sigma-Aldrich, HPLC-grade, $\geq$ 99.9 %) or methanol-D1 (Sigma-Aldrich, HPLC-grade, $\geq$ 99.9 %) were added at the saturation pressure to the gas flow at mixing ratios described further below for each experiment.

3.2.3 Transfer element 1

The glass capillary with an inner diameter of 0.5 mm and a length of 18 cm acts as the first flow restricting element. The exit of the capillary in the low pressure region is wrapped with 0.25 mm diameter tantalum wire, which allows to heat the gas flow. At the used experimental conditions the flow within the capillary is a fully developed turbulent choked flow [70]. Gimelshein et al. recently worked with 10 cm long capillary, which had an inner diameter of 0.5 mm. They reached a Reynolds number of 3000 and reported that the flow develops over a distance <1 cm downstream the inlet of the capillary [37].

Both ends of the capillary are metalized to provide a defined potential at the in- and outlet. The inlet was connected to ground potential, while the outlet was either grounded or held at a defined potential resulting in a field gradient from 0 to 1000 $\mathrm{V\,cm^{-1}}$.

The capillary is operated critically, with an exit plane pressure around 250 hPa [63]. The gas leaving the capillary thus forms an adiabatic expansion leading to the formation of a Mach disk. The location of the Mach disk is a function of the background pressure. In the present experiment this location can be easily adjusted from a position upstream of the skimmer orifice to a position downstream the orifice. The former “mode” thus represents thermal equilibrium sampling of the molecules present in the ion source region due to reequilibration in the shock. The latter “mode” leads to rapid further adiabatic cooling to very low rovibrational temperatures and resembles supersonic jet sampling (cf. [121]).

Also within the capillary flow the pressure drops; the exit port pressure is the base pressure of the expansion. The required equations for exit pressure

calculations are discussed in the literature [96], [150]. For a 18 cm long capillary with an inner diameter of 0.5 mm a pressure of 255 hPa at the capillary exit is calculated, with the upstream port held at about 1100 hPa. The capillary exit port was adjusted to a distance of 6 mm upstream of skimmer 1 for thermal sampling.

All experiments were conducted at room temperature, which is also used for the simulation of the cluster distributions.

3.2.4 Skimmer/orifice plate setup (Nozzle setup II)

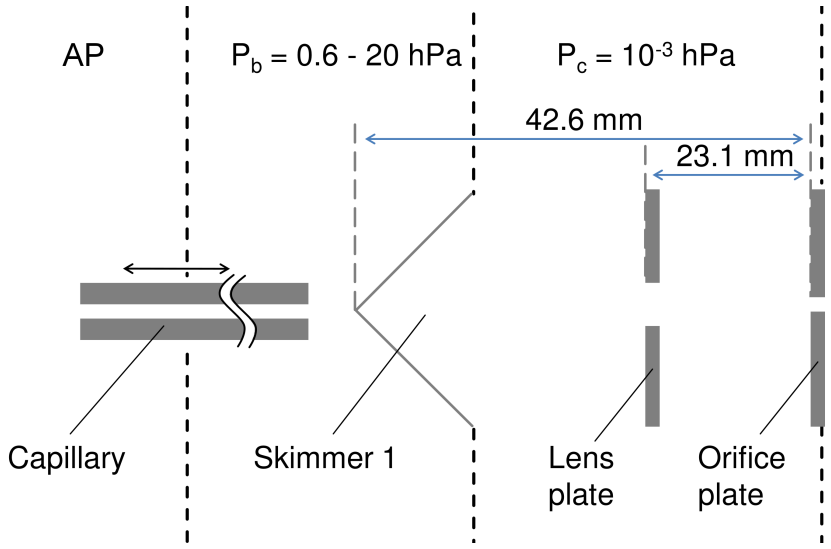

Figure 3.3: A schematic drawing of the skimmer orifice plate assembly.

In a second generation setup the two skimmer assembly (see figure 3.2) is replaced by a skimmer/orifice plate assembly, as shown in figure 3.3. The orifice of skimmer 1 is reduced to 0.6 mm to reduce the terminal temperature in the expansion, thus increasing the pressure and concentration range for the thermal sampling mode. Skimmer 2 is substituted by an orifice plate (inner diameter (ID) 2 mm). The orifice plate is isolated using a ceramic mount and may be biased. An additional plate electrode mounted between the first skimmer and the orifice plate creates a lens assembly. The plate electrode is made of stainless steel with a 1 cm center hole. The lens plate has a distance of 23.1 mm to the orifice plate.

3.3 Results

3.3.1 Position of the Mach disk

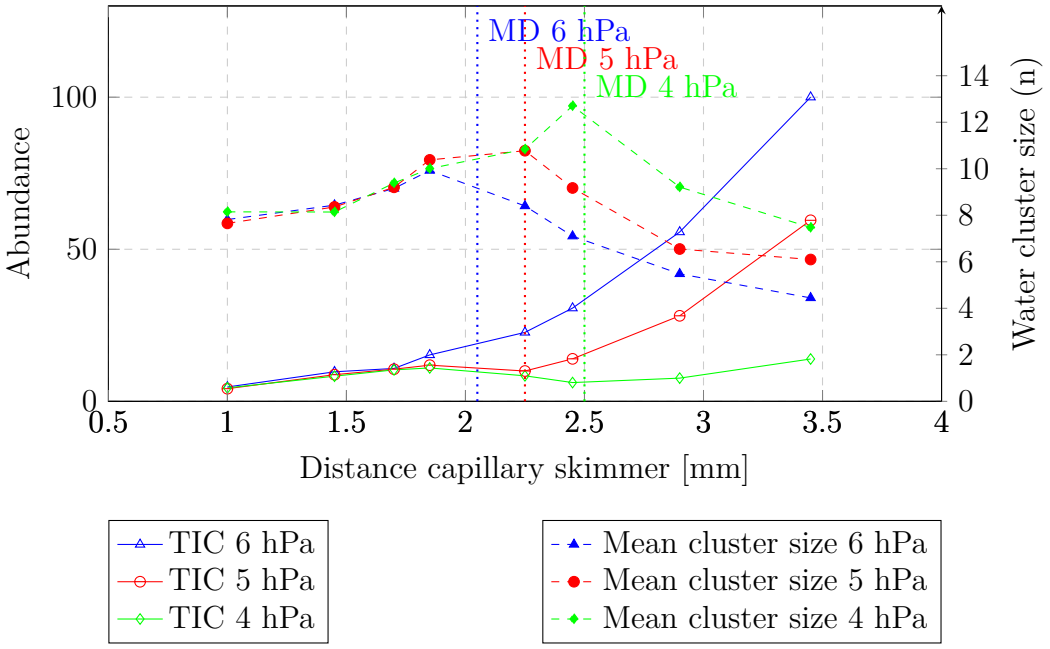

Figure 3.4: The measured relative signal intensities (solid lines) and the signal weighted water cluster size average (dashed lines) at different pressures in the first pumping stage as a function of the distance between the capillary and skimmer 1. The water mixing ratio is 0.16 %vol. The dotted lines mark the calculated positions of the Mach disk.

The position of the Mach disk calculated using equation 3.4 and the parameters in table 3.1, it is 2.3 mm downstream of the capillary exit at 5 hPa, i.e., centered between the capillary and skimmer 1. The measurements show that there is a rapid decrease of the average cluster size starting at a distance between the capillary and the skimmer of 2.3 mm (cf. Fig. 3.4), in perfect agreement with the calculated position (2.3 mm) of the Mach disk. Additionally Fig. 3.4 shows the mean cluster distribution at 6 hPa. The calculated Mach disk position is 2.1 mm at 6 hPa, which also matches reasonably the experimental data. The figure shows that the cluster distribution needs approximately 1 mm travel distance to adjust to the local conditions. For the thermal sampling mode the capillary was thus positioned at a distance of 6 mm upstream of skimmer 1,

keeping skimmer 1 downstream the Mach disk at pressures of ≥5 hPa in this pumping stage.

The reduction of the pressure downstream of the capillary from 10 hPa to 1 hPa changes the position of the Mach disk from before to virtually behind skimmer 1. The position of the Mach disk can thus easily be moved "behind" the skimmer without changing the capillary position. However, the pressure reduction results in a signal loss at least of an order of magnitude. A more efficient way is to move the capillary at constant pressure.

With larger distance an increase in the absolute signal intensity is clearly seen in Fig. 3.4. This measurement has been made using a krypton-vacuum ultraviolet (VUV) lamp to generate toluene radical ions due to the much better ion production stability while moving the capillary. At lower distances the individual cluster signals are lower because many cluster species are generated in the cold expansion. Also the total ion count (TIC) was two orders of magnitude lower compared to the thermal sampling mode. At the position of the Mach disk a sharp increase in the signal intensity is observed most probably associated to a change in the fluid dynamics. After the Mach disk the signal increases further until the optimum position is reached. The water cluster distribution has reached its thermal equilibrium 6 mm downstream of the capillary at ≥5 hPa, as shown in Fig. 3.6. Figure 3.5 illustrates the rapid change in the water cluster distribution after the Mach disk.

3.3.2 Thermal sampling

Many cluster processes have been studied using effusive nozzles [121]. The disadvantage of this measurement technique is the small orifice required limiting the ion flow into the mass analyzer. An alternative approach for measuring the cluster distribution is what is called here the "thermal sampling mode". Searcy et al. [122] reported that they found relatively small clusters using a non-effusive sampling nozzle, although clusters should grow in the cold expansion region. Later Zook et al. [153] found that they can measure the thermal equilibrium cluster distribution without an effusive nozzle when working at a specific elevated temperature range with He as buffer gas.

In the present experiments clusters produced in the ion source are sampled via a capillary. In the expansion downstream the capillary the water clusters

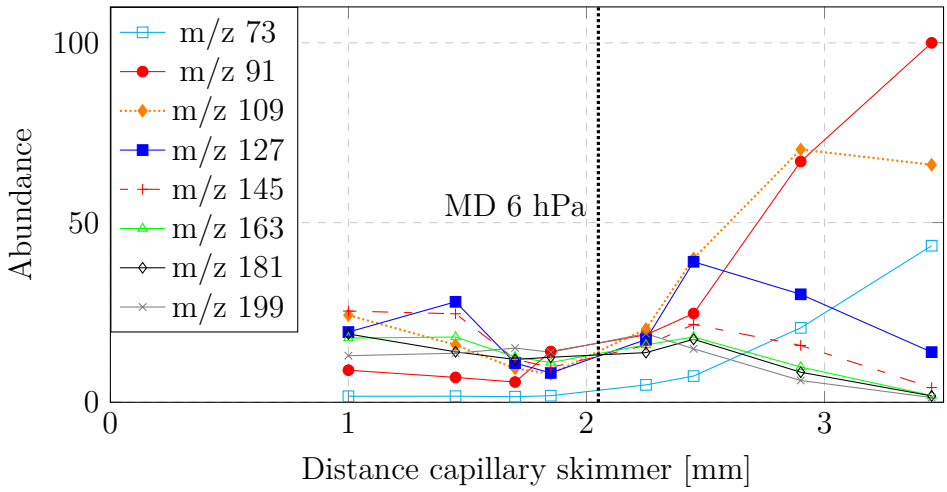

Figure 3.5: The measured relative signal intensities at 6 hPa in the first pumping stage as a function of the distance between the capillary and skimmer 1. The water mixing ratio is 0.16 %vol. The black dotted line marks the calculated position of the Mach disk.

nucleate with neutrals and lose these neutrals again within the Mach disk due to ample collisions. If no nucleation process is initiated in the second expansion, sampling of the thermally reequilibrated cluster distribution produced after the first Mach disk is thus possible. For this reequilibrated cluster distribution the same gas temperature as in the capillary is assumed, as supported by the distribution measurements (cf. section 3.3.2 and Klopotowski et al. [71]). On average the clusters are smaller than those present in the ion source because of the pressure reduction from the ion source to the Mach disk.

The current assembly is limited to 60 mm maximum distance between the capillary and skimmer 1. The expansion behind the capillary is resembling a directed gas stream [71], so even at larger distances no significant signal losses are expected.

In figure 3.6 the transition from the thermal sampling mode (5 hPa) to an expansion cooled cluster distribution (15 hPa) is shown. For these measurements the background pressure at the exit port of the capillary was changed (5 hPa, 10 hPa and 15 hPa, respectively). The input mixing ratios and the total flow were held constant. The comparison with the thermodynamic model shows that the cluster distribution fits very well at 5 hPa for a water mixing ratio of 0.3 %vol. At 10 hPa changes in the cluster distribution caused by additional nucleation

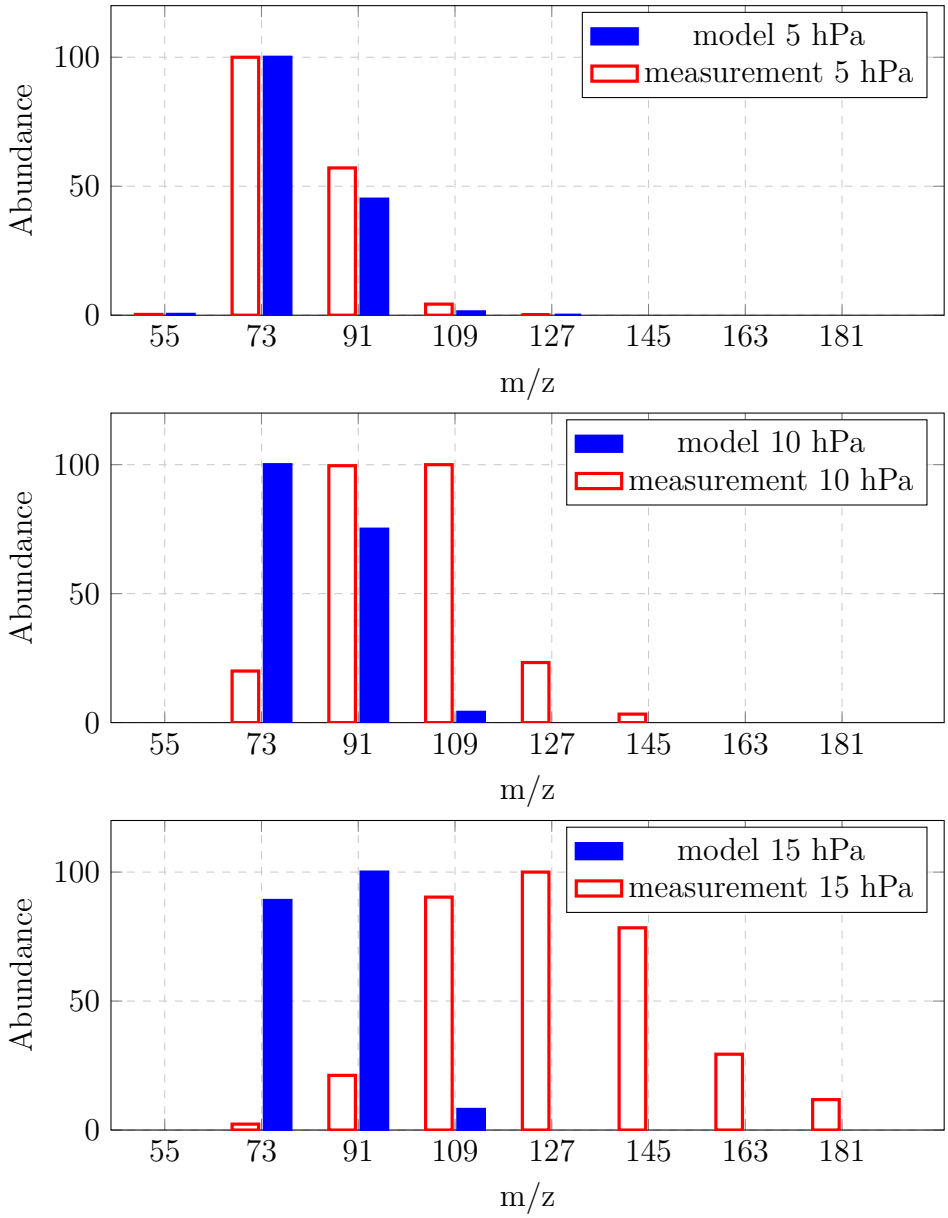

Figure 3.6: Normalized intensity of the measured water cluster signals at 5 hPa, 10 hPa, and 15 hPa in the first pumping stage (red bars). The solid blue bars give the water cluster distribution calculated by the thermodynamic equilibrium model (see section 3.1.2). The water mixing ratio is 0.3 %vol. Each spectrum has been scaled to the most abundant peak (100 %).

in the cold expansion are observed. The spectrum at 15 hPa exhibits an even broader non-thermal cluster distribution not caused by the first expansion. In the next section is shown that this is due to nucleation processes taking place in the second expansion.

In negative ion mode $[O_2(H_2O)_n]^-$ clusters are generated by thermal electrons from the toluene ionization process and subsequent attachment to O_2. The distribution of these clusters has been compared to literature data [105], which confirms the thermal equilibrium distribution of the clusters [24].

3.3.3 Nucleation processes

Nucleation becomes possible whenever the partial pressure of a compound exceeds the vapor pressure of the condensed phase for the given temperature [18]. This happens in the "cold" expansion particularly for the polar species. Additionally ions act as nucleation sites. Therefore larger clusters are produced in the first expansion. However, these clusters reequilibrate to the thermal conditions after the Mach disk. Thus, in the thermal sampling mode nucleation processes in the second expansion are avoided.

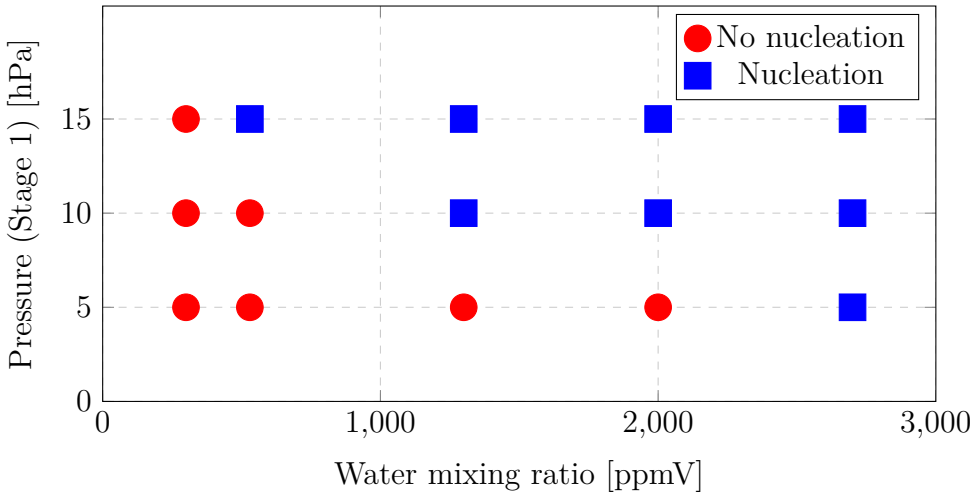

Figure 3.7: Background pressure in the first pumping stage plotted against the water mixing ratio in the ion source. The plot shows where a nucleation process in the second expansion changed the measured cluster distribution.

Measurements have been made with a water vapor mixing ratio of 1300 ppmv (at 5 hPa in the first pumping stage) derived from the mixing ratio in the ion

source. The measurement shows that this is right below the threshold of nucleation. Doubling the pressure results in nucleation in the second expansion, as plotted in Fig. 3.7. Both measurements have been made at low terminal temperatures in the second expansion as estimated by the empirical equation 3.3. Using the empirical vapor pressure equation for the water vapor pressure above ice, as determined by Marti and Mauersberger [87], the critical water concentration for the nucleation is estimated. Comparing the critical water concentration with the present water concentration shows that nucleation should occur in both measurements in the second expansion. We assume that under certain conditions (cf Fig. 3.7) the time in the second expansion is too short for efficient nucleation because the collision frequency in the second expansion rapidly drops to very low values, because the mean free path at 10^{-3} hPa becomes higher than the distance between the nozzles. Higher pressures in front of skimmer 1 (10 hPa) reduce the nucleation time in the second expansion and result in larger water clusters. This behavior has been modeled [143], however, a detailed study should be subject of forthcoming research.

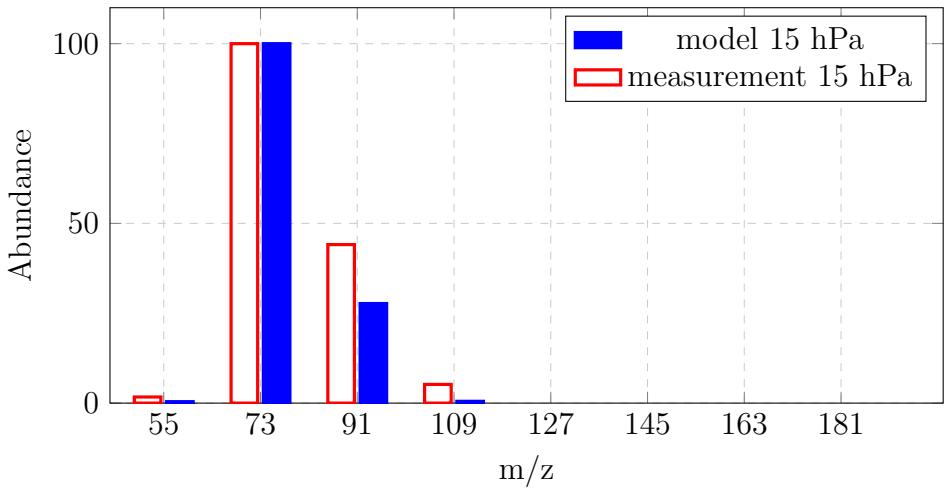

Figure 3.8: Abundance of the measured water clusters (15 hPa in stage 1, water mixing ratio is 300 ppmv) compared with the simulated water cluster distribution by the thermodynamic model.

At higher pressures the nucleation process in the second expansion gets faster but using smaller water mixing ratios the nucleation process gets slower again measuring thermal cluster distributions. Figure 3.8 shows such a measurement at 15 hPa in the first pumping stage and a water vapor mixing ratio of 300 ppmv

resulting in a nearly thermally equilibrated cluster distribution. Details of the nucleation processes in the expansion are given by Gordon et al. [38]. Here just a rough estimate is made to demonstrate that this model fits well with the measurements. The temperature and pressure in the expansion drops resulting in a slower water cluster production. The forward reaction rate for the water cluster production is $10^{-29}\,\mathrm{cm^6 s^{-1} molecules^{-2}}$ at 300 K [44]. Because water is in excess over the cluster ions it is straight forward to calculate the reaction time for the water clusters. Using a water mixing ratio of 1300 ppmv the reaction time is 4×10^{-4} s for 15 hPa and 3×10^{-3} s for 5 hPa. The time the gas spends between the two skimmers is approximately 1×10^{-4} s. This explains the change from a thermal cluster distribution to nucleation when increasing the pressure from 5 hPa to 15 hPa.

3.3.4 Labeling experiments

3.3.4.1 H/D Exchange

Most proton/deuteron (H/D) exchange reactions are collisionally controlled [12]. Because in the present experiments the exchange occurs within a cluster, binary collisions with the background gas with an energy of a few hundredths of electron volts are sufficient to drive such processes. H/D exchange was observed in the measurements shown in figures 3.9 to 3.12. H/D exchange may adversely affect analytical determinations if deuterated labels are employed. In order to research this process methanol-D1 instead of water was added to the toluene ions at a ratio of 1.2 %vol. The resulting cluster distribution has been measured in the expansion and after the Mach disk. The Mach disk was moved by a pressure change in the first differential pumping stage, resulting in a position located behind the skimmer (0.6 hPa) and in front of the skimmer (6 hPa), respectively.

In figure 3.9 protonated methanol-D1 clusters have been sampled within the expansion, before the Mach disk. In all experiments the methanol and methanol-D1 concentration is 1.2 %vol. Upon sampling downstream of the Mach disk, only deuterated methanol clusters were found, as shown in figure 3.10. The proton transfered from the toluene to the methanol-D1 clusters is lost in the Mach disk and replaced by a deuteron. H/D exchange is also possible

by using toluene-D8 and methanol. As shown in figure 3.11, methanol clusters are deuterated by toluene-D8. Within the Mach disk the clusters collide with the neutral background molecules and exchange the deuteron with a proton. The intensities when sampling within the expansion are lower resulting from a lower pressure and the additional ion peaks produced by the supersonic jet. Overall this result demonstrates proton deuteron exchange is feasible within the Mach disk.

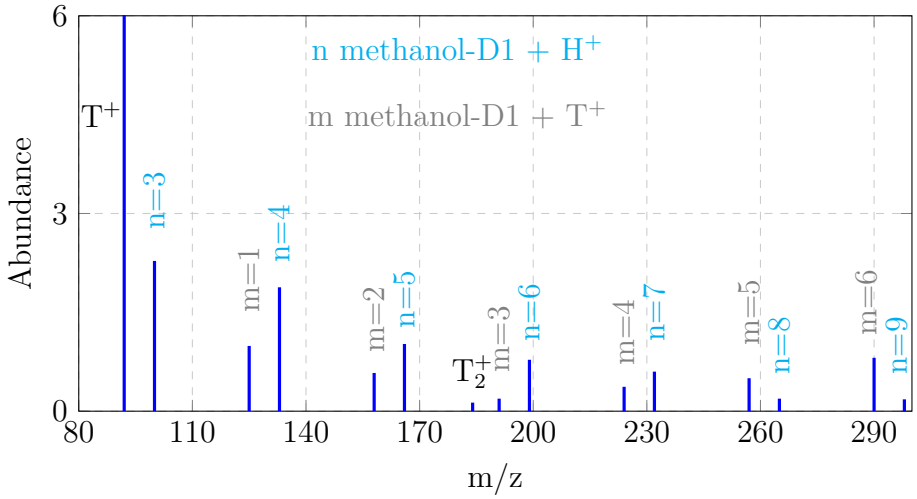

Figure 3.9: Intensity of the measured methanol-D1 clusters and toluene (mass 92) at 0.6 hPa (sampling in the expansion).

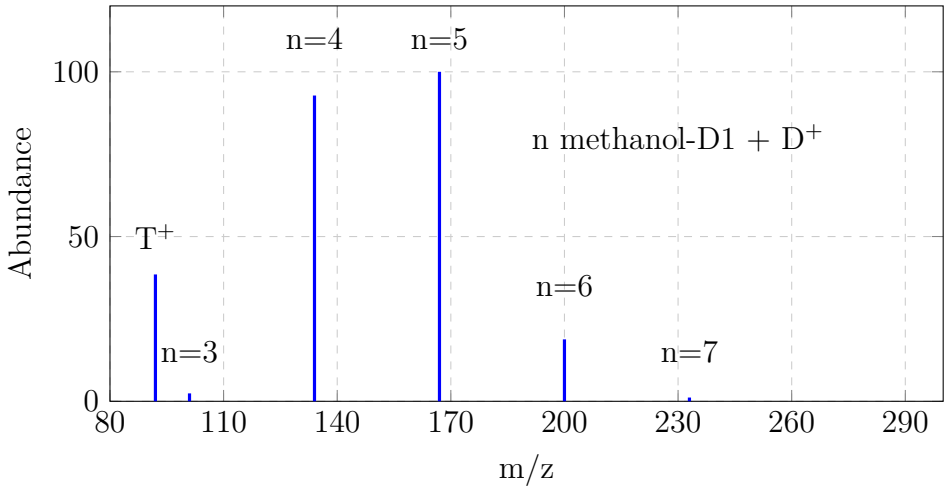

Figure 3.10: Intensity of the measured methanol-D1 clusters and toluene (mass 92) at 6 hPa (sampling downstream of the Mach disk).

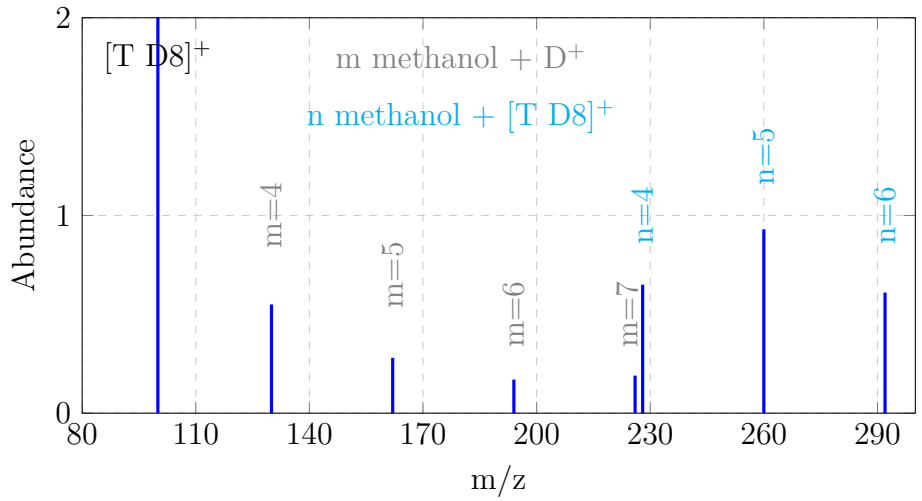

Figure 3.11: Intensity of the measured methanol clusters and toluene-D8 (mass 100) at 0.6 hPa (sampling in the expansion).

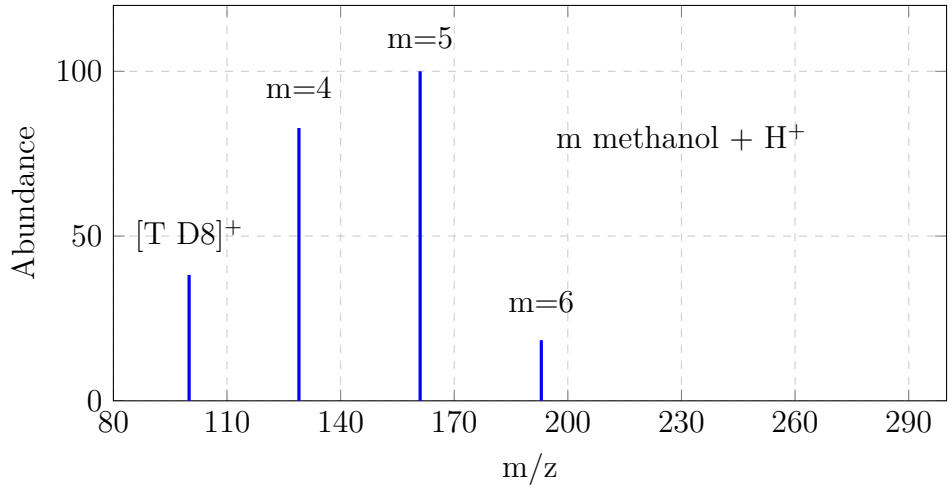

Figure 3.12: Intensity of the measured methanol clusters and toluene-D8 (mass 100) at 6 hPa (sampling downstream of the Mach disk).

Similar observations have been made with the reaction between toluene and D_2O. The energy is provided from the collisions with the background gas in the Mach disk after the capillary. These clusters have undergone many more collisions in the ion source, so why has the H/D exchange not happened already in the ion source? Probably at lower collision energies of 0.01 eV only the outer shell of the water clusters change while the inner shell protects the ion. More energy is needed to remove parts of the inner shell. In the expansion downstream the capillary higher velocities are reached compared to the thermal motion of the gas. This energy is obviously high enough to initiate the H/D exchange.

3.3.4.2 Toluene water reaction

The ionization of water by toluene is no direct charge transfer reaction because the ionization energy of water is higher than the ionization energy of toluene or the toluene dimer. Also the direct proton transfer is thermodynamically not favored. [68] But the free energy of the ion water system is lowered by the cluster formation [59]. So the dipolar water molecules stick to the polar ion and form a cluster with higher proton affinity than the toluene ion.

Miyazaki et al. studied the benzene water ion cluster system by infrared (IR) measurements. They observed drastic changes in the spectra of the benzene water cluster with four water molecules compared to the benzene water cluster with three water molecules. These changes have been referred to a proton transfer reaction as shown in equation 3.11 because the proton affinity of the benzene radical is in between the values for water clusters with n = 3 and n = 4 [98]. The proton affinity of the toluene radical is nearly identical to benzene [103]. So a similar proton transfer is expected.

$$T^{\cdot+}(H_2O)_n \longrightarrow [T-H]^{\cdot} + H_3O^+(H_2O)_{n-1} \tag{3.11}$$

Bernstein et al. studied the toluene water cluster system but they did not observe that the generation of water clusters is thermodynamically favored if up to three water molecules are attached to the toluene radical cation. They concluded that the fragmentation of aromatic cluster systems is favored because stable products are formed (e.g. a toluene radical and a water cluster).

Additionally they observed that the formation of water clusters is much faster for clusters with n > 3 [79].

Toluene water clusters containing many water molecules are produced in the expansion after the capillary as shown in Fig. 3.13. These clusters are not observed in the thermal sampling mode, which gives evidence of their fragile nature. We conclude that the toluene water clusters do not survive collisions taking place in the Mach disk and only their fragments or reaction products are observed.

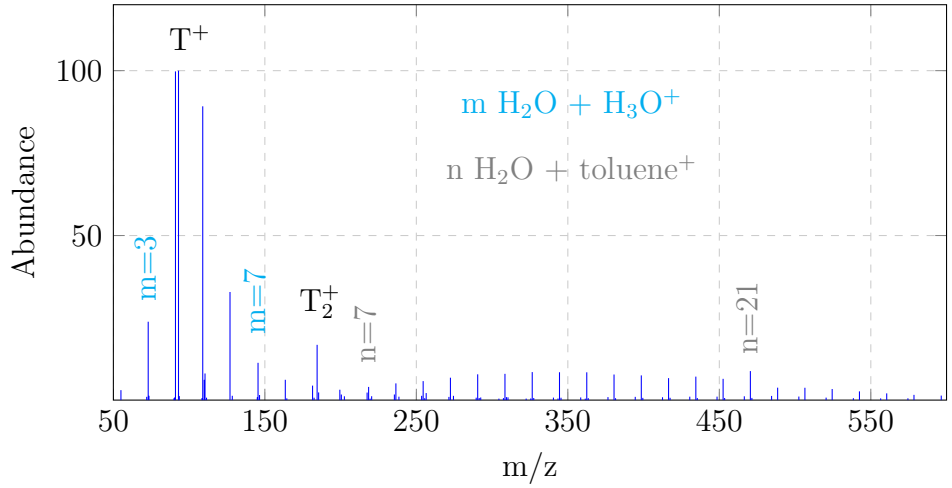

Figure 3.13: Intensity of water clusters and toluene water clusters at 5 hPa. The distance between the capillary and skimmer 1 is 1 mm in the expansion and the water concentration is 0.1 %vol.

Additionally H/D exchange within the water clusters is observed in the Mach disk. The loss of a single deuteron in large water clusters upon collisions may confuse the study of proton transfer reactions.

3.3.5 Heating by electrical fields

The transfer stage of the present setup has been optimized to minimize CID processes in the "thermal sampling mode". This is shown experimentally in Fig. 3.6. In addition, controlled CID experiments in the pressure regimes 10 hPa and approximately 10^{-3} hPa are performed. In the first regime a vibrational excitation by multiple collisions is still likely to occur, leading to the dissociation of the cluster. In the second regime it is not likely that multiple collisions occur.

Here the dissociation energy is provided mainly by single collisions [58].

More collision energy is provided if ions are accelerated by e.g. electrostatic fields. In the AP ion source commonly no high fields are applied and the mean free path is too short for the ions to gain much energy. However, electrostatic fields in the intermediate- and low-pressure regions may drive ion chemistry different from the ion source chemistry. Modern API instruments always involve energetic collisions induced by electrical fields to cool ions by collisions with the background gas [60]. Figure 3.14 shows that these fields drive water cluster dissociation down to n = 1..2, which are in a low mass range not usually measurable due to mass discrimination.

While applying voltages to the electrodes in the respective pumping stages changes in the cluster size distribution induced by CID were monitored. All experiments shown here were performed with a water mixing ratio of 0.12 %vol. The pumping stage downstream of the capillary was held at a pressure of 10 hPa, resulting in a background pressure of 10^{-2} to 10^{-3} hPa in the following pumping stage. CID at 10 hPa was driven with a potential at the capillary tip with grounded skimmers. The applied field gradient between the capillary and skimmer 1 was varied from 0 to 1000 V cm^{-1}. Due to the short mean free path comparably high voltage gradients are required to induce CID processes here. At field gradients of 330 to 475 V cm^{-1} the maximum of the water cluster distribution was reduced from n = 4 to n = 3. A field gradient of 1000 V cm^{-1} resulted in a water cluster distribution with a maximum intensity at n = 2.

CID at 10^{-3} hPa was driven with skimmer 2 grounded and connecting the capillary tip and skimmer 1 to the same potential. The gas density is much lower, thus much lower voltages are required to drive CID processes in this pressure region. Without electrical fields present the ions spend less than 100 µs between the skimmers with a mean free path larger than the distance between the orifices. At this pressure, favorable CID field gradients are below 10 V cm^{-1}. The reduction of the cluster size with the potential between the skimmers is shown in Fig. 3.14. Below 1.25 V cm^{-1} no appreciable CID effects have been recorded. At field gradients exceeding 8 V cm^{-1} first $[M-H]^+$ toluene fragments as well as production of nitrogen ions has been observed. At field gradients of 17 V cm^{-1} these peaks show intensities comparable to the toluene $[M]^+$ peak. It is reasonable to assume that higher field gradients are reached at

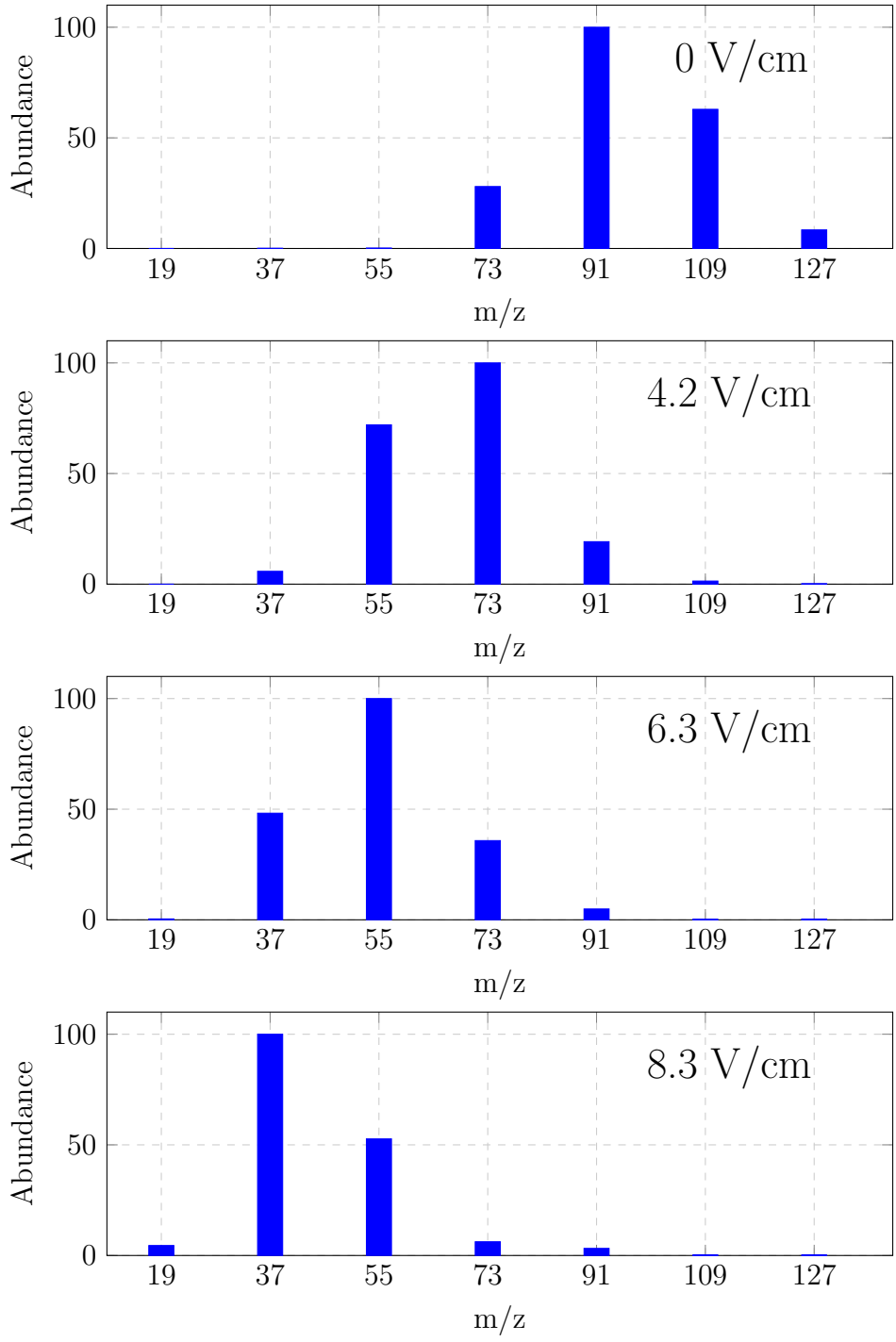

Figure 3.14: Relative intensities of the measured water clusters as function of different CID voltages between the two skimmers. ($p = 10^{-2}$ to 10^{-3} hPa)

the sharp skimmer tip. Additional the gas has an increased conductivity caused by the ions transported. So a plasma burns at the tip of the skimmer creating nitrogen ions using field gradients exceeding $8\,\mathrm{V\,cm^{-1}}$. The mean energy of the electrostatic field must be much lower, otherwise water clusters should not be present at all. The binding energy of H_3O^+ is 1.1 eV and decreases for larger water clusters (0.3 eV for $[H + (H_2O)_4]^+$, m/z = 73), cf. table 5.3.

Without electrical fields present it is possible to record radical cation multimers such as T_2^+ as well as ion bound clusters. These multimers and clusters are obviously present in the ion source. An example is the toluene radical cation dimer which is easily dissociated at electrical fields of the order of $16\,\mathrm{V\,cm^{-1}}$, as shown in Fig. 3.15. For the measurements of the toluene spectra the distance between the capillary and skimmer 1 has been increased to the maximum (60 mm) resulting in maximum equilibration time. Measurements with a distance of (10 mm) between the capillary and skimmer 1 at similar conditions shows no significant differences. Moving the capillary illustrates the magnitude of the reaction rates involved. The observed convergence with increasing distance between capillary and skimmer shows that an equilibrium is reached. Unfortunately rate constants or nucleation rates for the toluene multimers are not available to address nucleation in the second expansion. Ernstberger et al. [30] measured a dissociation energy of 0.660 eV for the toluene radical cation dimer indicating that the dimer is stable under the conditions in the ion source. Because no larger toluene clusters were measured is concluded that the toluene monomer/dimer ion system is fully equilibrated at maximum skimmer distance.

3.3.6 Heated capillary

In order to study the dependence of the cluster size distribution on the gas temperature, mass spectra were taken with the capillary held at room and elevated temperature, respectively. These experiments were performed at 0.3 %vol water vapor mixing ratio and at a pressure of 10 hPa. A thermocouple was placed on the outer wall of the capillary about 5 cm upstream of the exit, resulting in an overestimation of the effective gas temperature due to the colder tip of the capillary and the cooling effect of the expansion. Figure 3.16 shows the cluster size distributions measured for temperature readings of 295 K and

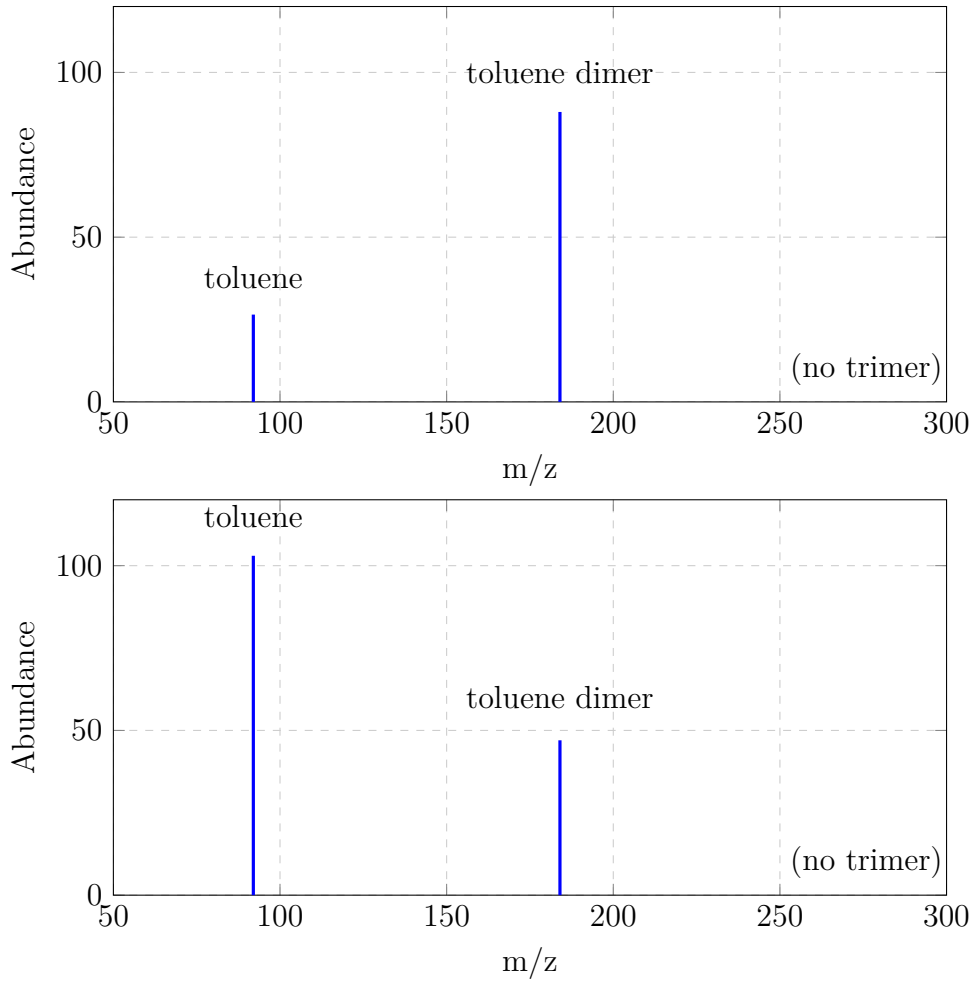

Figure 3.15: Mass spectrum of toluene at thermal sampling conditions without electrostatic fields (top) and at 16 V cm^{-1} (bottom). The pressure in pumping stage 1 was 15 hPa and the mixing ratio of toluene was 480 ppmv.

490 K, respectively. These are compared to simulated cluster size distributions employing the thermodynamic model (cf. 3.16). For the capillary at room temperature the experimental distribution is best matched by a cluster size distribution modeled for 250 K gas temperature while for the heated case the distribution is best matched for a temperature of 372 K, which is in reasonable agreement with the crude temperature measurements.

The total ion count decreased by 40 % upon heating the capillary compared to RT while the total mass flow into the capillary has been kept constant. However, this causes the pressure in the ion source to increase from 828 torr (250 K) to 975 torr (372 K). This effect is due to the temperature dependence of the the gas viscosity.

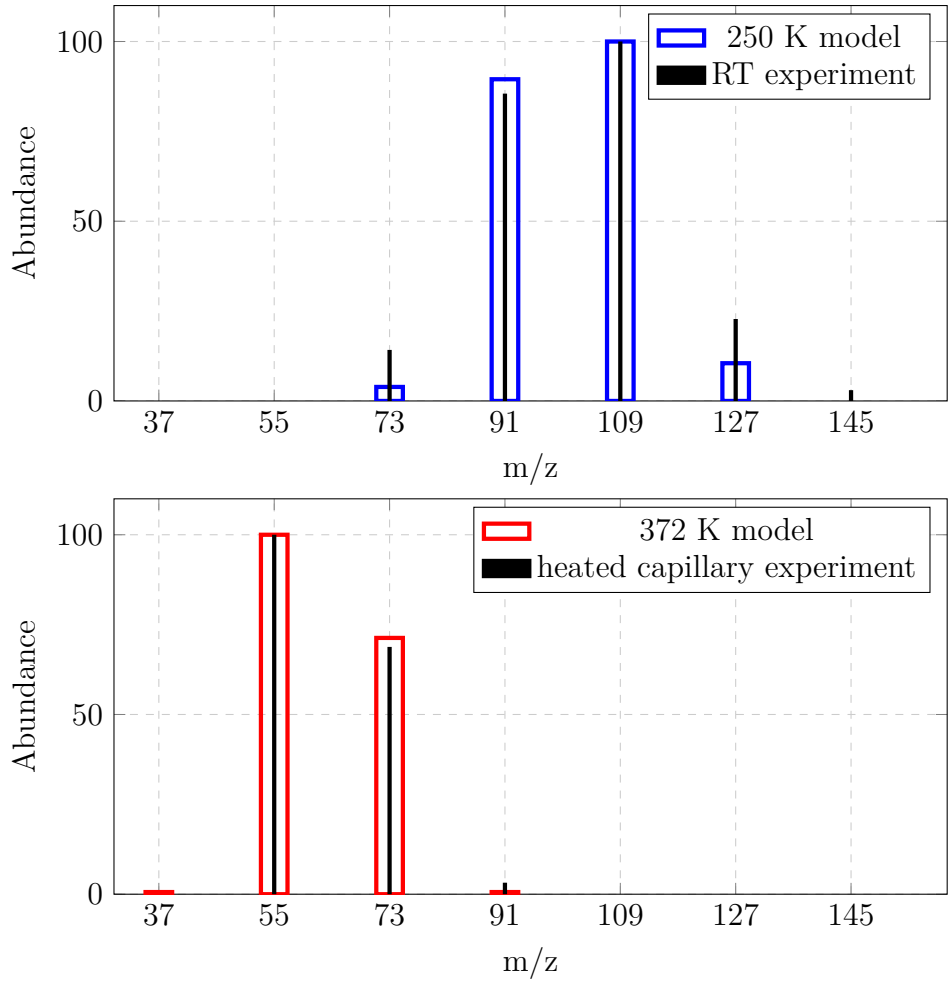

Figure 3.16: Measured and simulated cluster distributions at room temperature and elevated temperature. The water mixing ratio is 0.3 %vol.

3.3.7 Protonation via CID

Collisional activation also provides energy for other reactions, e.g. protonation or deprotonation. This is shown by measurements with different suitable molecules. Toluene radical cations primarily form the radical ion dimer as shown in Fig. 3.15 (top). Such ion bound dimers and clusters are easily destroyed using electrostatic fields.

In an experiment approximately 1 ppmv N,N-diisopropylethylamine is mixed with 1500 ppmv water. As in the previous experiments the primary ion generated is toluene. N,N-diisopropylethylamine (m/z 129) is ionized by charge transfer in the thermal equilibrium mode. Even the amine with its strong gas phase basicity is not efficiently protonated but it acts as protonated water cluster ligand, cf. equation 3.12.

$$[H_3O(H_2O)_n]^+ + Amine \longleftrightarrow [H_3O(H_2O)_{n-1}Amine]^+ + H_2O \tag{3.12}$$

$$[H_3O(H_2O)_nAmine]^+ \xrightarrow{\text{CID}} [Amine + H]^+ + (n+1)H_2O \tag{3.13}$$

Adding an electrical field ($8\,\mathrm{V\,cm^{-1}}$) results in a strong signal at m/z 130 as shown in Fig. 3.18. This demonstrates that the protonation of the amine, is facilitated by the electrical field, cf. equation 3.13. Water ion clusters have a lower gas phase acidity than the bare hydronium ion because the proton is stabilized by additional water molecules in the clusters [8]. Thus we conclude that molecule polarity inducing cluster formation plays an important role for the ion source chemistry and it is a reason why the simple concept of gas phase acidity does not lead to reasonable results.

These reactions play a role in all ion sources which are open to the atmosphere, i.e. water is present in mixing ratios exceeding 100 ppmv. Even in the lower stratosphere the mean annual water vapor is around 4 ppmv [69]. The cold tropopause is in the same range. In the troposphere the water vapor concentration increases with decreasing height to the single-digit percentage range at ground level. This is the water vapor range encountered for flight campaigns planned in the future. In closed AP ion sources generally a few

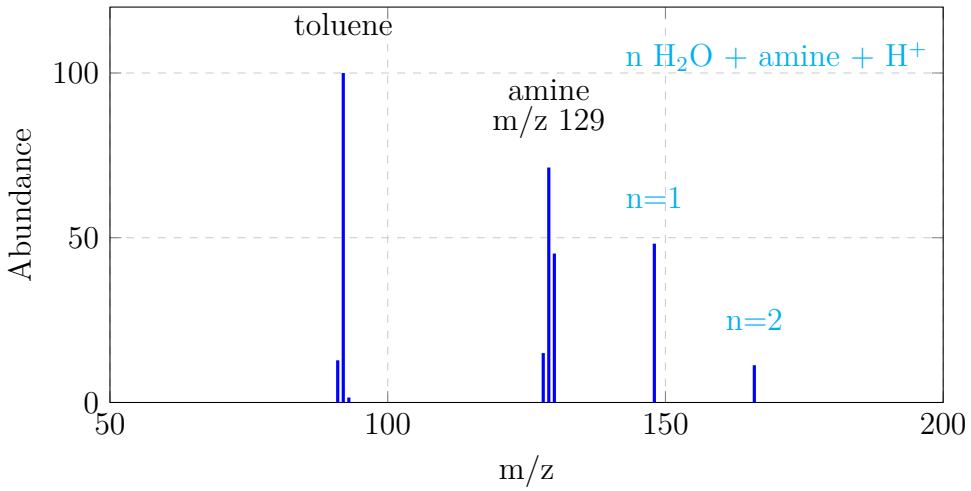

Figure 3.17: Mass spectrum of N,N-diisopropylethylamine measured with the first version of the cluster transfer stage. The pressure after the capillary was 10 hPa and 0 V were applied between the skimmers.

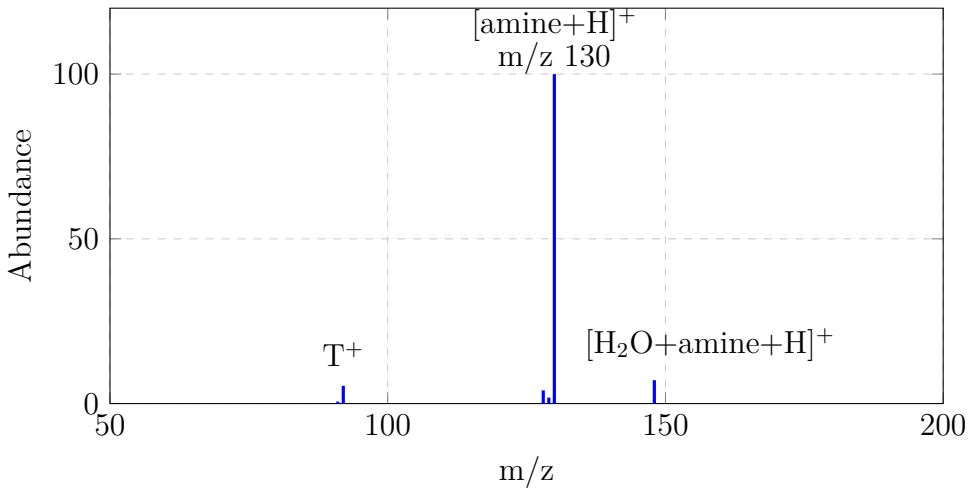

Figure 3.18: Same as Fig. 3.17 but with 20 V applied between the skimmers (10 V cm^{-1}).

ppmv water are present due to water residuals in buffer gases, analytes and dopants.

There are some critical requirements that assist the efficient protonation of analytes by CIMS or other dopant assisted ionization methods. An interaction of the analyte with the proton bound cluster system is governed by the chemical properties of the analyte, e.g. polarity. The analyte has to compete with all other matrix compounds to become a ligand of the proton bound cluster system. If the cluster is destroyed by an electrical field the analyte has to capture the proton. The proton affinity is the main factor for the assignment of the proton to one ligand upon cluster disintegration.

3.3.8 Signal intensity considerations

The ion concentration generated in the source is reduced over the pressure reduction stages. The reduction is proportional to the pressure drop at the nozzles. Signal intensity can be won if the ions are focused to the nozzle by an electrical field. 850 sccm gas are sampled by the capillary from the ion source held at 1013 hPa. At a pressure of 10 hPa 100 sccm gas are sampled by the first skimmer. The ion concentration is thus reduced by a factor of 9 but only a factor of 2 in signal intensity is gained with an additional voltage on the capillary. The reduction in pumping stage 2 is a factor of 10000 because only 0.01 sccm are sampled by skimmer 2. The signal increase with a potential between the skimmers was a factor of 5 to 10. This agrees with the observations made by Bruins et al. [13], who also worked with a two skimmers sampling system. These observations suggest, that an optimization of their transfer stage may lead to significant signal enhancements. Such improvements will be discussed in chapter 3.3.9.

3.3.9 Nozzle setup II

The measurements described in this section were carried out with two different transfer stage setups: 1) the first generation with a skimmer/skimmer arrangement and 2) the second generation with a skimmer/orifice plate arrangement. Using skimmers leads to sharp electrostatic field gradients as discussed in section 3.3.5. Such field gradients cause a plasma at only 15 V potential difference

between the two skimmers of the 1st generation assembly. In measurements with the new assembly potential differences up to 30 V over a similar distance caused no ionization of N_2.

Compared to the second generation set-up with no electrostatic fields present the two skimmer assembly shows a factor 2 to 4 better transmission. However, less than a factor of 5 is gained with electrostatic fields applied to the skimmers for the thermal sampling mode before considerable CID processes are invoked. The skimmer orifice nozzle assembly demonstrated a strongly improved ion focusing. Without changes in the cluster distribution, i.e., in the "thermal sampling mode" a factor of approximately 20 was gained by applying a small potential between the skimmer and the nozzle. This factor increased to approximately 50 (as compared to grounded electrodes) with further increased voltages, however at the expense of CID, as indicated by the change in the cluster distribution. These results show that combined electrostatic and fluid dynamic simulations of this region aid further improvements of the ion transmission efficiency. Poor signal intensities using skimmer skimmer assemblies have also been observed earlier, see e.g. Bruins et al. [13].

To ensure that no CID occurs in the region downstream of the orifice plate measurements with different diameters of the plate under otherwise identical conditions were performed. The results showed no changes in the cluster distribution with nozzle diameters of 2 mm, 1 mm and 0.5 mm. Also with up to −30 V applied to the nozzle with the electrodes upstream grounded the ion signal increased linearly with the nozzle diameter. This clearly demonstrates that the ion focusing spot of the arrangement exceeds the largest nozzle diameter used (2 mm).

Chapter 4

CIMS inlet and ion source

4.1 Theory

Selected fundamental reaction equations of chemical ionization were already discussed in chapter 2.3.1. A dopant present in large excess hinders the direct ionization of most substances since it competes against these substances for the primary charge. For negative ion CIMS the resulting selectivity towards analyte ionization can be judged by the electron affinity and proton affinity of the dopant, as discussed in the following sections. To generate primary ions numerous ion sources can be used but they may differ in their brilliance. The highest charge densities are reached within plasmas. Even though the entire charge can not be extracted from the plasma, plasma ion sources can be relative brilliant. Another alternative are radioactive ion sources, which have the disadvantage that radioactive material is a severe safety issue.

Chemical ionization cascades can be driven in positive and negative mode. Here, the focus is on the negative ion chemistry because very selective dopants for atmospheric trace gas detection are available. These dopants provide access of multiple analytes present in the stratosphere, as listed in section 4.1.2. The analyte of interest for this work is primarily sulfuric acid. The developed instrumentation can easily be adapted to different dopants, in order to ionize and measure other analytes. The most promising dopants for ionization of stratospheric species are discussed as well.

Section 4.1.3 discusses previously published ion source setups and introduces a new concept developed in this work. In order to achieve accurate mea-

surements of reactive or "sticky" trace species they must be sampled without significant losses, including wall reactions. In the interest of achieving optimum sensitivity the ionization should be driven by an ion chemistry within a brilliant ion source generating selected primary ions and thus initiating a defined ion chemical system. In this chapter a concept for a corresponding inlet stage including a selective reagent ion source is presented.

4.1.1 H_2SO_4 ion chemistry

In the atmosphere H_2SO_4 is mainly produced by the oxidation of SO_2, as sketched in equations 4.1, 4.2 and 4.3. The rate limiting step for these reactions is reaction 4.1. The direct reaction of water and SO_3 (reaction 4.3) has a relatively high activation barrier. Most likely the reaction proceeds via water cluster formation [85]. This lowers the reaction barrier significantly. As a result, these reactions can be employed for an online calibration [27, 74]. A defined concentration of OH is generated with an ultraviolet (UV) lamp or an excimer laser. Since the reaction cascade has to be started in the inlet of the instrument, perturbations can be caused by the sampled molecules and also by flow perturbations dragging fractions of the calibration gas out of the inlet [7]. A strong chemical perturbation is caused by NO, if present in higher concentration, which amplifies the reaction of SO_2 and OH because it recycles OH. On the other hand NO_2 may consume the generated OH radicals.

Typical concentrations of sulfuric acid in the stratosphere are in the range of 10^5 to 10^6 molecules cm^{-3}. For a measurement the concentration of the dopant ions ($NO_3^-(HNO_3)_n$) should be 100 times greater than the sulphuric acid concentration. This concentration is determined by the reaction constant between the sulphuric acid and the analyte at typical reaction times of 0.15 s. [27]

$$SO_2 + OH + M \longrightarrow HSO_3 + M \tag{4.1}$$

$$HSO_3 + O_2 \longrightarrow SO_3 + HO_2 \tag{4.2}$$

$$SO_3 + H_2O + M \longrightarrow H_2SO_4 + M \tag{4.3}$$

Lovejoy et al. [85] have generated SO_3 from SO_2 (approximately 1 %vol) in oxygen passed over a hot filament. A similar pathway may be used for a simplified online calibration, provided the conversion efficiency is known and wall losses are low. This will be explored in forthcoming work.

4.1.2 Dopant species

The proper choice of the dopant species is important for an efficient and selective ionization. The high collision rates of about $10^9\,s^{-1}$ at atmospheric pressure and the elevated residence time of more than 5 ms in the high-pressure region leads to more than 10^6 collisions of each ion traveling to the MS detector. This estimation shows that most species reach their thermodynamic cluster equilibrium in the ion source because most thermodynamically allowed bimolecular ion-molecule reactions occur at the collision limit [135]. Especially water and most dopants are present at levels greater than 1 ppmv and they rapidly form clusters with bare ions. Ion clusters have the benefit, that they include the analyte ion and allow an easier identification of the last steps of the reaction cascade leading to the ion. It has to be ensured that the transfer stage does not destroy these clusters by CID to gain intact ion analyte clusters.

In addition chemical ionization suppresses chemical noise, which results from unwanted species being ionized and monitored. In the atmosphere ample concentrations of neutral molecules that form ions and ion-clusters with higher stability are present [128]. For example CO_3^- and NO_3^- ions are generated by reaction cascades starting with CO_2 and NO_2, which are discussed in chapter 4.3.3.2. These ions and their water clusters may act as secondary dopants which lead to a more complex reaction cascade that also depends on the water concentration, which changes the cluster size and thus the electron affinity of the clusters. This is not the case for the detection of sulfuric acid via $NO_3^-(HNO_3)_n$ clusters. Also for nitrate ions water ligands are observed [142], indeed the detection of sulfuric acid is independent of the water concentration within the error limits [136]. Ligand attachment may stabilize the charge of an ion, i.e. the electron affinity of the cluster is higher than the electron affinity of the bare dopant ion [86].

The smaller number of substances present in the UTLS compared to the lower troposphere may call for a lower selectivity but the dopant has to be selected

after a detailed study of the ion molecule chemistry. The choice is dependent on e.g. the analyte and it's concentration that needs to be measured, the resolution of the mass analyzer and the number of analytes, which are targeted. For this reason a large flexibility of the developed instrument particular in the ion source and transfer region is advantageous. It can easily be used with different dopants, just the calibration unit will have to be adapted. If cross contaminations are avoided also a fast change between the dopants for different analytes is possible. In the next four sections potential dopant ions will be discussed.

4.1.2.1 The nitrate ion, NO_3^-

Nitrate can be produced using a flow of HNO_3, which is ionized by deprotonation [41]. It can also be produced by the reaction of O_2^- with NO_2. The latter technique provides a cleaner environment because NO_2 is much less sticky as compared to HNO_3. Thermal electrons for the ionization of O_2 can be generated e.g. by a radioactive ion source or dielectric barrier discharge (DBD).

As seen from table 4.1 NO_3^- CIMS is very selective, since only few analytes are ionized, e.g., H_2SO_4 and a few organic peroxy radicals. Also OH and a few peroxy radicals can be indirectly measured reacting with SO_2 and H_2O to H_2SO_4. Table 4.1 provides an overview of possible analytes along with published detection limits.

Analyte	Ion	Detection limit	Literature
H_2SO_4	$HSO_4^-(HNO_3)$	4 ppqv	[25], [152]
OH (indirect)	$HSO_4^-(HNO_3)$		[25]
HO_2 (indirect)	$HSO_4^-(HNO_3)$	< 0.5 pptv	[41]
RO_2 (indirect) (R = organic rest)	$HSO_4^-(HNO_3)$		[41]

Table 4.1: Detectable analytes using NO_3^- as dopant with the main analyte ion (clusters), published detection limits and most relevant original publications. Detection limits partly apply to measurements at AP and may not be matched for UTLS measurements at reduced pressure.

4.1.2.2 The iodide ion, I^-

The iodide ion CIMS is of special interest because it allows simultaneous measurement of a range of analyte species present in the UTLS, e.g., bromine and chlorine species, as listed in table 4.2. I^- can be produced from CH_3I or CF_3I which are ionized by a polonium (^{210}Po) radiation source (4 slm N_2, 1 sccm (0.5 %vol CH_3I/N_2)) [130]. The iodide ion reacts readily with water to form an iodide water ion cluster, and also a dimer ion I_2^- (254) [101]. In most cases an iodide analyte cluster is detected.

Analyte	Ion	Detection limit	Literature
PAN		12 pptv (1 s)	[130]
N_2O_5		12 pptv (1 s)	[130, 47]
NO_3		12 pptv (1 s)	[130]
Br_2	I^-Br_2	7 pptv	[81]
BrO	I^-BrO	7 pptv	[81]
$HOBr$	I^-HOBr	7 pptv	[81]
HBr	I^-HBr	700 pptv	[81]
Cl_2	I^-Cl_2		[80]
$ClNO_2$	I^-ClNO_2		[80]
$BrCl$	I^-BrCl	2 pptv	[80]
$ClNO_3$	NO_3^-		[47, 43]

Table 4.2: Detectable analytes using I^- as dopant (as table 4.1).

4.1.2.3 CO_3^-

CO_3^- ions are readily produced by a corona discharge (2 slm N_2, 260 sccm O_2, 10 sccm CO_2) [129] or by atmospheric pressure photo ionization (APPI) [3]. Byproducts are CO_3^- water clusters [3]. In most cases a CO_3^- analyte cluster is detected.

CO_3^- also gives access to a number of relevant species in the UTLS, as shown in table 4.3. It may be a good alternative to NO_3^-, provide the sensitivity for sulfuric acid measurements is achieved.

Analyte	Ion	Detection limit	Literature
SO_2	$SO_3^-(H_2O)$, $SO_5^-(H_2O)$	30 - 40 pptv	[123], [42], [129]
NO_3	$CO_3^-(HNO_3)$	20 - 50 pptv	[42], [129]
HO_2NO_2	$CO_3^-(HO_2NO_2)$		[129]
H_2O_2	$CO_3^-(H_2O_2)$		[17], [142]
$ROOH$	$CO_3^-(ROOH)$		[17], [142]
HCN	$CO_3^-(HCN)$	2 pptv	[116]
SO_3	SO_4^-		[112]
H_2SO_4	HSO_4^-, $CO_3^-(H_2SO_4)$		[112]

Table 4.3: Detectable analytes using CO_3^- as dopant (as table 4.1).

4.1.2.4 SF_6^-

Compared to the previously presented dopants an even broader range of analytes are known for SF_6^- CIMS. Due to the less selective ion chemistry higher chemical noise is present, i.e., more ion signals are present, which reduces the sensitivity of the measurement. However, the broad range of analytes, presented in table 4.4, provides access to very interesting species such as SO_2 and BrO.

Analyte	Ion	Detection limit	Literature
SO_2	$F_2SO_2^-$, SF_5^-, FSO_2^-	20 pptv	[65], [48], [47]
HO_2NO_2	$NO_4^-(HF)$	5 pptv (1 min)	[65], [48]
BrO	BrO^-	1 pptv (1 min)	[80]
HNO_3	$NO_3^-(HF)$, $SF_5^-(NO_3)$	20 pptv	[48], [47]
O_3	O_3^-		[47]
Cl_2	Cl_2^-		[47]
NO_2	NO_2^-		[47]
HCl	SF_5Cl^-, $F^-(HCl)$		[47], [43]
Cl_2O	Cl_2O^-, Cl^-		[47]
$ClNO_3$	$NO_3^-(FCl)$, $ClNO_3^-$		[47]
N_2O_5	NO_3^-		[47]
CF_2O	CF_3O^-		[47]
CF_3CFO	$CF_3CF_2O^-$		[47]
$HOCl$	SF_5O^-		[47]
$HOBr$	SF_5O^-		[47]
Br_2O	FBr_2O^-		[47]
$BrNO_3$	$NO_3^-(FBr)$		[47]
$ClONO_2$	$F^-(ClONO_2)$		[43]
HBr	$HBrF^-$	100 pptv (100 Torr)	[29]
Br_2	Br_2^-	100 pptv (100 Torr)	[29]
HO_2	$SF_4O_2^-$		[29]
CF_3O_2	$CF_3O_2^-SF_6$		[55]
CF_3OH	CF_3O^-HF		[55]
CF_3O	CF_3O^-		[55]
SO_3	SO_3F^-		[54]
H_2SO_4	HSO_4^-		[54]

Table 4.4: Detectable analytes using SF_6^- as dopant (as table 4.1).

4.1.3 Ion source set-up geometry

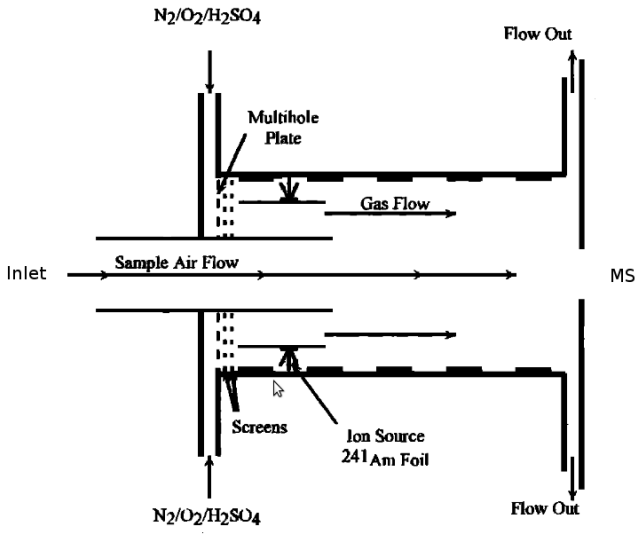

Figure 4.1: A schematic of the chemical ion source of Eisele, Tanner et al., adapted from [91].

Due to its high solubility sulfuric acid is generally of extremely low abundance in the gas phase, in the UTLS at mixing ratios of less than 100 ppqv [92]. Therefore successful instruments to measure this species are of utmost interest as a starting point of the development undertaken here. First measurements in the upper stratosphere have been made by Arnold et al. [4] using a rocket-borne mass spectrometer, which measured natural ions produced by cosmic rays. Later on, measurements have been made in the lower stratosphere using balloon-borne MS [99]. The state-of-the-art technique for UTLS sulfuric acid measurements is the use of an ion source generating NO_3^- ions as dopant for chemical ionization. A well established example is the laminar flow ion source developed by the group of Eisele and Tanner [26], as shown in figure 4.1. It will be discussed here as the starting point of the work presented here.

The radioactive (^{241}Am) foil provides a stable current of 5 MeV alpha particles. Ions are generated by the collision of alpha particles and gas molecules. The energy lost by an alpha particle of 1.2 MeV generating a charge pair depends on the species ionized, in pure nitrogen and oxygen energies of 36.6 eV and 32.5 eV have been measured, respectively [56, 50]. This energy also changes with the energy of the alpha particle [56]. So up to few tens of thousands

of ions can be generated by one alpha particle depending on the number of collisions of the alpha particle before it is absorbed by the wall.

The processes generating the primary ions are sketched in reactions 4.4 to 4.7. The ionization energy of nitrogen and oxygen molecules is 15.6 eV and 12.2 eV, respectively. The excess energy transfered by the alpha particle causes dissociation and excitation of molecules or causes a spontaneous emission of a photon. Excited nitrogen molecules can react with each other forming a N_4^+ ion (R 4.5). Thereby positive primary ions are produced, in air this is mainly nitrogen. Additionally excited nitrogen molecules and electrons are generated (R 4.4). The electrons attach to a molecule when they are thermalized by collisions, in air the electrons primarily attach to oxygen (R 4.6 and 4.7). [50]

$$He^{2+} + 2N_2 \longrightarrow He^{2+} + N_2^+ + N_2^* + e^- \tag{4.4}$$

$$N_2^* + N_2^* \longrightarrow N_4^+ + e^- \tag{4.5}$$

$$N_2 + e^- \longrightarrow N_2^* + e^-_{thermalized} \tag{4.6}$$

$$O_2 + e^-_{thermalized} \longrightarrow O_2^- \tag{4.7}$$

The primary ions react with the dopant and create a defined starting point for further reactions. Wall reactions are reduced by the dimension of the ion source and the laminar flow in the ion source. The ions are pulled into the center of the ion source by a DC-field gradient. [90] However, this technique cannot collimate ions efficiently (cf. chapter 3.3.9 and 5.1).

In the present work a new concept for the ion source is developed, the turbulent flow ion source. It is designated turbulent because there is no need to work in laminar mode. The turbulent flow ion source mixes the flows of the dopant ions and the analyte inside a 100 hPa ion funnel. The ion funnel collimates the ions while the neutral gas is pumped away. By this approach far less ions are lost in the first pumping stage as compared to the laminar flow ion source shown in figure 4.1.

4.1.4 Laminar flow ion source

The laminar flow ion source shown figure 4.1 provides a 19 mm diameter air inlet and a 44.5 mm diameter concentric ion flow tube. As long as the flow is kept laminar wall losses are kept to a minimum [85]. This design provides an almost wall-less sampling. Especially when sampling atmospheric air all inlet surfaces will be rapidly covered with reactive and sticky molecules in addition to aerosols.

The air is sampled through a stainless steal tube with an inner diameter of 1.9 cm. Synthetic air mixed with the dopant is added concentrically. To laminarize the outer flow fine mesh screens are used. The total flow through the ion source is regulated with a flow controller upstream of the pump for this sampling stage. The sample air flow is thus the difference between the outer flow and flow through the pump. With this technique both flows can be adjusted to keep the total flow in the drift tube laminar.

Ions are generated via a radioactive ^{241}Am foil positioned in the outer flow, 6 mm away from the wall. The ^{241}Am foil employed is an alpha particle source with an activity of 10 MBq. To push the ions into the middle of the ion source DC fields are used.

4.1.5 DBD plasma ion source

The dielectric barrier discharge (DBD) represents a "cold" plasma, which means that electrons are accelerated to a few electron volt while neutrals and ions remain at velocities corresponding to room temperature [72]. A dielectric plate positioned between the electrodes prevents arcing at the time the gas becomes electrically conductive. Therefore the breakdown voltage of the dielectric material is a key parameter. It can be controlled by the thickness of the layer and needs to be higher than the breakdown voltage of the gas. If the local field strength is high enough for ignition, the breakdown starts at many points on the electrode surface. Microdischarges (filaments), which are of nanosecond duration develop in the gas gap [144]. DBD plasmas are mostly generated with radio frequency (RF) power supplies. An RF-voltage or a pulsed DC-voltage can be used for this purpose [144]. The required voltage amplitude depends mainly on the electrode design, the dielectric material, the temperature, the

pressure, and the employed gas [78]. For nitrogen the initial reaction sequence leading to the primary ions are sketched in reaction 4.8 to 4.11 [151]. Nitrogen ions are generated by collision with electrons, thereby excited nitrogen ions with up to 19 eV have been observed spectroscopically [73]. Several metastable nitrogen molecules are present in the plasma with energies of up to 11.8 eV [73, 32]. Additionally N_4^+ ions are generated either by collisions of metastables or by reaction 4.10 [89, 5]. N_4^+ ions have only a small onset of 0.6 eV below the ionization energy of N_2^+ ions (15.6 eV) [5]. The complex behavior of the plasma, that also changes with the gas species present, requires well defined conditions to drive a stable DBD [75].

$$N_2 + e^- \longrightarrow N_2^+ + 2e^- \tag{4.8}$$

$$N_2^* + N_2^* \longrightarrow N_4^+ + e^- \tag{4.9}$$

$$N_4^+ + N_2 \longleftrightarrow N_2^+ + 2N_2 \tag{4.10}$$

$$N_2 + e^- \longrightarrow N_2^* + e^-_{thermalized} \tag{4.11}$$

For a proper operation of the DBD a self-sustained plasma should ignite upon voltage switch-on without further means. In general the plasma is generated by increasing the voltage amplitude above the breakdown voltage. Once the DBD is ignited enough seed electrons are available at the begin of the following cycle and lower voltages are sufficient to sustain the plasma. [75]

The electron density in the plasma is increased with rising permittivity of the dielectric material. The seed electrons that are required for the discharge may be "stored" on the dielectric surface. These stored electrons have a low binding energy. Therefore the dielectric material strongly influences the plasma. Some dielectrics provide a filamentary, others result in a more homogeneous discharge in different pressure ranges. Also the charge density changes the plasma characteristics [78]. In a filamentary plasma the number of filaments depends on the distance of the electrodes and the field strength. At AP a filamentary discharge is most common; with increasing voltage the number of filaments increases [108].

A high electron density in the plasma results in a higher temperature of ions and neutrals. DBDs with only one dielectric layer have the highest efficiency with regard to ion production [94]. One minimum requirement is that the dielectric material is stable with respect to the reactive species present in the plasma. In this context Al_2O_3 is a promising candidate, it has a relative permittivity of approximately 10, a dielectric strength of $17\,\mathrm{kV\,mm^{-1}}$ and has shown good chemical stability [20]. Also fused silica provides a dielectric strength of approximately $45\,\mathrm{kV\,mm^{-1}}$ at 5 kHz [28]. But the relative permittivity of fused silica is relative low ($\epsilon = 3{,}75$ [82]).

To sustain a stable plasma a frequency above a certain limit is required. When the frequency is to low, the dielectric layer is fully loaded with charge before the voltage reaches a maximum and seed electrons are lost in the long period between the pulses. At relatively high frequencies electrons and ions get trapped in the plasma. The frequency of a stable nitrogen plasma ranges approximately from 2 to 700 kHz at AP. A typical field strength for such a plasma is $27\,\mathrm{kV\,cm^{-1}}$. In nitrogen higher ion densities are reached but N_2 also has an 8 times higher breakdown voltage compared to helium operated discharges. On the other hand the pumping requirements for a nitrogen DBD are lower compared to helium. [23]

In order to use the DBD as an ion source, a gas flow is required. This also is advantageous for the discharge since the concentration of etching products (e.g. H or O), which potentially react with the metastables is decreased. More metastables are available for the production of seed electrons by Penning ionization (cf. equation 4.9). [35]

The major parts of the DBD can be represented by an equivalent circuit, shown in figure 4.2 [144]. Because the resistance R_g of the plasma is relatively low, the dielectric layer limits the current. Equation 4.12 is used to calculate the plasma current, i_0. The capacitance of the dielectric layer is calculated using equation 4.13 [94]. Here, U_0 is the applied AC-voltage, ω is the angular frequency, C_d is the capacitance of the dielectric material, ϵ_0 is the dielectric permittivity, ϵ_r is the relative permittivity, A is the area, and d is the thickness of the dielectric material respectively. Parasitic capacitances causing additional power consumption e.g. the shielded high voltage cable of the DBD may be included in the calculation [84].

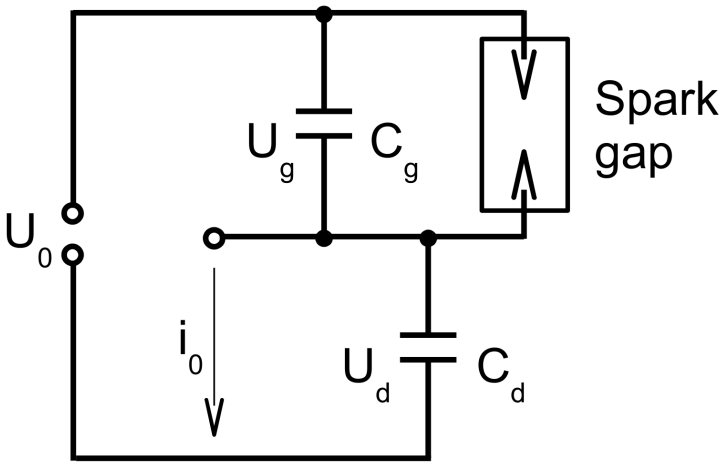

Figure 4.2: Equivalent circuit of the DBD, U and C designate the voltage and the capacitance of the dielectric material ("d") and the gas gap ("g").

$$i_0 \approx U_0 \, \omega \, C_d \tag{4.12}$$

$$C_d = \frac{\epsilon_0 \, \epsilon_r \, A}{d} \tag{4.13}$$

The capacitance of a shielded cable C_c is estimated using equation 4.14 [84]. Here, l is the length of the cable, r_o is the radius of the shield and r_i is the radius of the inner wire.

$$C_c = \frac{2 \, \pi \, \epsilon_0 \, \epsilon_r \, l}{ln \frac{r_o}{r_i}} \tag{4.14}$$

The required power to drive the discharge is estimated using equation 4.15 and the capacitance of the components, e. g. of the dielectric material. Here, U_0 is the amplitude of the applied voltage, ω is the angular frequency, and C is the total capacitance. A rough estimation shows that a shielded cable with typical $100\,\mathrm{pF\,m^{-1}}$ consumes $150\,\mathrm{W\,m^{-1}}$ at $10\,\mathrm{kV_{pp}}$ and $5\,\mathrm{kHz}$. Thus a DBD operated ion source should be placed in one box with the driving circuit. This grants good electrical shielding and reduces additional capacitances.

$$p = 0.5 \, U_0^2 \, C \, \omega \tag{4.15}$$

When a plasma is used as an ion source, pure gases (N_2, He, Ar) have to be employed. Using atmospheric air will strongly disturbs the desired ion chemistry. A nitrogen plasma generates excited nitrogen ions (mostly N_2^+) with an energy of up to 19 eV [73]. They will react easily with most other gases present.

Möhler et al. use a high frequency discharge ion source to generate CO_3^- [99]. They employ a mixture of 0.4 %vol CO_2 in oxygen. CO_3^- reacts fast with other reactants. Thus typically only products are observed, e.g. an ion analyte cluster. Reiner et al. use a similar reaction to generate NO_3^- [109]. They mixed NO_2 and oxygen in the ion source, which is a cleaner option than supplying a HNO_3/N_2 mixture by head-space sampling since HNO_3 is very sticky. The mixing ratio of HNO_3 in the ion source is not discussed by Reiner et al. but it is stated that mainly NO_3^- ions and ion clusters are generated.

4.1.6 Parameters of pipe flows

The Reynolds number Re is used in fluid dynamics, to characterize flow regimes. It is maybe calculated using equation 4.16. Here, v is the mean velocity of the gas, d is the inner diameter of the tube, ρ is density of the gas and η is the viscosity of the gas.

$$Re = \frac{v\,d\,\rho}{\eta} \tag{4.16}$$

Below the critical Reynolds number of 2320 a laminar flow is established after a distance L calculated with equation 4.17 [100]. Here, r is the inner radius of the pipe. The viscosity of nitrogen at 1013 hPa and 300 K is $\eta_0 = 17.9\,\mu\mathrm{Pa\,s}$ [82], and is constant at relevant pressures of 1013 hPa and lower [64]. The density of the gas reduces with the pressure reduction in the pipe and thus the velocity increases but the Reynolds number stays constant. The density of nitrogen at 1013 hPa and 273 K is $\rho_0 = 1.250\,\mathrm{kg\,m^{-3}}$ [34].

If the Reynolds number is above 2320, the flow tends to become turbulent. In contrast to the laminar flow the turbulent flow is affected by the roughness of the wall. At the wall of the pipe a laminar boundary layer forms, which is stable up to Reynolds numbers of 3.2×10^5 to 3×10^6. The thickness of the boundary layer depends on the velocity of the gas. [10]

$$L = 0.07\, r\, Re \tag{4.17}$$

$$\eta = \eta_0 \frac{p_1\, T_0}{p_0\, T_1} \tag{4.18}$$

4.1.7 Ion transfer through a capillary

All measurements described have been conducted at chocked flow conditions. This means the pressure difference over the capillary is high enough so the Mach number M = 1 is reached at the outlet.

For given P_0 at the inlet the critical pressure at the outlet of the capillary is calculated using equation 4.19 [150]. If the pressure P_1 at the outlet of the capillary is below the critical pressure, the flow through the capillary is independent of P_1. Here, d is the inner diameter of the capillary and l is the length of the capillary. Using the critical pressure P_{crit} the flow through the capillary f_{cap} is given by equation 4.20. Here, v_{Mach} is the Mach velocity, r is the inner radius of the capillary, T_{cap} is the temperature of the capillary outlet, P_{std} is the pressure at standard conditions and T_{std} is the temperature at standard conditions.

$$P_{crit} = \frac{4.51 \left(\frac{d^3\, P_0^2}{2\, l}\right)^{\frac{4}{7}}}{d} \tag{4.19}$$

$$f_{cap} = \pi\, r^2\, v_{Mach} \frac{P_{crit}\, T_{std}}{P_{std}\, T_{cap}} \tag{4.20}$$

The ion transmission through a capillary depends mainly on space-charge effects and the fluid dynamics in the capillary. Page et al. [104] used a 6.4 cm long capillary with a diameter of 640 µm and reported a transmission of up to about 50 % for a transmitted ion current of 10 nA. For turbulent and laminar flows the velocity near the wall decreases caused by the laminar boundary layer. So the ions need to diffuse through the laminar boundary layer to get in contact with the wall. The ion loss in the capillary can be explained within a factor of two by space-charge and diffusion. To estimate whether diffusion is dominated by space-charge equation 4.21 is used. If the charge density is higher than the calculated (ρ_{crit}), space-charge plays a role. Here, r_0 is the inner diameter of

Length [cm]	Inner diameter [mm]	Reynolds number	L [cm]	Transfer time [ms]	Critical pressure [hPa]	Flow [sccm]
15	0.5	2270	4.0	0.71	207	840
15	0.6	3100	6.5	0.69	236	1381
15	0.7	4050	9.9	0.68	263	2099
25	0.5	1697	3.0	1.24	155	629

Table 4.5: Parameters of selected capillaries for 300 K and 1013 hPa at the inlet.

the capillary, ϵ is the dielectric permittivity of the gas, ze is the charge of the ions, k is the Boltzmann constant and T is the temperature. [83]

$$\rho_{crit} = \frac{k\,T\,\epsilon}{ze}\left(\frac{2.405}{r_0}\right)^2 \tag{4.21}$$

Turbulence may also play a role for the ion transport through capillaries because the turbulence drives ions faster to the laminar boundary layer, which limits the ion loss [10]. The Reynolds number in the capillary remains constant with decreasing density (and pressure) over the capillary since the velocity increases proportionally.

Table 4.5 shows that Re for a capillary with a diameter of 0.5 mm and a length of 15 cm is right below the critical Reynolds number. After 4 cm the flow may become laminar in the optimal case but small perturbations, e.g. a nonuniform inner diameter or pressure fluctuations, can cause transition to a turbulent flow.

4.2 Experimental

4.2.1 Inlet and ion source design

In this work a new CIMS inlet has been designed. It is schematically shown in figure 4.3. At AP the inlet flow is restricted by a capillary. For planned measurements in the stratosphere ($\leq$ 100 hPa) it may be operated with a tube because no restriction of the flow is needed at pressures below 100 hPa. Dopant ions are generated using a DBD ion source (cf. chapter 4.2.2). The flow from

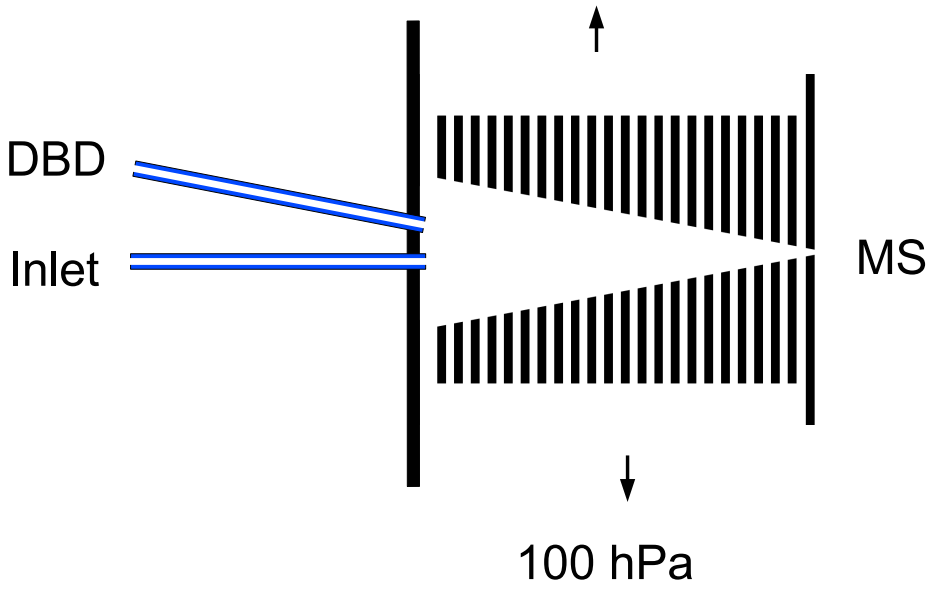

Figure 4.3: A schematic of of the newly designed chemical ion source.

the ion source and the flow sampled from the atmosphere are mixed at the entrance of a 100 hPa ion funnel. Analyte ions are generated and directly guided by the ion funnel. The effective potential of the ion funnel prevents the wall contact of the ions, while neutral molecules are pumped out of the funnel through the stacked funnel electrodes (for details see chapter 5). Wall reactions are not excluded, since the inlet capillary provides surface for wall reactions that calls for further characterization.

4.2.2 Setup of the new DBD ion source

In order to test the efficiency of a DBD ion source, a prototype has been developed, which has proven to work very well and was employed in the lab measurements. The containment of the high voltage electrode in the dielectric material provides increased safety-at-work, because the high voltage can cause serious injury. An improved final development will also be discussed. The design of the DBD ion source is finalized, but its characterization is still to be performed.

The prototype ion source has been constructed using a 6 mm swagelok cross

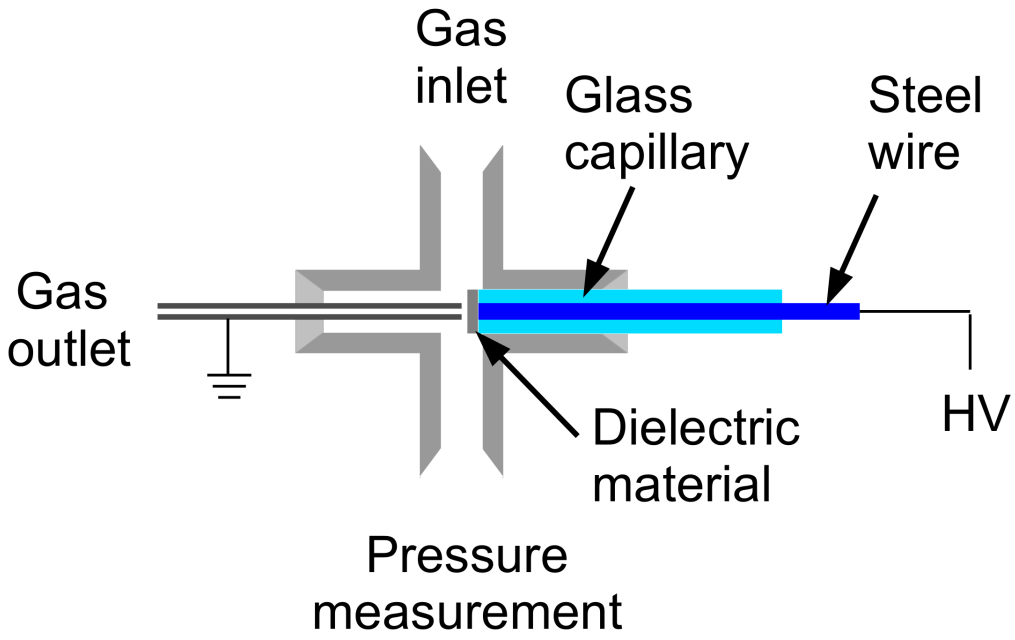

Figure 4.4: A schematic drawing of the DBD prototype.

(Swagelok Co., Solon, OH, USA). One side of the cross has been widened to a 6.2 mm bore to introduce a 6 mm glass capillary with an inner diameter of 2.2 mm. The glass capillary holds an electrode, a 2 mm metal rod. The capillary is capped with a 0.2 mm thick window of fused silica. The grounded counter electrode is a metal capillary (2 mm outer diameter) connected to the MS ("Gas outlet" in Fig. 4.4). The other two ports of the swagelok cross are used to measure the pressure in the plasma region and to supply the gas flow to the DBD.

4.2.2.1 DBD operation

The electrical requirements to drive the DBD are a high voltage amplitude to ignite the plasma in nitrogen ($> 12\,\mathrm{kV_{pp}}$) with a suitable frequency in the optimal region (2 to 100 kHz), which has been discussed in section 4.1.5. The availability of driving circuits determines the upper frequency limit. Three different circuits are used to drive the DBD.

For initial tests, which needed only low ion currents, a custom circuit was used. It works with a car ignition coil and provides 100 Hz at voltages of up to $10\,\mathrm{kV_{pp}}$. However, the low voltage amplitude renders the plasma ignition in

nitrogen rather difficult.

Much higher ion currents are reached with a low cost circuit, which provides 120 kHz at up to 30 kV_{pp} (PLASMSP_v2, HighVoltageShop, Graz, Austria). However, this circuit easily overheats and is not applicable for continuous operation.

Finally a Minpuls 2.1 circuit kit (Minipuls 2.1, GBS Elektronik GmbH, Großerkmannsdorf, Germany) is used for a sustained operation of the DBD. It provides 5 to 20 kHz at up to 20 kV_{pp} and additional features like a voltage and current monitor output. In addition, a burst frequency of 0 to 400 Hz is available. Hence pulse bursts in the kHz range can be repeatedly switched on (cf. section 4.3.2.2).

4.2.3 Improved DBD setup

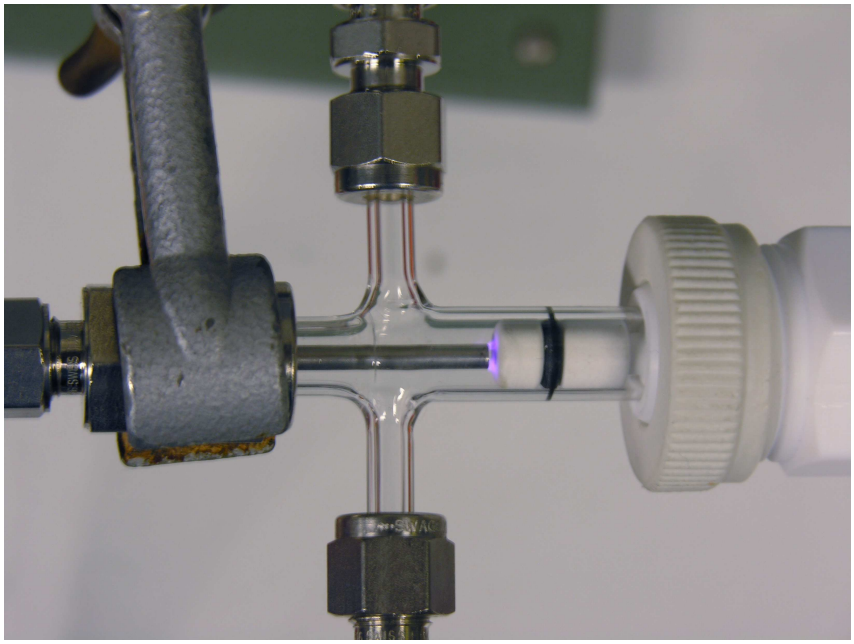

Figure 4.5: Photograph of the improved DBD setup with the plasma burning between the electrodes.

Two improvements have been implemented for the second version of the DBD. First, the swagelok cross is replaced by a glass cross to eliminate parasitic capacitances causing higher power consumption. Secondly, the high voltage electrode is replaced by a ceramics coated stainless steel electrode. This

electrode provides o-ring grooves for sealing to the glass cross. The stainless steel high voltage electrodes has been coated by a magnesium spinel by Daniel Mack (IEK-1 Materials Synthesis and Processing, Forschungszentrum Jülich GmbH) using a high velocity oxide fuel spray. The optimum thickness of the material has to be chosen to prevent a breakdown and to create a stable ceramic layer, because thicker layers easier fracture. A 300 to 400 µm ceramic coating provides such an optimum for voltage amplitudes up to approximately 15 kV_{pp}.

If not explicitly mentioned in the experiments the DBD prototype was used.

4.3 Results

The following sections present results obtained with the new inlet and ion source design. The subunits have been optimized and characterized but the final overall tests still have to be performed.

The new inlet design divides the ionization region and the reaction region of the dopant and the analyte, which may reduce chemical noise [40] because dopant ions with a defined internal energy are generated in the ion source before they are mixed with the dopant. The reaction of the dopant and the analyte occurs within the first ion funnel where the sampled gas stream is mixed with the dopant ions, produced by a DBD. The DBD provides an ion current output in the nA range and can be transported without special permissions since it lacks radioactive parts. In contrast to the ion source of Eisele et al. [26] also turbulent mixing is possible, leading to efficient mixing of dopants and analytes without the presents of additional DC field gradients.

4.3.1 CIMS inlet

In the laminar flow ion source of Eisele et al. [26] losses induced by flow perturbations are observed, since air stream caused additional turbulences in the inlet and the ion source. A nozzle has been used to stabilize the sampling gas flow. However, the sensitivity was reduced by 50 % [137]. At 100 hPa turbulences are less pronounced compared to atmospheric pressure because the Reynolds numbers are lower. In the present setup ions are kept in the ion funnel and guided to the sampling nozzle, which will additionally reduce such effects.

For measurements at 100 hPa an inlet pipe with increased inner diameter may be used because no pressure reduction is needed. However, measurements at AP require a flow restriction either by a nozzle or a capillary. The later may cause wall loss. The measurements of Page et al. [104] show that the ion transmission through a short capillary is about 50 % (cf. chapter 4.1.7). Lin et al. [83] argued that this transport is space charge and diffusion limited and can be explained within a factor of 2 by these processes. This is in agreement with the measurements of Page et al. which are above the critical value where space charge starts to dominate the transport (cf. chapter 4.3.2.1). These results indicate that only a fraction of ions hit the wall, while the ions are transported through the capillary. Even less neutral but sticky molecule will hit the wall because no space charge effect occurs. Additionally not every sticky molecule hitting the wall will be lost. Concluding, this leads to a transport of more than 50 % of neutral but sticky molecules for a short capillary of 0.6 mm inner diameter and a length of 6.4 cm (as used by Page et al.).

For the new inlet a capillary as flow restricting element will be tested and characterized. Additionally the gas flow in the capillary can easily be heated (cf. chapter 3.3.6). This is beneficial to protect the inlet of freezing up in field campaigns where cold gas in the stratosphere is sampled. However, heating has to be limited to temperatures below the evaporation temperature of aerosols. This way a stable operation of the instrument can most probably be assured.

4.3.2 Properties of the DBD

The prototype DBD establishes a stable ion source. With a plasma burning at the upstream port of the capillary, this geometry offers a good control of experimental parameters, e.g. the pressure in the plasma region. To create defined chemical conditions in the plasma only nitrogen or a defined gas mixture is delivered to efficiently generate the preferred dopant ions. If the dopant cannot be generated in the plasma, the dopant ion precursor might be injected into the capillary downstream of the DBD.

The gas flow through the plasma region is restricted by the capillary. Capillaries with different inner diameter have been tested to change the mass flow through the capillary while the DBD is driven at AP. Since the flow through the capillary depends on the temperature (cf. equation 4.20) temperature

control is necessary. In the laboratory a quite constant temperature is present but for a final version of the DBD a temperature controlled housing is needed. Additionally the sample gas flow must be kept at a constant temperature.

The DBD has been tested with 15 cm long capillaries with an inner diameter of 0.50 mm, 0.65 mm and 0.70 mm, resulting in flows of 0.85 slm, 1.82 slm and 2.03 slm respectively. The smallest capillary has a critical pressure of approximately 200 hPa at the outlet. The capillary is operated at chocked flow conditions with a pressure of 100 hPa in the first pumping stage of the mass spectrometer. The critical pressure further increases with a higher inner diameter of the capillary.

The measurements have shown that the ion current is independent of the pressure downstream of the capillary. The critical parameter in this case just is the flow through the capillary. As long as the flow is constant the ion current also seems to be nearly independent of the critical pressure downstream the capillary. If the pressure increases above the critical value only small changes are observed while the plasma keeps burning.

For the DBD prototype the generation of discharges inside the glass capillary electrode housing is also a limiting factor for the voltage used. For the second version of the DBD an adequate breakdown voltage of the surrounding glass cross is required for work safety. A driving voltage of 20 kV_{pp} results in field gradients of 10 $kV\,mm^{-1}$ between the high voltage electrode and the grounded Swagelok cross. The glass capillary housing of the high voltage electrode thus needs to withstand a higher breakthrough voltage. A fused silica capillary is used to increase the maximum driving voltage since the dielectric strength of glass is lower than for fused silica [131] (45 $kV\,mm^{-1}$ at 5 kHz [28]). Additionally the relative permittivity of fused silica (ϵ = 3,75 [82]) is lower compared to glass (e.g. Pyrex glass ϵ = 4,3 - 6,0 [82]). This results further in a lower power consumption through reduced capacitance.

For the prototype setup operated at 20 kV_{pp} and 5 kHz effective loads of 0.3 W for the discharge, 5 W for the electrode-housing gap and a minimum of 100 $W\,m^{-1}$ for a shielded cable are determined.

The protoype DBD has another disadvantage compared to the improved version, where the dielectric window is glued onto the capillary. In inclusions in the glue layer between the window and the high voltage electrode additional

plasmas ignite and potentially change the entire characteristics of the DBD.

Figure E.1 shows that the plasma erodes the glue in between the dielectric window and the capillary resulting in spark discharges after a few hours of operation.

The improved design eliminates inclusions because the ceramic is coated directly onto the stainless steel electrode.

4.3.2.1 DBD ion source output and stability

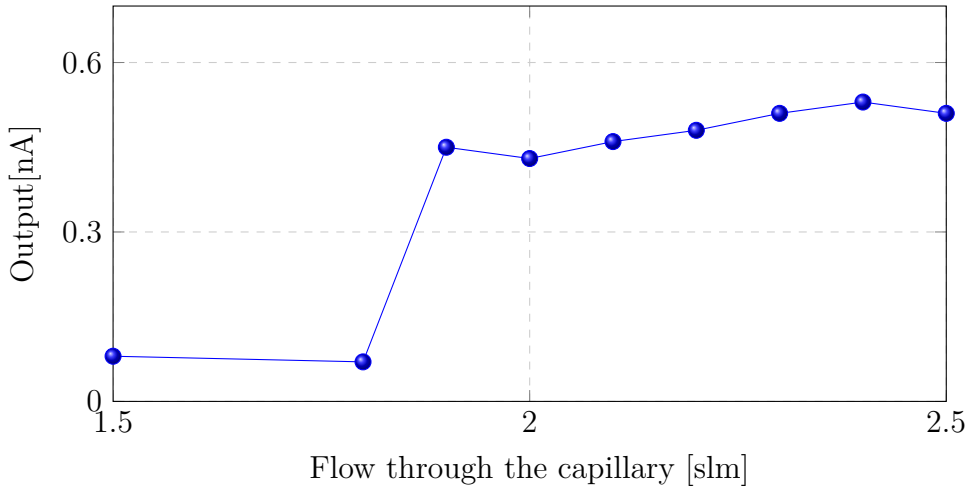

Figure 4.6: Ion current output of the DBD at defined flows through the sampling capillary with an inner diameter of 0.7 mm.

In order to quantify the charge output of the N_2 DBD it has been coupled to a Faraday cup, while driven with approximately 20 kV_{pp}, 120 kHz, at a distance of 0.5 mm between the electrodes. Capillaries with diameters of 0.5 mm and 0.7 mm mm have been used to sample the ions, both with a length of 22 cm. The pressure in the ion source changed with gas throughput and the diameter of the capillary and was in the range of 500 to 1500 hPa. The capillary was biased with 10 V for the ion current measurement. The ion current was measured with a custom electrometer. The comparison with a Keithley Picoampere Meter (model 485, Keithley Instruments, Ohio, USA) showed differences of 0.1 nA, which is is in the error range of the Picoampere Meter.

Measurements with pressures slightly higher than the critical pressure at the outlet of the capillary showed no significant changes in the ion current

output while the flow through the capillary was constant. However, below a critical flow the ion current abruptly decreased by more than an order of magnitude. The maximum charge output of the 0.5 mm capillary under the described conditions is 0.1 nA and 0.5 nA for the 0.7 mm capillary. The charge output increased approximately linearly as the driving voltage was increased (cf. section 4.3.2.2).

Increasing the driving voltage to 30 kV_{pp} increased the ion current output of the 0.5 mm capillary from 0.1 to 0.8 nA. This is consistent with the measurements of Page et al [104]. They transfered 10 nA using an electrospray ion source with 50 % transmission through a 0.5 mm capillary which is shorter than the capillary used here. So the ion current will increase further using a shorter capillary.

The transport through the capillary is limited by space charge or by diffusion, which dominates the transport through the capillary below a critical ion density (cf. chapter 4.1.7). For the capillary with an inner diameter of 0.5 mm and a flow of 800 sccm this critical value is 0.16 nA. The measurements of Page et al. [104] suggest that the loss in the 22 cm long capillary is larger than 50 %. Therefore the ion density at the capillary inlet seems to be slightly higher than the critical value and so the transport is limited by space charge.

For the ion currents of 0.1 to 0.5 nA with critical flows of 0.7 slm and 1.9 slm ion mixing ratios of approximately 1 ppbv are calculated. This shows that the ion current under the described conditions is proportional to the critical flow through the DBD.

4.3.2.2 Ion current and driving frequency

For this experiment a capillary with 0.5 mm inner diameter and a length of 22 cm has been used at an upstream pressure of 1100 hPa using nitrogen. The DBD has been operated using a non-metal cross to reduce the capacitance. As shown in figure 4.7, the resonance coil was changed for each frequency to operate the DBD in a resonant mode. In contrast to theory the ion current output increased at lower frequencies. This may be due to the fact that less energy is coupled into the plasma, because of some mismatching which depends on e.g. the capacitance of the dielectric layer. Further adjustment of the resonant coil and the capacitance of the DBD is required. However, comparable high ion

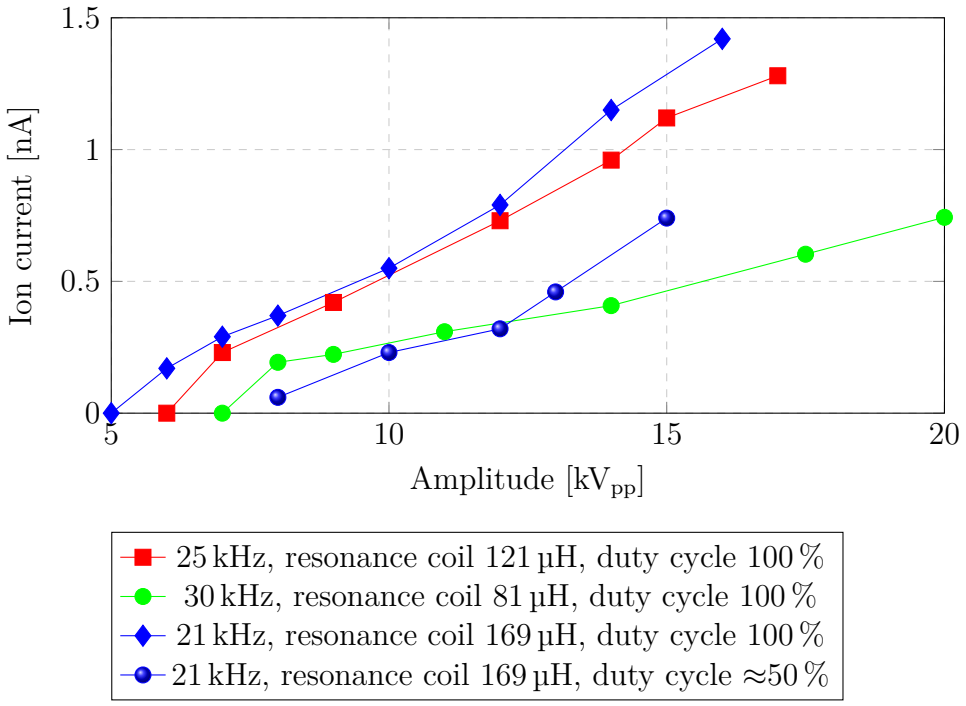

Figure 4.7: Ion current output of the DBD as function of the voltage amplitude for different frequencies.

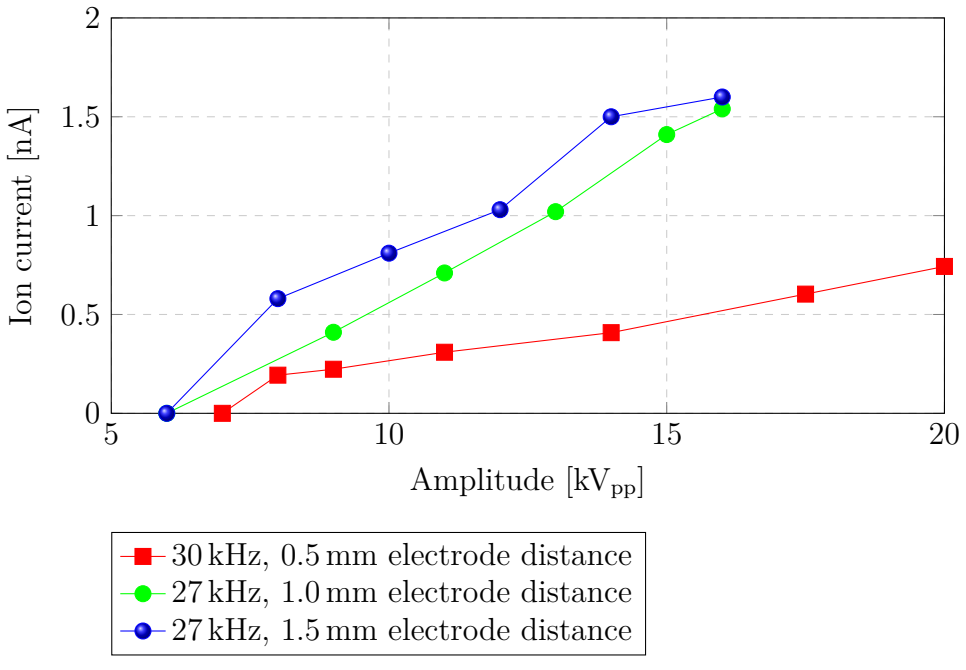

Figure 4.8: Ion current output of the DBD as function of the voltage amplitude for different electrode distances.

currents in the nA range have been reached already and further optimization is possible, e.g. by the use of a dopant. The ion current increased approximately linearly with the driving voltage amplitude. Reducing the duty cycle of the DBD to 50 %, using the burst frequency, consequently reduced the ion current by 50 %.

Figure 4.8 shows that increasing the distance between the electrodes increases the ion current, which seemed to change the plasma characteristics increasing the charge output.

Different discharge modes are possible in the DBD. The AP DBD in nitrogen represents a Townsend discharge; the ionization level is thus not high enough to reach the regime of an AP glow discharge. However, e.g. using helium such a transition is possible. The current density in the AP glow discharge is approximately a factor 10 higher compared to the Townsend discharge [88]. This is in agreement with the measurements presented here since no jump has been observed in the ion current increasing the voltage amplitude.

The DBD is also a bipolar ion source in nitrogen. Positive ions are generated in excess because the main discharge products are positive nitrogen ions and electrons, which are lost at least in the capillary after the plasma or do not leave the plasma field. In synthetic air the measured ion current decreases approximately to zero because oxygen captures the electrons and transports them through the capillary. So positive and negative ions are almost in equilibrium. Due to this fact it is difficult to measure the real output of positive ions of the DBD because the nitrogen gas also includes impurities capturing negative charge.

4.3.2.3 Ignition voltage

As shown in figure 4.2, the DBD may be represented by two capacitors connected in series. The first capacitor is the dielectric layer, which should prevent a breakthrough. The second capacitor represents the gap. Field gradients above the breakthrough voltage of the gas are needed to ignite the plasma. Wagner et al. listed typical operation conditions of the DBD [144]. Typical reduced field strengths for the first breakdown at AP in nitrogen and RT are approximately 150 Td. The ignition voltage of the presented DBD with a gap of 0.5 mm is 12 kV_{pp}. Many uncertainties are involved in the calculation of the field strength

in the gas gap, e.g. the effective plasma area, the capacity of the dielectric layer and impurities in the gas. So, a comparison to the theoretical values is hardly possible.

The ignition voltage depends on the voltage gradient between the electrodes. A sharp ridge at the capillary electrode was found to reduce the ignition voltage due to higher local field gradients [145]. A significant change in the ion output has not been found when comparing the ridge with a plane capillary end. For an increased electrode gap a higher ignition voltage is required. Also, increasing the distance between the electrodes from 0.5 to 0.9 mm a decrease of about 30 % of ion output has been found.

4.3.3 DBD ion generation

4.3.3.1 SF_6^- and related dopant ions

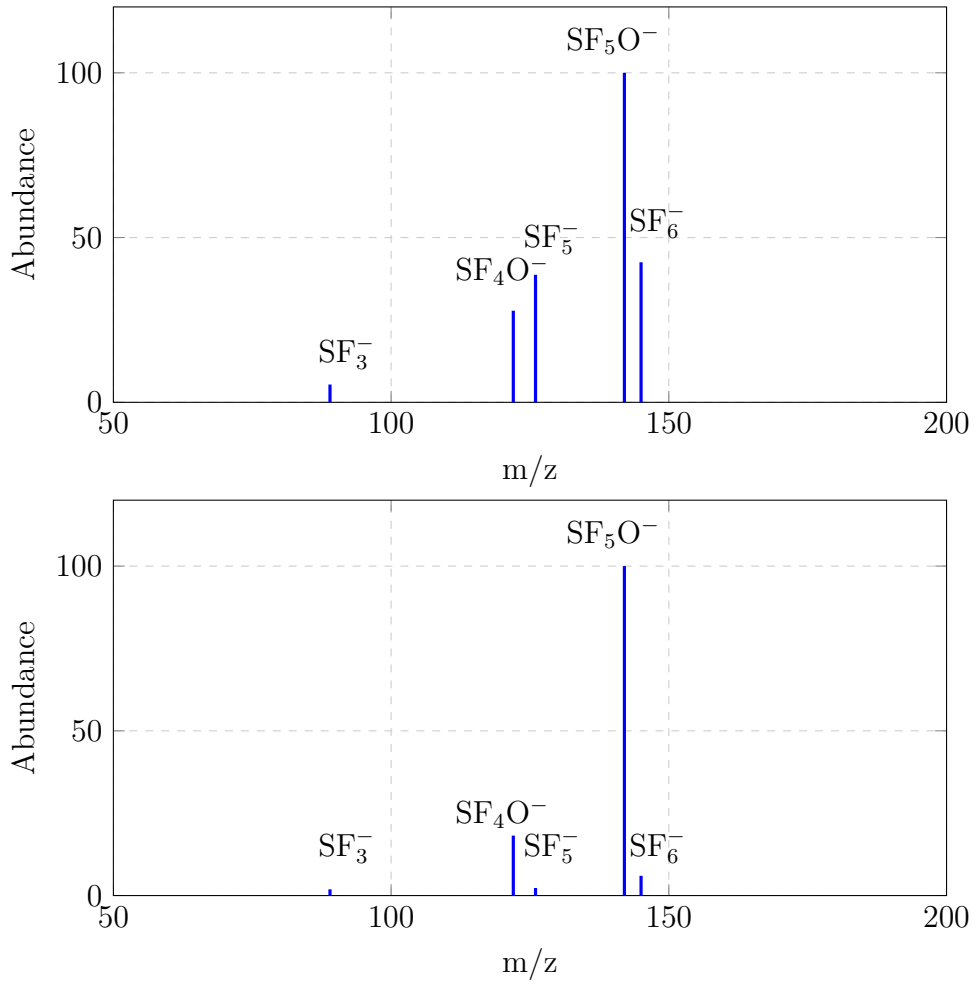

Figure 4.9: Mass spectrum of SF_6 and nitrogen flowing through the DBD with a SF_6 mixing ratio of 200 ppmv (top) and 2000 ppmv (bottom) in nitrogen, each spectrum has been scaled to the most intensive peak.

SO_2 can be measured using SF_6 as a dopand. Therefore in a first experiment the generation of SF_6^- ions has been tested. Results are presented in figure 4.9. SF_6 is added to a flow of 700 sccm of the nitrogen in concentrations of 200 ppmv and 2000 ppmv flowing through the DBD. The experiment shows that the concentration of SF_3^-, SF_5^- and SF_6^- ions decreases with higher mixing ratios. Electron attachment is typically done with thermalized electrons, in a plasma also electrons with higher energies are present. This electron energy

likely leads to a dissociation of SF_6 or a dissociative electron attachment to SF_6, e.g. SF_6^- is likely generated at electron energy below 0.1 eV, SF_5^- at electron energies below 0.1 eV and SF_x^- (x = 2-4) at electron energy higher than 4 eV [77]. The dissociation and the dissociative electron attachment of SF_6 is sketched in reactions 4.22 and 4.23,

However, high concentrations of SF_5O^- and SF_4O^- were found. Therefore it seems that the SF_6^- reacts with oxygen species in the nitrogen (5.0). Also reactions with oxygen species forming SF_nO^- ions are well known [77, 47].

$$e^- + SF_6 \longrightarrow SF_x + (6-x)F + e^- \tag{4.22}$$

$$e^- + SF_6 \longrightarrow SF_x^- + (6-x)F, \quad [x = 2-6] \tag{4.23}$$

4.3.3.2 CO_3^- and NO_3^- dopant ions

The generation of CO_3^- and NO_3^- dopant ions was achieved as follows. Figure 4.10 shows a measurement of CO_3^- ions and $CO_3NO_3^-$ ion clusters generated in the DBD. The gas flow was 700 sccm synthetic air mixed with 3.5 sccm CO_2. This leads primary to the production of CO_3^- ions but also NO_3^- is produced by the oxidation of nitrogen. The production of NO_3^- ions might be further amplified by the addition of NO_2, as discussed in section 4.1.2.

O_2^- and O^- ions are generated in the plasma via dissociative electron attachment and three body electron attachment. These oxygen ions oxidize CO_2 and NO_2 producing NO_3^-, CO_3^- and HCO_3^-, as sketched in reactions 4.24 to 4.30 [128]. HNO_3 is formed by the reaction of OH and NO_2 [146] and by the attachment to CO_3^- a $CO_3HNO_3^-$ cluster is formed. CO_2^- is most likely formed by electron attachment. The origin of a HCO_2^- is not clear.

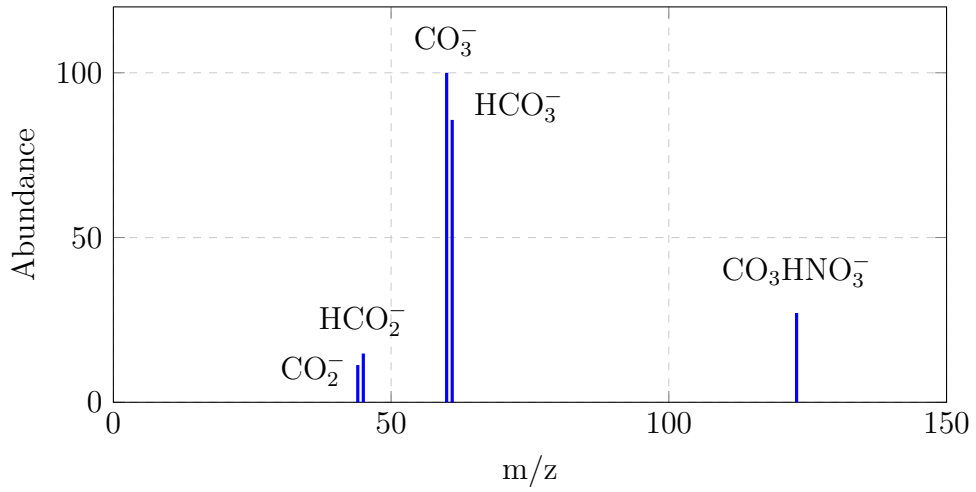

Figure 4.10: Mass spectrum of CO_2 and synthetic air flowing through the DBD with a CO_2 mixing ratio of 5000 ppmv, the spectrum has been scaled to the most intensive peak.

$$O^- + CO_2 + M \longrightarrow CO_3^- + M \tag{4.24}$$

$$O^- + O_2 + M \longrightarrow O_3^- + M \tag{4.25}$$

$$O_2^- + O_3 \longrightarrow O_3^- + O_2 \tag{4.26}$$

$$O_3^- + CO_2 \longrightarrow CO_3^- + O_2 \tag{4.27}$$

$$O_3^- + NO_2 \longrightarrow NO_3^- + O_2 \tag{4.28}$$

$$CO_3^- + NO_2 \longrightarrow NO_3^- + CO_2 \tag{4.29}$$

$$OH^- + CO_2 + M \longrightarrow HCO_3^- + M \tag{4.30}$$

Chapter 5

CIMS transfer stage

An ideal ion transfer stage would transfer all ions to the mass spectrometer while only neutral molecules are pumped away. Additionally the ions would not be altered by any reactions, so the mass spectrum represent the ion composition in the ion source. In this chapter a real transfer stage is discussed and its advantages and limits are characterized.

5.1 Theory of ion transfer elements

5.1.1 The RF-only quadrupole

Quadrupoles can be used as mass filters with a combination of RF- and DC-fields. RF-only quadrupoles are commonly used as transmission devices because they transfer a wide mass-to-charge (m/z) range of ions.

The Mathieu equation (equation 5.1) is a linear second order homogeneous differential equation describing several physical applications, e.g. vibrations of an elliptical drum, the stability of a floating boat or the stability of the motion of single ions in the quadrupole [111]. The parameters "a" and "q" are characteristic for the given application. For the quadrupole a describes the influence of the DC-field, which is not used by the RF-only quadrupole and q (equation 5.2) describes the interaction of the ions with the RF-field [97]. In this case, X is the temporal and Y is the geometric term. In equation 5.2, ω is the angular frequency ($\omega = 2\,\pi\,f$, f = frequency), V_{RF} is the voltage amplitude of the RF-field, m is the molecular mass of the buffer gas (N_2: 28 u), ze is the

charge of the ion, and r_0 is the inner radius of the quadrupole.

$$\frac{d^2\,Y}{d\,X^2} + [a - 2\,q\,\cos(2\,X)]\,Y = 0 \tag{5.1}$$

$$q = \frac{2\,ze\,V_{RF}}{m\,\omega^2\,r_0^2} \tag{5.2}$$

Equation 5.1 explains the transmission of a broad range of masses (m/z) by the RF-only quadrupole, i. e. if the orthogonal direct current (DC)-field between the rods is zero (a = 0).

However, the Mathieu equation does not include the collision of ions with neutral background molecules, which leads to collisional "cooling". The ions move on a helical flight path with the phase of the RF-field. By collisions with the neutral background gas the ions lose velocity in axial and radial direction. This confines the ions to the center axis of the quadrupole at a minimum radial oscillation. The damping of the ions in axial direction can be compensated by an axial DC-gradient that is applied by a segmentation of the quadrupole.

The RF-only quadrupole is a low mass filter [22]. The low mass cut-off is estimated in first approximation using equation 5.2 and 5.3, exact values are obtained by simulation or measurements [140]. Here q_u is the q parameter for m/z = 1.

$$(m/z)_{low} = 1.1\,q_u \tag{5.3}$$

High q-values lead to ion activation [22] due to high effective potentials. However, high potential also increases the charge density Q_{max} that can be stored by the quadrupole under ideal conditions [139]. Here, ϵ_0 is the dielectric constant, and V_{RF} is the zero-to-peak voltage.

$$Q_{max} = \pi\,\epsilon_0\,V_{RF} \tag{5.4}$$

Equation 5.5 correlates the collision time of the buffer gas and the ion. τ is the collision relaxation time, which depends on the mass of the ion M, the mass of the buffer gas m and the time between collisions $t_{col} = 1/n\sigma\nu$. Using the collision relaxation time the high pressure limit for the quadrupole is estimated ($\omega\tau >> 1$). Above the high pressure limit the effective RF-field is suppressed.

The low mass cut-off (equation 5.3) of the quadrupole is valid below the high pressure limit and does not change significantly with the buffer gas used [138].

$$\tau = \frac{3\,(m+M)}{4\,m}\,t_{col} \tag{5.5}$$

The high mass cut off is not sharp and two cases have to be discussed. Case 1: The minimum beam diameter, which increases with the mass of the ion, is larger than the nozzle diameter D. This relation is given by equation 5.6. Here, k is the Boltzmann constant, T is the buffer gas temperature, M_{min} is the low mass cut off, and M_{max} is the high mass cut off. Case 2: The length of quadrupole L_Q is too short for sufficient ion cooling ($L_{kT} > L_Q$; $L_{kT} \sim u_0\tau$ with u_0 = initial ion velocity) because a certain path L_{kT} is needed to reach the minimum beam diameter [138].

$$\omega = \frac{8\sqrt{k\,T\,M_{max}}}{D\,M_{min}} \tag{5.6}$$

5.1.2 The ion funnel

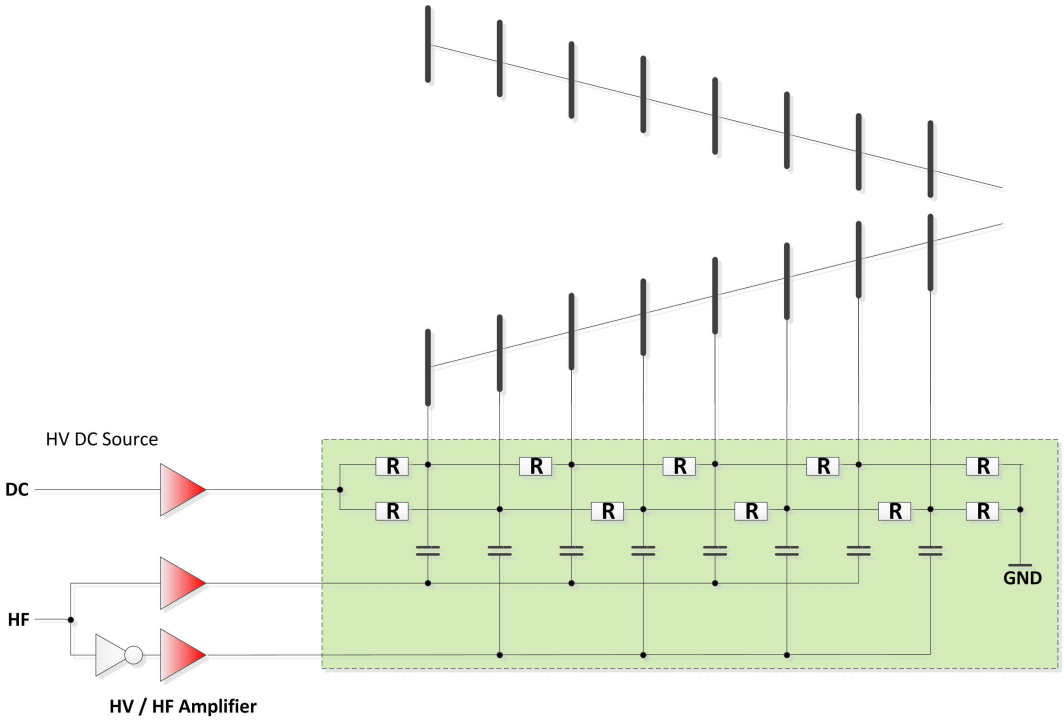

Figure 5.1: A schematic sketch of the ion funnel (top) and the attached resistor and capacitor network (bottom). Source: Heinz Rongen, ZEA-2 Electronic Systems, Forschungszentrum Jülich GmbH

Ion funnels are typically used to focus ions at pressures exceeding 1 hPa where fluid dynamic motion makes it challenging to guide the ions [125]. State-of-the-art funnels may be used at up to 30 hPa [51]. Experiments with an ion funnel capturing ions at up to 140 hPa have been published [102] but in helium and without noticeable gas flows. This particular ion funnel had electrode distances of 0.5 mm, it worked up to 180 V_{pp} and a frequency of 800 kHz. The effectiveness γ of the RF-field is thus only 1 % (cf. chapter 5.3.1).

The ion funnel consists of a stack of narrow ring electrodes with decreasing inner diameter in downstream direction. A radio frequency voltage (see Fig. 5.1) is used to create steep electrostatic field gradients between the electrodes that trap the ions inside the ion funnel. The maximum field gradient is reached between the electrodes while the inner volume of the ion funnel remains nearly field free. To transport the ions downstream in the ion funnel, the neutral gas flow or an additional DC field gradient are used.

The electrostatic field decreases with the third power of the inverse distance to the electrodes [61]. An ion approaching the electrode experiences stronger fields that attract and reject it with the rf frequency. The oscillating field generates an effective potential that rejects the ions to regions of weaker fields independent of their mass [33]. The penetration depth into the effective potential is determined by the mass, the charge and the initial velocity of the ion. As in the quadrupole, the ion loses velocity by collisions and repels to the near field free inner volume of the ion funnel.

The distances between the electrodes of a quadrupole are typically much larger and the field gradients counteracting the fluid forces are lower. This is the reason why a quadrupole performs worse at higher pressures [61].

Important parameters of the ion funnel are the geometry and the operating parameters, which are peak voltage amplitude and frequency. To prevent that the gas flow chokes in the ion funnel a sufficient drift distance is important because the pumping cross section increases with the length of the ion funnel [66]. The pitch angle is not very critical because the performance of the ion funnel mainly depends on the force generated by the electrostatic field. If the electrostatic fields can stop the ions in the gas flowing with Mach velocity, the performance of the ion funnel is at optimum. Recently, a planar ion funnel has been presented [141] and also the other extreme, a stacked ring ion guide has been realized [39].

The smallest inner diameter of the ion funnel should be smaller or equal to the downstream nozzle diameter to grant a good ion transfer through the nozzle. The electrode distance should be smaller than the smallest inner ring diameter otherwise ions with low m/z are lost in the exit region of the ion funnel [125]. The distance between the electrodes is typically 0.5 mm, comparable to the thickness of the electrodes. The maximum diameter of the funnel needs to be large enough to capture most ions.

The maximum effective potential generated by the RF-field in the ion funnel is estimated using equation 5.7 [36]. This potential characterizes the field strength that affects the ions and is used to compare different operation modes of the ion funnel. Here, ω ($\omega = 2\,\pi\,f$, f = frequency) is the angular frequency, V_{RF} is the voltage amplitude of the RF-field, m is the molecular mass of the ion, q is the charge of the ion, and $\delta = d/\pi$, where d is the centre-to-

centre distance between the electrodes. This equation however neglects that the ion motion is choked if the ions encounter collisions. Tolmachev et al. introduced an additional term γ [138]. It specifies the effectiveness of the RF-field suppression near the high pressure limit. This results in the effective potential U_{eff}, which takes into account the ion mass, the electrode distance and the pressure dependence.

$$U_{max} = \frac{q\,V_{RF}^2}{4\,m\,\omega^2\,\delta^2} \tag{5.7}$$

$$\gamma = \frac{\omega^2\,\tau^2}{1+\omega^2\,\tau^2} \tag{5.8}$$

$$U_{eff} = \gamma\,\frac{q\,V_{RF}^2}{4\,m\,\omega^2\,\delta^2} \tag{5.9}$$

The ion transmission through the ion funnel is space charge limited, as in the quadrupole. Equation 5.10 gives the maximum charge that can be stored in an ion funnel [139]. Here, ϵ_0 is the dielectric constant, ρ is the minimum inner radius of the ring electrodes, V_{RF} is the RF-voltage amplitude, and d is the spacing between the electrodes.

$$Q_{max} = 0.5\,\pi^2\,\epsilon_0\,\rho\,V_{RF}/d \tag{5.10}$$

5.1.3 Effective ion temperature

The ion temperature T_{eff} in a quadrupole field is calculated using equation 5.11. Here, m_r is the reduced mass (($\mathrm{m}_g\,\mathrm{m}$)/(m_g+m)), m_g is the mass of the gas molecules, T is the temperature of the background gas, q is the charge of the ion, V^* is the effective potential, m is the mass of the ion, and k is the Boltzmann constant. However, no collisions with neutral gas particles are involved. Therefore the bath gas pressure needs to be low, such that the RF ion velocity is not dominated by collisions. The upper limit can be estimated via the collision relaxation time τ (cf. chapter 5.1.1) and the angular frequency ω. For a frequency of 1 MHz the upper pressure limit is approximately 1 hPa ($\omega\,\tau >> 1$). Below this pressure limit the drift motion is in phase with the RF-field. The pressure limit increases further with increasing frequency. Above

the pressure limit the effective field is essentially suppressed by the medium. [138]

$$T_{eff} = \frac{m_r}{m_g} T + \frac{m_r \, 2 \, q \, V^*}{m \, 3 \, k} \tag{5.11}$$

Since space charge plays a significant role, only a fraction of the calculated maximum ion charge is transferred through a quadrupole without significant ion heating. At increased ion densities ions are pushed towards the electrodes by space charge, where the effective potential is higher. For higher multipoles the maximum ion density that is transferred is increases with the number of poles (2N). The maximum ion density that is transferred through a multipole also increases with the effective potential, which inevitably leads to an increased ion heating. The preferred option to prevent ion heating is to increase the number of poles. It is noted though that the most confined ion beam is generated by a quadrupole.

An option to overcome this limitation is the usage of an ion funnel. The transfer is also limited but it is comparable to a higher order multipole, cf. equation 5.12. Here, ρ is the minimum inner diameter of the funnel, and d is the distance between the electrodes.

$$N = \pi \, \rho / d + 1 \tag{5.12}$$

Concluding, a number of parameters are determining the actual ion temperature. Also the cluster distribution caused by RF-fields is non-Maxwellian [18], hence only an effective temperature can be estimated. Obviously the ion temperature is best judged from kinetics of ion molecule reactions, e.g. an ion cluster reaction, or by the activation energy of ion molecule reactions, e.g. fragmentation reactions, which can be compared with known data.

In combination with ion transfer stages often the term "soft" ion transfer is used. This term is misleading since a real soft transfer is only reached without the use of electrostatic fields in a brought pressure range used in common transfer stages. Such an instrument will lack of sensitivity but is superb for the research of sensitive ion bound clusters. Sensitive transfer stages use transfer elements in sensitive pressure regions causing ion energies of approximately 1 eV. To reveal this in a effective temperature, this is above 1000 K and shifts water cluster to their smallest size (m/z = 19). But also in this context often

the term "soft" is used. Here the meaning is that most fragmentation reactions and collision induced reactions are avoided keeping the ion energy slightly below 1 eV.

5.1.4 Breakdown voltage

Burm et al. [14] present data for the breakdown voltage in nitrogen as a function of the field gradient, which is very similar to the breakdown voltage in air. These data are used to determine the breakdown voltage in the following. In addition the pulse rise time and the frequency influence the breakdown voltage [93]. With higher frequencies the breakdown voltage decreases by up to 20 % for gap distances < 0.5 mm. [107]

Electrodes with small radii of curvature however show significant deviations of the ideal behavior. Also the electrode material can influence the breakdown voltage to approximately 10 %. Relative humidity below the condensation level has only minimal effects. [118]

5.2 Experimental

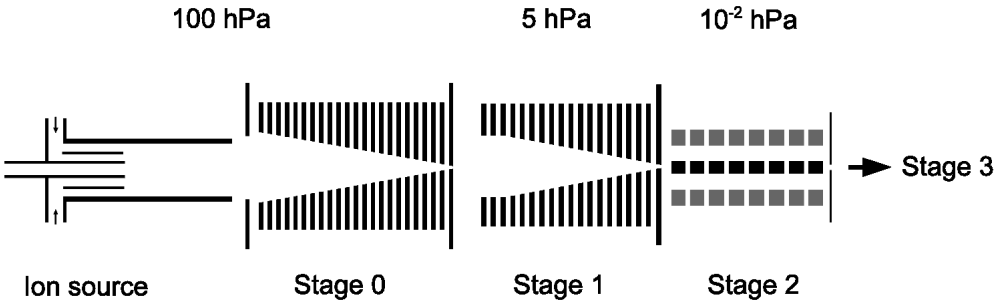

Figure 5.2: A schematic drawing of the CIMS transfer stage. Stages 0 - 2 are described in chapter 5.2. For stage 3 see section 2.3.3.

The transfer stage consists of the two ion funnels shown in figure 5.2 and a segmented quadrupole. Downstream of stage 3 an rf-quadrupole guides the ions further. The pressure in stage 3 is 10^{-5} hPa, virtually no ion molecule

collision are present and transmissions of 1 are readily achieved. Therefore this stage is not further discussed in this chapter.

5.2.1 The 100 hPa ion funnel (Stage 0)

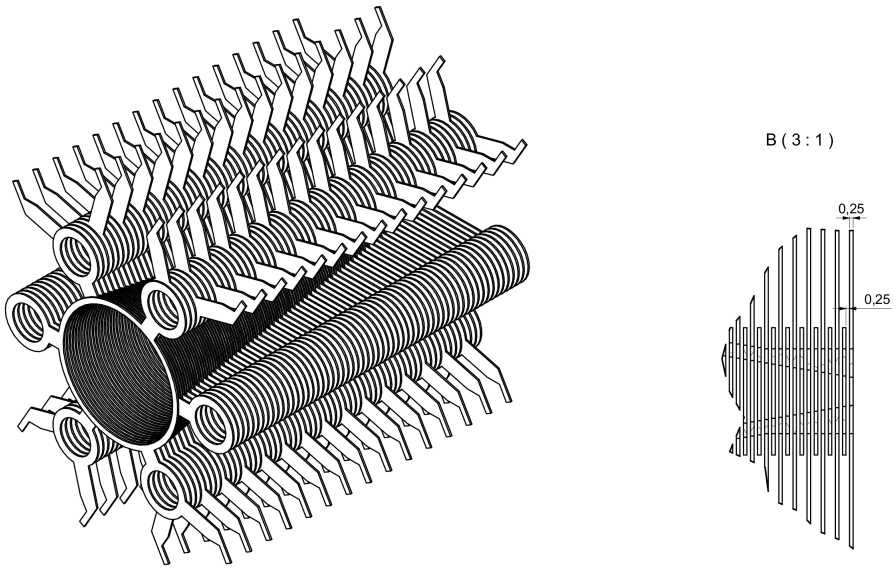

Figure 5.3: 3D-view of the ion funnel electrodes. B is a cut through the electrodes at the downstream part of the ion funnel.

The ion funnel consists of 120 electrodes, comprised of 0.25 mm thick stainless steel. It has been designed based on the experience gained from the 5 hPa ion funnel described in section 5.2.2. The distance between the electrodes has been reduced to 0.25 mm. Therefore stainless spring steel is used to protect the electrodes against bending during the assembly process. Additionally the electrodes are gold coated (2 µm) to protect against chemical corrosion. Also soldering of the electrodes to a printed circuit board becomes much easier. The inner diameter of the electrodes linearly decreases from 20 to 2 mm, which is also the nozzle diameter. The total length of the ion funnel is 60 mm.

The total capacitance of the ion funnel is minimized in order to reduce the overlapping area of the electrodes with opposite RF signals (cf. figure 5.3). Six fixtures arranged hexagonally are used for the electrodes, three for each of the

phase shifted RF-signals. The distance between the electrode rings is 0.25 mm; the distance between the electrodes at the fixture is 0.75 mm since only every second electrode is mounted on each fixture. The electrodes are separated by 0.75 mm thick polyether ether ketone (PEEK) spacers, which are positioned as a comb (cf. figure 5.4). This renders the mounting easier and increases the spatial accuracy and the stability of the funnel. The electrodes and spacers are stacked on a M3 threaded rod isolated by a 6 mm glass tube.

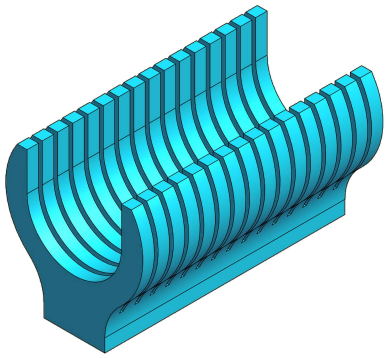

Figure 5.4: A drawing of the PEEK spacers holding the funnel electrodes.

The electrodes are soldered to printed circuit boards with a capacitor and resistor network, which connects all electrodes. Four printed circuit boards are soldered to 2 electrode rows each. This design provides 1.75 mm in-between the contacts of each row, as sketched in figure 5.3.

The RF power supply for the ion funnel is designed by Heinz Rongen and Markus Dick, ZEA-2, Electronic Systems, Forschungszentrum Jülich GmbH. Initially the frequency is generated using a signal generator (AFG3102, Tektronix, Oregon, USA) and a RF power amplifier (2100L, Electronics & Innovation, Rochester, USA). Two phase-shifted signals (by 180°) are generated using the output of a "balun". The origin of the word balun is "balance" and "unbalance". The balun transforms an unbalanced signal oscillating relative to ground, in a balanced signal, i.e. two signals oscillating relative to each other. The balun consists of three interacting inductors, which establishes a resonant circuit in combination with the capacitance of the ion funnel. Without matching the resonant frequency is approximately 5.3 MHz and a large fraction of the energy is reflected to the amplifier. Matching is achieved by connecting a 130 nH

inductor to each of the phase-shifted channels. This changes the resonant frequency to approximately 9 MHz and reduces the reflected power to a minimum. The 100 hPa ion funnel is thus driven at 9.2 MHz and up to 200 V_{pp} using only 23 W, which is very well suited to airborne deployment. Further work is needed however to increase the voltage amplitude to approximately 300 V_{pp}.

5.2.2 The 5 hPa ion funnel (Stage 1)

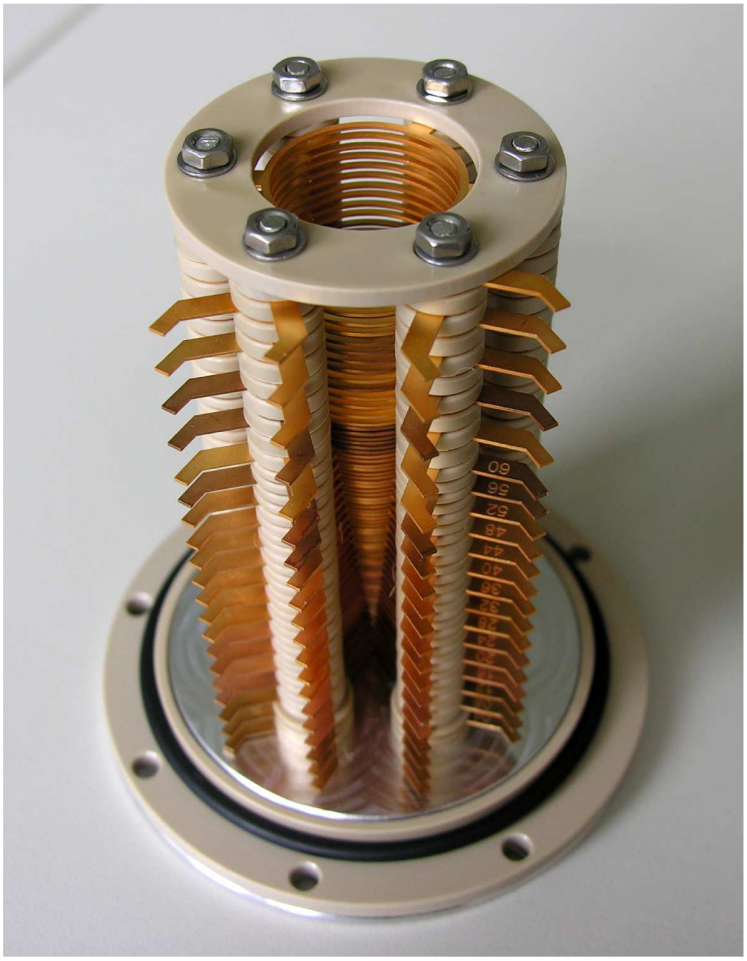

Figure 5.5: Photograph of the 5 hPa ion funnel before the printed circuit board is soldered to the electrodes.

The ion funnel operated at 5 hPa consists of 80 electrodes comprised of 0.5 mm thick gold coated stainless steel. The first 20 electrodes have an inner diameter of 22 mm and a distance of 1 mm between the electrodes. The other 60 electrodes have linearly decreasing inner diameters down to 2 mm, which is the nozzle

diameter. These electrodes have a distance of 0.5 mm, resulting in a total length of the funnel of 89.5 mm.

As already discussed in chapter 4.1.5 for the DBD, the power that is needed to drive the ion funnel is directly proportional to its capacitance. Thus the overlapping area of the electrodes is reduced in order to reduce the capacitance. As for the 100 hPa ion funnel six fixtures for the electrodes are used, three for each of the phase shifted RF-signals. Additionally, the outer diameter of the ion funnel electrode ring has been kept as small as possible (cf. Fig 5.6).

Figure 5.6: The two smallest electrodes of the ion funnel with the PEEK isolators.

As compared to individual full ring mounting thicker spacers between the electrodes can be employed since six fixtures are used. These spacers (isolators) are made of PEEK. The electrodes and spacers are stacked on a M3 all-thread rod isolated by a 6 mm glass tube.

A capacitor and resistor network connects all electrodes. The resistor network establishes a linear decreasing DC potential in the funnel and decouple the RF-voltage from the DC power supply. The capacitor network decouples the RF-supply from the DC-voltage. The network is implemented on a printed circuit board, which is directly soldered to the gold coated electrodes. Only four vacuum feed-troughs are needed, two for the RF-signals and two for the

DC-voltage at the entrance and the outlet of the ion funnel.

The ion funnel voltages are controlled by a signal generator (AFG3102, Tektronix, Oregon, USA), an amplifier (A400DI, FLC Electronics, Partille, Sweden) and a custom resonant circuit (ZEA-2 Electronic Systems, Forschungszentrum Jülich GmbH). The resonant circuit is used to stabilize the output of the amplifier at a given frequency. This way up to 180 V_{pp} voltage amplitude can be generated at a frequency of 1.8 MHz.

5.2.3 The segmented Quadrupole (Stage 2)

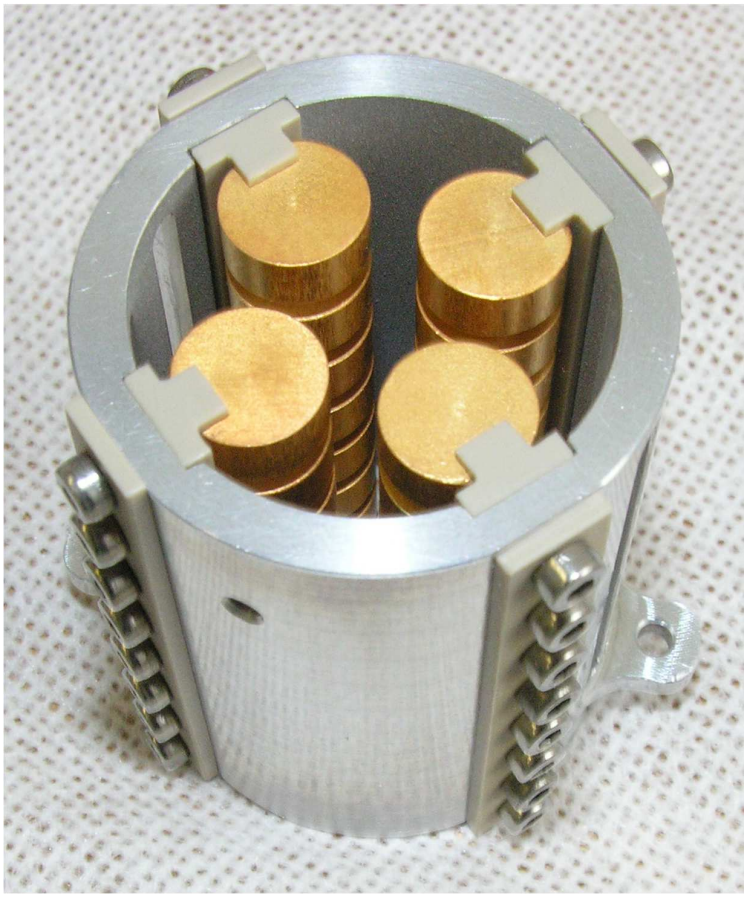

Figure 5.7: A picture of the segmented quadrupole before the printed circuit board is mounted to the electrodes.

The segmented quadrupole consists of 32 gold coated aluminum electrodes. The electrodes are oriented and isolated by a PEEK rail. The inner diameter ($2\,r_0$) of the quadrupole is 9 mm. The total length of the quadrupole (entrance

to exit) is 58 mm. Each electrode has a length of 5 mm and a diameter ($2\,r$) of 5.2 mm, as suggested by Dawson et al. [22], ($r \approx 1.1468\,r_0$). The distance between the segments is 2 mm, in order to keep the local field gradients between the electrodes comparably low. The effect of the fringing fields at the inlet and outlet of the quadrupole is kept low when the distance between the nozzle electrodes and the quadrupole is small. Since the electrostatic field lines continue in axial direction with minimum bending. In the optimum case the distance is below $0.125\,r_0$ [49], however the intensity of the fringing fields starts to decrease for distances below $1.0\,r_0$. For the presented setup a distance of 2 mm was chosen ($\approx\ 0.5\,r_0$). The jacket of the quadrupole holds the PEEK rail carrying the electrodes and has an inner diameter of 15.9 mm ($R = 3.54\,r_0$ [22]). Additionally the jacket reduces the pumping cross section in order to increase the pressure in the quadruple for a sufficient collisional cooling. The pumping cross section is $0.6\,\mathrm{cm}^2$. The flow f into the quadrupole is limited by a 2 mm nozzle, thus a flow of $5.5\,\mathrm{hPa\,L\,s^{-1}}$ at 5 hPa upstream of the nozzle is reached. This is calculated by the equation $f = a\,v_{Mach}\,p_0$. Here, a is the area of the nozzle, v_{Mach} is the Mach velocity, and p_0 is the pressure upstream the nozzle. Rearranging the equation for p and using an area of $0.6\,\mathrm{cm}^2$ for the pumping diameter of the quadrupole jacket, results in a calculated pressure of around 2×10^{-2} hPa in the quadrupole.

The printed circuit board (CGC Instruments, Chemnitz ,Germany) is comparable to the board used for the ion funnel (cf. chapter 5.2.2) with the exception that the electrodes are electrically connected to the printed circuit board by screws. The quadrupole is driven by a frequency generator [19] (RFG50-4.6MHz, CGC Instruments, Chemnitz ,Germany), supplying up to $900\,\mathrm{V_{pp}}$ at 4.6 MHz.

5.2.4 Ion trajectory calculations

For the optimal design of the ion funnels ion trajectory calculations have been performed by combining fluid dynamic and electrostatic calculations.

5.2.4.1 Fluiddynamic calculations

The fluiddynamic calculations were done by Armin Afchine (IEK-7, Forschunszentrum Jülich GmbH) using Ansys CFX 14 (Ansys, Inc., Cecil Township,

Pennsylvania, USA). Ansys CFX is a powerful computational fluid dynamics program package. The boundary conditions in the ion funnel are well known so the Ansys results should be reliable. This reasoning is corroborated by the successful operation of the ion funnels. The boundary conditions used for the fluid dynamic calculations are given in appendix A.1.

The Shear Stress Transport (SST) has been modeled based on the k-ω turbulence model [95]. To overcome typical solver problems each calculation has been initially set up with a conservative physical model and more robust discretization to generate a first estimate of the flow field. These results have been used as starting point for the final setup using the complete physical model and higher order discretization. For a better accuracy of the results the double precision solver has been used for all calculations. The domains have been meshed with an irregular mesh containing approximately 7 million elements and 1 million nodes, using the Ansys meshing tool.

5.2.4.2 Electrostatic calculations

For electrostatic calculations the SIMION software package (Scientific Instrument Services, Inc., Ringoes, New Yersey, USA) was used. With its Lua programming language interface the oscillating fields of ion funnels and quadrupoles are simulated. Additional Lua packages for collision simulations are available. "SIMION Version 8.1 is a software package primarily used to calculate electric fields and the trajectories of charged particles in those fields when given a configuration of electrodes with voltages and particle initial conditions, including optional RF (quasistatic), and collisional effects." [127]

5.2.4.3 Electrostatic calculations with collisions

To recognize the fluid dynamics within the electrostatic calculations collisions are simulated in Simion using the fluid dynamic data output from Ansis CFX. The data are linearly interpolated to the Simion mesh and tailored to the Simion geometry by a Python program presented in appendix B. These data are then used for the collision model.

Simion provides two collision algorithms, the HS1 algorithm, which is a hard-sphere collision model and the SDS algorithm, which employs collision statistics. The HS1 algorithm calculates the mean free path depending on

the pressure and the temperature. The fluid dynamic calculations are used to calculate the velocity, temperature and pressure of the background gas. Single collisions are simulated to model the interaction of ions with the background gas.

The SDS collision algorithm employs collision statistics to simulate multiple collisions per time step. In this approach the simulation time is considerably decreased, which enables simulation at AP on a personal computer. Combined viscous ion mobility and random ion jumping is used [2]. Up to pressures of 5 hPa the HS1 collision algorithm is used, above this threshold the SDS collision algorithm may be used.

For the simulation of the ion funnel at 100 hPa the time steps of the SDS collision algorithm have been reduced to matched to the driving frequency of the ion funnel. This also reduced the amount of ions that are simulated per time step and increases the time consumption of the simulation. A simulation of 40 ion trajectories took about 2 weeks on a state-of-the-art personal computer.

5.3 Results

5.3.1 The 100 hPa ion funnel

The proper function of the ion funnel is sensitive to high gas velocities, as further discussed in chapter 5.3.2. For a given mass flow an increased pressure in the ion funnel leads to lower gas velocity. Higher field gradients are necessary to compensate increased velocities (cf. section 5.3.2), however at the expense of increased collisional ion activation.

The first step for the realization of an ion funnel operated at 100 hPa is an assessment of the limiting operating parameters. As already discussed, the breakdown voltage for nitrogen at 100 hPa and an electrode distance of 0.25 mm is approximately 360 V [14], i.e. the upper limit of the RF-amplitude (V_{pp}) of the ion funnel. The Paschen curve does not linearly decrease with lower gap distances, cf. figure 5.8. Higher field gradients can be reached with smaller electrode distances, but these are mechanically challenging. Further details about the breakdown voltage were discussed in chapter 5.1.4.

The 5 hPa ion funnel works properly with RF-amplitudes from 60 to 120 V_{pp}

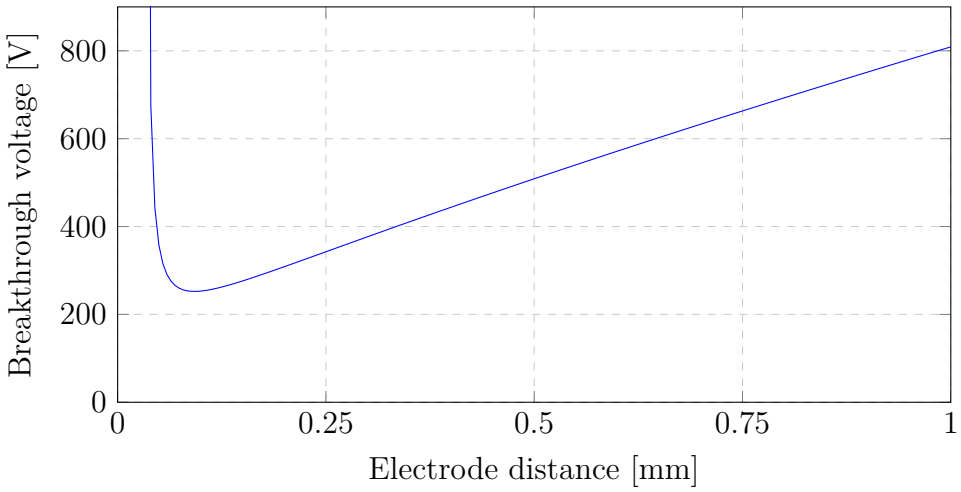

Figure 5.8: Breakdown voltage in nitrogen at 100 hPa [14].

(cf. figure 5.15), while the operation of the 100 hPa ion funnel is limited by the breakthrough voltage of 400 V_{pp} for 0.25 mm electrode distance. However, Table 5.1 shows that U_{eff} (see equation 5.9) is in the same range for both ion funnels.

Voltage amplitude 100 hPa ion funnel [V_{pp}]	Voltage amplitude 5 hPa ion funnel [V_{pp}]	U_{eff} [V]
200	57	233
300	86	523
400	114	930

Table 5.1: Voltage amplitudes of the ion funnels calculated for a given effective electrostatic potential. The 5 hPa ion funnel has electrode distances of 0.5 mm and is operated at 1.8 MHz. The 100 hPa ion funnel has electrode distances of 0.25 mm and is operated at 10 MHz.

It is obvious that the frequency of the RF-field has to be scaled up by the same value as the collision frequency increases with rising pressure. At 5 hPa ion funnels work properly at frequencies starting around 500 kHz [51]. Scaling this value to 100 hPa a frequency of 10 MHz is needed for a proper operation of the ion funnel. Additionally the high pressure limit ($\omega\tau >> 1$) is estimated, which has been discussed for the quadrupole (cf. section 5.1.1). At 100 hPa the

collision time is approximately 1×10^{-8} s. With a frequency of 10 MHz, and an ion of mass 100 u in a nitrogen buffer gas (28 u), this leads to $\omega\tau = 4.4$, which is close to the high pressure limit. The effectiveness of the RF-motion γ is 0.6, the 5 hPa ion funnel has a γ of 0.95 at 1.8 MHz, so slightly higher effective field strengths are needed at 100 hPa.

An important limiting factor is the power consumption of the ion funnel at 100 hPa. Here proper circuit design, e.g. using a resonant circuit is needed that lowers the power consumption [19].

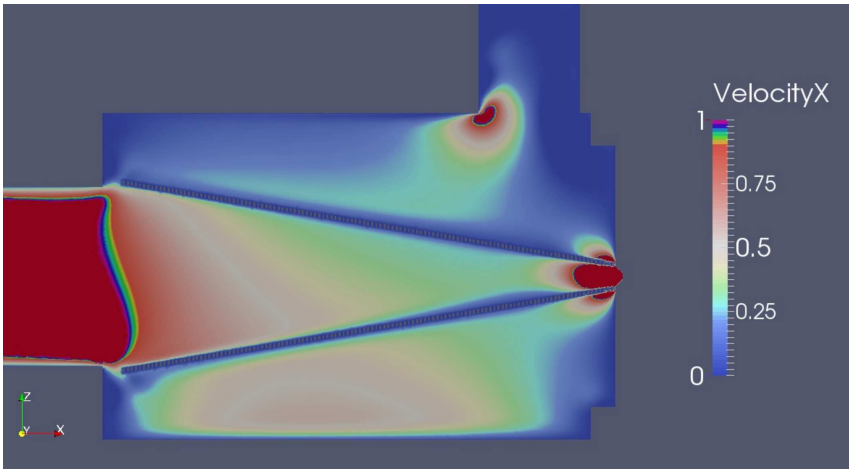

Figure 5.9: A cut through the simulated flow field of the ion funnel at 100 hPa with the velocity in x-direction in $\mathrm{m\,s^{-1}}$.

Figure 5.9 shows results of the fluid dynamical simulations made to understand the corresponding characteristics of the funnel. A gas velocity of $1\,\mathrm{m\,s^{-1}}$ at the inlet and an inlet diameter of 22 mm has been used. As shown this leads to generally low flow velocities even in the downstream region of the ion funnel.

The performance of the ion funnel is governed by the velocity of the neutral gas, especially between the funnel electrodes. In combination with an expanding gas stream the same problems as seen for the ion funnel at 5 hPa (see section 5.3.2) may appear. So the flow and consequently the velocity must be kept below a critical value in order to increase the performance of the ion funnel. In the presented simulation a laminar flow of 2 slm has been used.

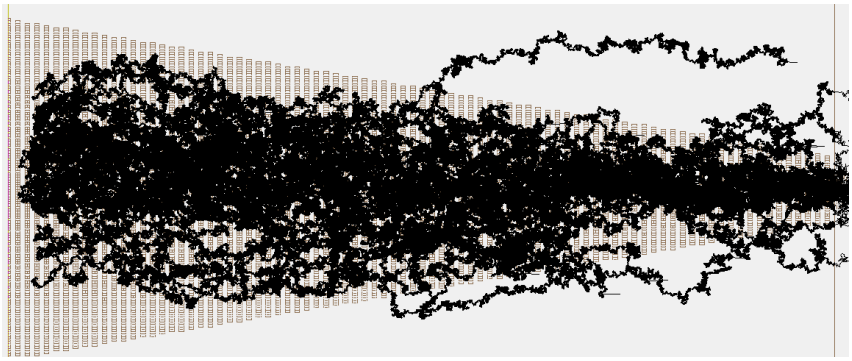

Figure 5.10: A cut through the Simion SDS ion trajectory simulations of the ion funnel at 100 hPa driven with 300 V_{pp} and 10 MHz. In black the ion trajectories of 40 ions with mass 100 are shown.

An electrostatic simulation including collision model has been performed using Simion with the SDS collision model. Figure 5.10 shows results, which indicate that most ions reach the exit of the ion funnel. Therefore the RF-field capturing the ions in the funnel seems to be sufficient and no additional DC-field is needed to drive the ions downstream. Further simulation runs with voltage amplitudes from 200 to 500 V_{pp} and 10 MHz at 100 hPa are presented in appendix A. These runs show that even increased transmission factors are possible above 300 V_{pp}. In addition, it is shown that voltages above the breakdown voltage (360 V) are required to reach a transmission of 1.

5.3.2 The 5 hPa ion funnel

as discussed in chapter 5.2.2 the capacity of the ion funnel has been reduced to a minimum. A relatively small capacity of approximately 200 pF has been reached. Ibrahim also reduced the capacitance of their ion funnel of approximately similar dimensions but lowered the capacity of their ion funnel to only 1.6 nF [51]. This demonstrates the favorable design of the ion funnel presented in this work.

The breakdown voltage at 5 hPa for electrode distances of 0.5 mm is exceeding 700 V [14]. Higher voltage amplitudes for the ion funnel than used in the presented measurements may be used, but at the expense of extensive CID.

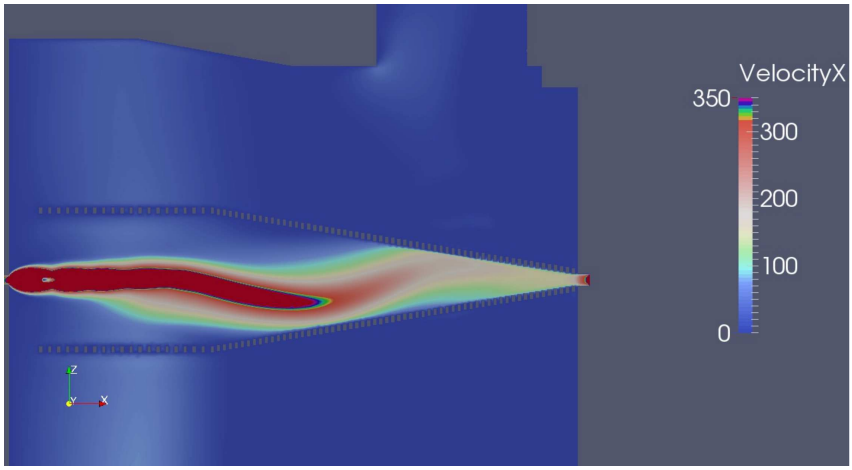

Figure 5.11: A cut through the simulated flow field of the ion funnel at 5 hPa with the velocity in x-direction in $\mathrm{m\,s^{-1}}$.

Figure 5.11 shows that a jet expansion exists downstream of the inlet nozzle to the exit of the ion funnel, resulting in gas velocities above $100\,\mathrm{m\,s^{-1}}$. This is in agreement with the measurements, presented in section 5.3.5, that show that the ions are solely driven downstream by the fluid and no additional DC-field is needed. The measurements of the ion transmission, discussed in section 5.2, indicate that the gas throughput is a critical parameter for the transmission of the ion funnel. The impact pressure of the jet at the narrow end of the funnel causes relatively high velocities between the electrodes, driving the ions out of the funnel, as shown in figure 5.12. This effect is reduced by a lower gas flow through the ion funnel. Alternatively a "jet disrupter" may be used to diffuse the jet [61].

Figure 5.13 shows two regimes of slightly increased pressure caused by the expanding gas (upstream) and by the impact pressure (downstream). Kelly et al. [61] have reported 2 to 3 fold pressure increase due to impact pressure, which obviously is not the case for the present ion funnel.

In appendix A.5 further results with a shorter ion funnel are shown. These simulations have been performed with the same boundary conditions as previously. Figure A.17 shows that a higher pressure (6 hPa) is reached inside the ion funnel because of the reduced pumping cross section. Additionally the jet causes higher velocities ($>200\,\mathrm{m\,s^{-1}}$) downstream in the narrow exit region of the ion funnel, as shown in figure A.18. Figure A.17 demonstrates that the higher pressure in the ion funnel causes higher velocities, especially at the inlet

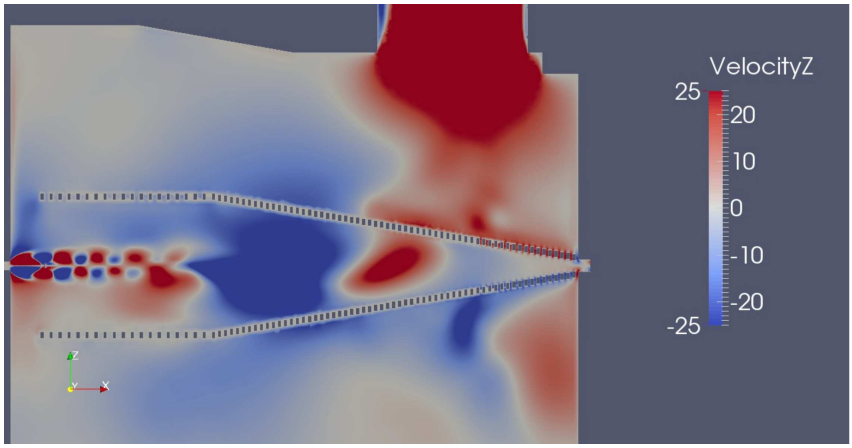

Figure 5.12: A cut through the simulated flow field of the ion funnel at 5 hPa with the velocity in z-direction in $\mathrm{m\,s^{-1}}$.

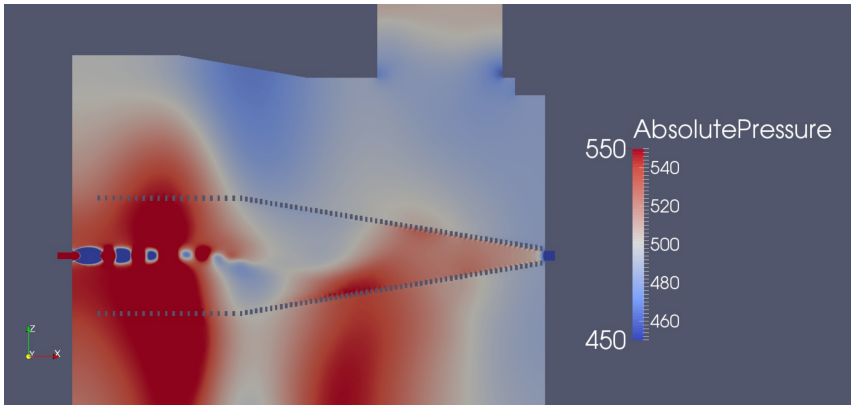

Figure 5.13: A cut through the pressure field of the ion funnel at 5 hPa with the pressure in Pa.

with 5 mm space between the first electrode and the housing allowing the gas to escape and dragging ions out of the funnel.

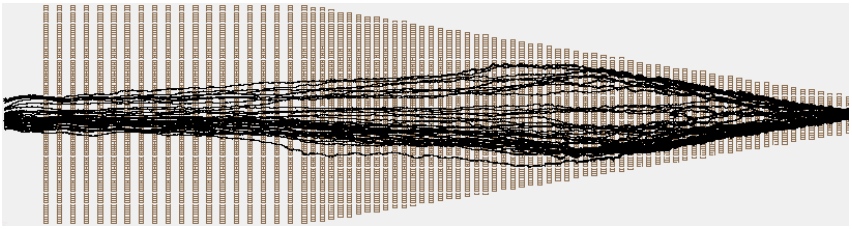

Figure 5.14: A cut through the SIMION HS1 ion trajectory simulations of the ion funnel at 5 hPa driven with 180 V_{pp} and 1.8 MHz. In black the ion trajectories of 40 ions with mass 100 are shown. The velocity vector of the fluid dynamic simulation is multiplied by 0.5 compared to figure A.7.

Electrostatic simulations for the ion funnel driven at 5 hPa have been performed using the fluid dynamic results in combination with the HS1 collision model of SIMION. Figure 5.14 shows results for a run at 180 V_{pp} operating at 1.8 MHz with reduced velocity compared to the original fluid dynamic simulation. The comparison between the simulated ion trajectories presented in appendix A.3 and A.4 shows that the required voltage amplitude may be reduced by a factor 2 if the velocity in the ion funnel is also reduced by the same amount. This is in agreement with theory since the electrostatic fields have to compensate the flow through the electrodes. Relating this result to the measurements of the ion temperature presented in section 5.3.2.2 shows that the flow through the ion funnel needs to be reduced to assure a softer ion transfer instead of increasing the voltage.

The reduction of the length of the ion funnel resulting in a reduced pumping area causes similar effects, as shown in appendix A.5. Ions are dragged out of the ion funnel at the inlet of the ion funnel. Here, the space between the inlet nozzle and the first electrodes is 5 mm. Due to the relative high back pressure a sizeable part of the gas leaves the ion funnel through this gap.

5.3.2.1 Transmission parameters

Measurements have been carried out to determine the ion transmission of the 5 hPa ion funnel. The experiment is conducted with a 25 cm stainless steel capillary (inner diameter 0.5 mm). The capillary is positioned at the entrance

of the ion funnel. Upstream the capillary is the counter electrode of the DBD, which is driven at constant pressure of 1300 hPa and a flow of 1.0 slm nitrogen. The total ion count should remain constant with increased pressure at the outlet because the output of the ion source is limited by the constant chocked flow in the capillary (cf. chapter 4.3.2).

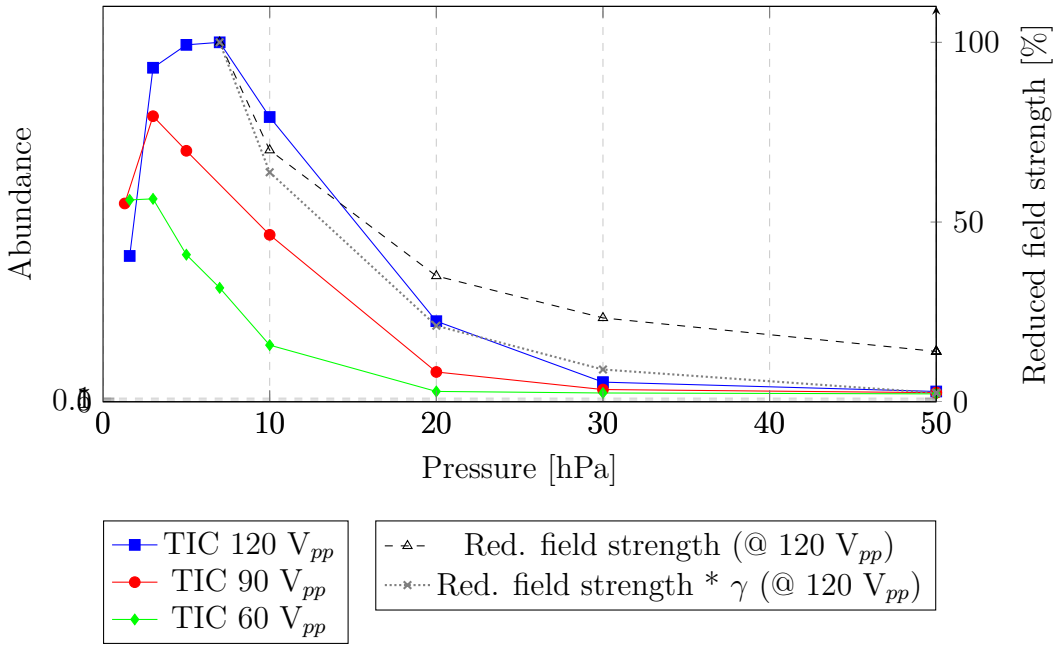

Figure 5.15: Total ion count measured at different pressures and voltage amplitudes (at 1.8 MHz) applied to the funnel. The second vertical axis shows the reduced field strength.

The transmission of the ion funnel decreases when the pressure reaches a critical level above approximately 10 hPa at 120 V_{pp}, depending on the used voltage amplitude. This can be explained by the reduced field strength E/N, which is the ratio of the electrostatic field E and the molecule density N. The unit for the reduced field strength is Townsend ($1\,\mathrm{Td} = 10^{-17}\,\mathrm{V\,cm^2}$). Figure 5.15 shows that the total ion count follows the reduced field strength. At higher pressure the measured total ion count decreases more pronounced than E/N. This is rationalized by the changing optimum ion funnel frequency, while the experiment is carried out at constant frequency (cf. chapter 5.1.2). Multiplying the reduced field strength with γ results in a curve that matches well the measured ion transmission. γ represents the dependency of the funnel

frequency on the efficiency of the RF-field, as discuss in chapter 5.1.2.

At a voltage amplitude of 120 V_{pp} the ion funnel operates with maximum efficiency up to 7 hPa. The transmission reduces when the fluid dynamic forces are becoming stronger than the electrostatic forces between the electrodes.

Table 5.2 shows that the reduced field strength at the point of the maximum transmission through the ion funnel reduces with increasing pressure. However, the high Townsend values presented in the table are only reached directly in-between the electrodes. Ions reaching the mass analyzer will not enter this region and thus experience much lower field strength as shown by the low rate of fragmentation present in the measurements presented in this chapter.

Pressure [hPa]	Voltage amplitude [V_{pp}]	Reduced field strength [Td]	Relative ion current [a.u.]
1.6	60	3000	0.55
3	90	2500	0.80
5	120	2000	1.00

Table 5.2: Reduced field strength for the maximum transmission at different ion funnel voltage amplitudes at 1.8 MHz.

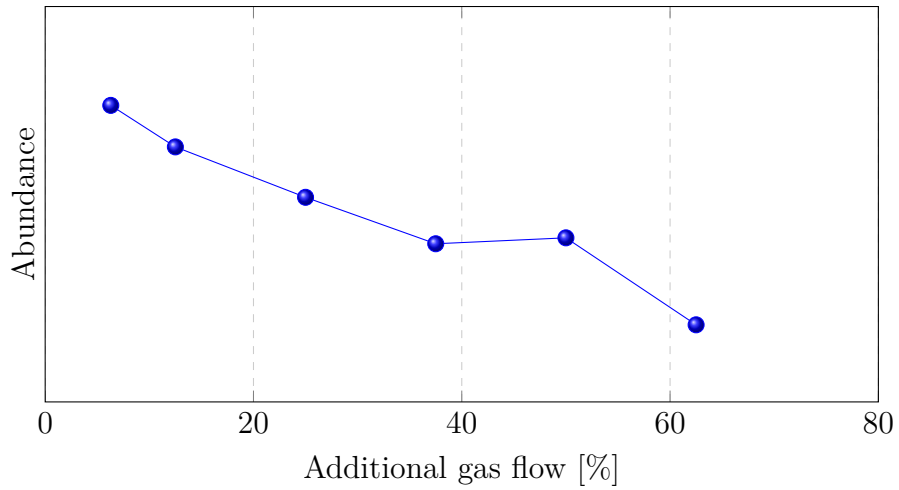

Figure 5.16: Total ion count measured with an additional gas flow added concentrically to the constant flow of the DBD (1 slm).

The ion transmission increases with pressures up to an optimum (cf. figure 5.15). This is in contrast to the reduced field strength presented in table 5.2

and is explained by the reduced velocity in the ion funnel. In figure 5.16 a measurement with an additional gas flow is shown. The ion funnel is driven with 120 V_{pp} at 10 hPa. The pressure is kept constant while an additional flow of nitrogen is added concentrically to the capillary. The flow through the DBD was 1 slm. All other parameters were kept constant. Figure 5.16 shows that an increased flow of 60 % can decrease the ion transmission by approximately 20 %. The fluid dynamic simulation has shown that the velocity in the ion funnel is already high without additional flow. Increasing the flow renders the efficiency of the funnel less favorably.

5.3.2.2 Ion energies

To study the conditions in the ion funnel at 5 hPa, experiments with different ion chemistry are made. Higher ion temperatures enable more reactions with higher activation thresholds and can lead to more product ions. The toluene fragmentation as well as the fragmentation of water clusters with toluene as dopant are studied. In figure 5.17 the total ion count is shown as function of the voltage amplitude applied to the ion funnel. The total ion count shows a maximum at approximately 90 V_{pp}.

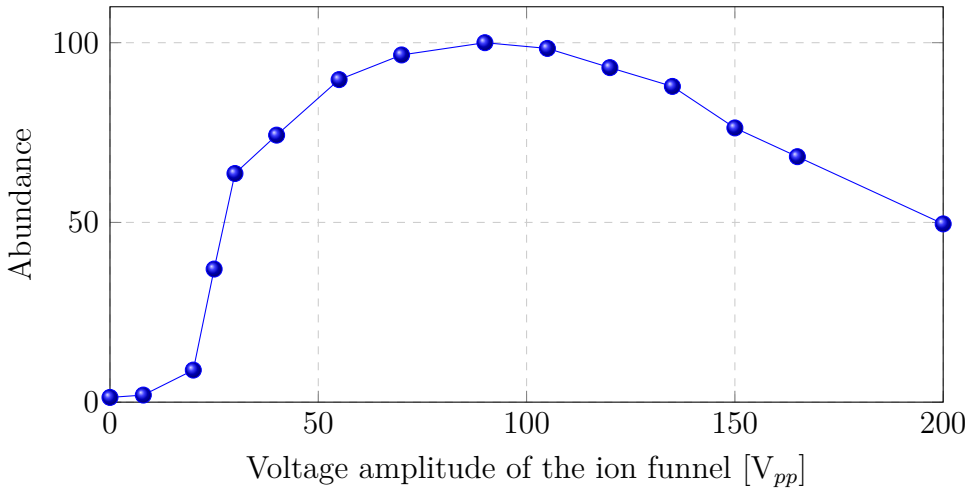

Figure 5.17: Total ion count measured at different voltage amplitudes applied to the funnel at 1.8 MHz.

Figure 5.18 shows the distribution of the most intense ion signals. All signals are scaled to the total ion count. Toluene is added with a mixing ratio of

150 ppmv in nitrogen. Without scaling the toluene peak (m/z 92) shows the most intense peak at 70 V_{pp}. Dissociative proton attachment to toluene (m/z = 91) starts at 90 V_{pp} and leads to the most intense peak at 120 V_{pp}. The dissociative proton attachment starts at a collision energy of about 2.3 eV for toluene [46, 117]. Finally smaller fragments start to form at 120 V_{pp}. A rearrangement of the toluene ring and the loss of C_2H_2 forms a fragment at mass 65. Further on an additional loss of C_2H_2 forms a fragment at mass 39 by an additional loss of C_2H_2 [119, 9]. Another fragmentation pathway seems to form a C_2H_5 fragment (m/z 29).

At low voltage amplitudes ($\lesssim$ 20 V_{pp}) a fraction of the toluene dimer ions with a stability of 0.66 eV survives [30]. Additional energy is needed to produce the smaller fragments from the toluene ion, e.g. $C_5H_5^+$ (m/z = 65, 7.3 eV) or $C_3H_3^+$ (m/z = 39, 9.1 eV) [119].

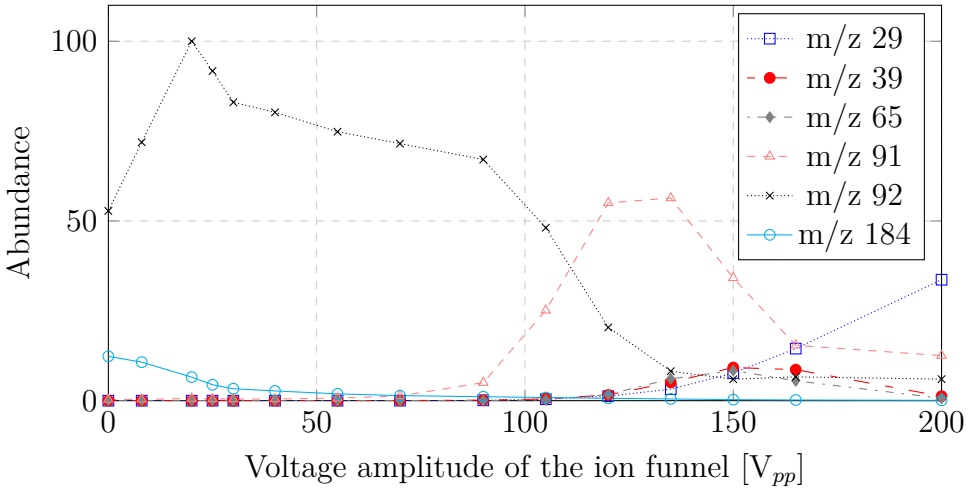

Figure 5.18: Abundance for different masses scaled by the total ion count measured at different voltage amplitudes (@ 1.8 MHz) applied to the funnel.

Figure 5.19 shows the distribution of the most intense ion peaks scaled to the total ion count when water is added at a mixing ratio of 0.3 %vol to the 150 ppmv toluene mixture. The water consumes toluene (m/z 92) and thus only a weak toluene signal remains. Toluene is protonated with the water present (m/z 93). The protonation starts at 20 V_{pp} and exhibits a maximum at 90 V_{pp}. The dissociative proton attachment of toluene seems to happen in the same voltage amplitude range as before. Water clusters with 4 and 5 water molecules (m/z 73 and 91) show a maximum at voltage amplitudes of 20 V_{pp}.

The water cluster with 3 water molecules (m/z 55) has a shallow maximum at 55 V_{pp}. Smaller water clusters show no clear maximum over the measured voltage amplitude range of up to 210 V_{pp}. The stability of the water clusters is listed in table 5.3.

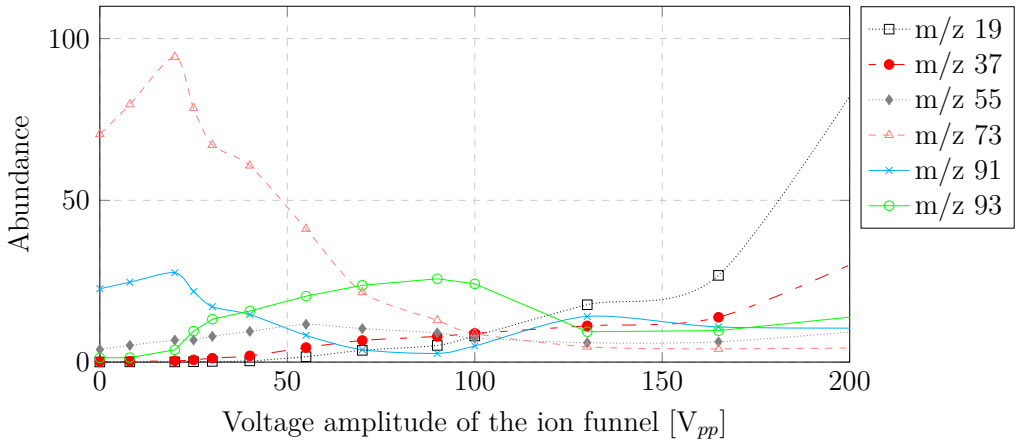

Figure 5.19: Abundance for different masses scaled by the total ion count measured at different voltage amplitudes (@ 1.8 MHz) applied to the funnel, water is added at a mixing ratio of 0.3 %vol.

The measurements show that a dramatic shift of the water cluster distribution along with protonation reactions can not be avoided within the range of good transmission through the ion funnel. A relatively soft transfer is still given at a voltage amplitude of 70 V_{pp}. At this operation point the dissociative proton attachment and fragmentation of toluene is not yet efficient. Regarding the low stabilities listed in table 5.3 water clusters should not be present (only m/z 19) above about 45 V_{pp}. However, at this level ion temperatures above 1000 K are reached. Since higher water clusters are observed at $U_{pp} > 45$ V, extensive recombination reactions further downstream must be present. At mixing ratios of 0.3 %vol this seems to be rather feasible.

5.3.3 Characteristics of the segmented quadrupole

The segmented quadrupole enables application of an axial DC gradient, which drives the ions through the quadrupole. However, experiments have shown that an additional DC gradient does not increase the ion current. DC gradients up to 4 V cm^{-1} do not change the total ion count, while higher DC gradients decrease

m/z	Stability [eV]
19	1.1
37	0.6
55	0.4
73	0.3
91	0.2
109	0.1

Table 5.3: Stability of the water clusters estimated for 295 K by the equilibrium constants measured by Lau et al [76] and Kebarle et al [59].

the total ion count. It is concluded that the gas stream of the expansion is sufficient to drive the ions through the quadrupole. Higher DC gradients probably defocus the ions trapped in the axial quadrupole field and lead to the observed decrease in the TIC.

The quadrupole is far below the high pressure limit. Even at high voltage amplitudes (600 V_{pp}) the low mass limit is m/z ≤ 5 (cf. equation 5.3). The high mass limit is m/z ≥ 150 at 2×10^{-2} hPa, so for higher masses the length of the quadrupole is too short for sufficient ion cooling, if the ions enter with a speed of 350 m s^{-1}. This may changed by increasing the pressure in the quadrupole or by reducing the initial velocity of the ions.

5.3.3.1 Ion energies

Measurements have shown that the toluene ion stays intact in the quadrupole. This might be caused by the low pressure in the quadrupole which results in single collisions in this stage. No toluene fragmentation or dissociative proton attachment is observed even at voltage amplitudes up to 800 V_{pp}. Figure 5.20 shows the total ion count of a measurement similar to the one described in section 5.3.2.2. Again water is added at mixing ratios of 0.3 %vol to the 150 ppmv toluene/nitrogen mixture.

Figure 5.21 shows that no significant changes at m/z 93 (toluene+H) and 91 (toluene-H) are present with increasing voltage amplitudes. Mass 91 is not due to $[H + (H_2O)_5]^+$ water cluster because the concentration of the cluster with one water less (m/z 73) is low and the collision cross section of the larger

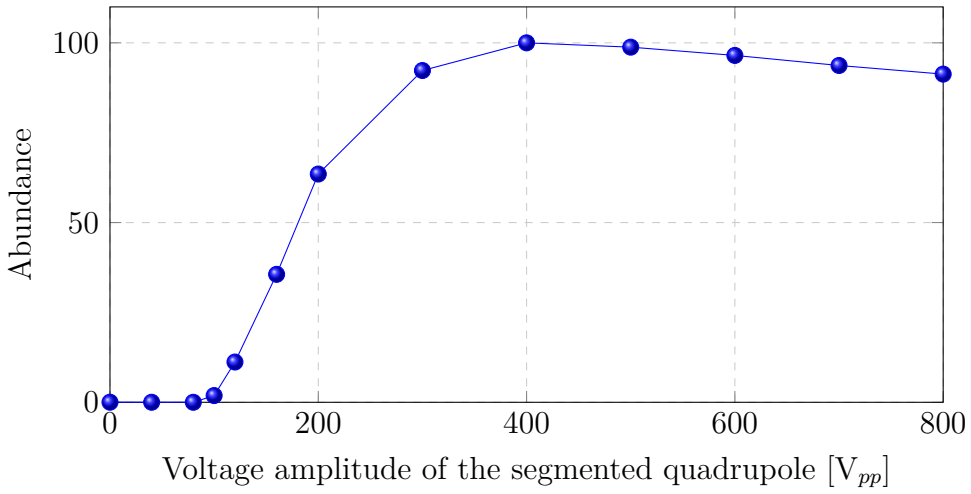

Figure 5.20: Total ion count measured at different voltage amplitudes applied to the segmented quadrupole (@ 4.6 MHz) using a toluene/water mixture.

cluster is higher. It is clearly visible that the water cluster system is efficiently shifted to small n, since the main product ion clusters are H_3O^+ (m/z 19) and $(H_2O)H_3O^+$ (m/z 37). The quadrupole should thus be operated at the voltage amplitude of maximum transmission around 400 V_{pp}.

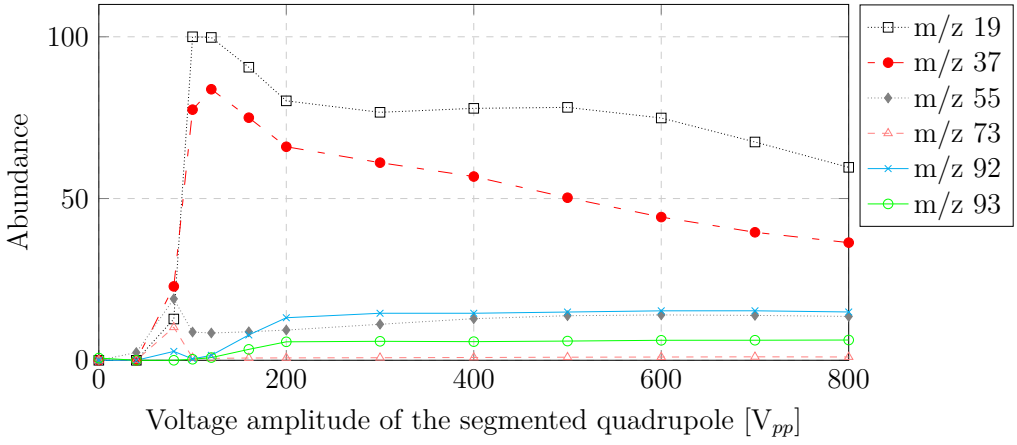

Figure 5.21: Ion count for different masses scaled by the total ion count measured at different voltage amplitudes (@ 4.6 MHz) applied to the segmented quadrupole.

5.3.4 Space-charge limit of the transfer elements

Transfer element	Voltage amplitude [V_{pp}]	Charge [$C\,m^{-1}$]	Ion current [µA]
Ion funnel 100 hPa	300	2×10^{-7}	73
Ion funnel 5 hPa	120	4×10^{-8}	15
Segmented Quadrupole	400	6×10^{-9}	2

Table 5.4: Calculation of the maximum transferred charge and ion currents through the transfer elements.

Table 5.4 lists the maximum ion currents that can be transferred through each transfer element at typical voltage amplitudes, which is limited by space-charge. For this estimation it is assumed, that the ions travel at the speed of sound, approximately $350\,m\,s^{-1}$. The calculation is done using equation 5.10 for the ion funnel and equation 5.4 for the quadrupole. The corresponding ion current is reached under ideal conditions only. Because a number of parameters play a significant role, e.g. the nozzle properties downstream of the transfer element and the corresponding fluid dynamics.

The calculation demonstrates that the ion funnels can transfer much more current than the quadrupole. If ion funnel transmissions close to 1 are reached, the quadrupole will be the limiting transfer element.

5.3.5 Transmission of the transfer elements

All transmission measurements are performed with grounded nozzles and the transfer elements driven in the rf-only mode. These measurements include several parameters that change the performance of the transmission such as fluid dynamic, electrostatic, space-charge, and surface effects, respectively as well as nozzle diameters and more. A discussion of the impact of these parameters is thus very challenging.

The transmission has been calculated using the ion currents measured upstream of the ion funnel and downstream of the nozzle of the ion funnel by means of a Faraday cup and a custom electrometer. This measurement has been performed with the 5 hPa and the 100 hPa ion funnel. The ion current of

the DBD has been measured using a mass flow of 700 sccm. For this experiment the DBD has been driven with an electrode distance of 1 mm, 13.5 kV, and 26 kHz, which yields an optimum ion output.

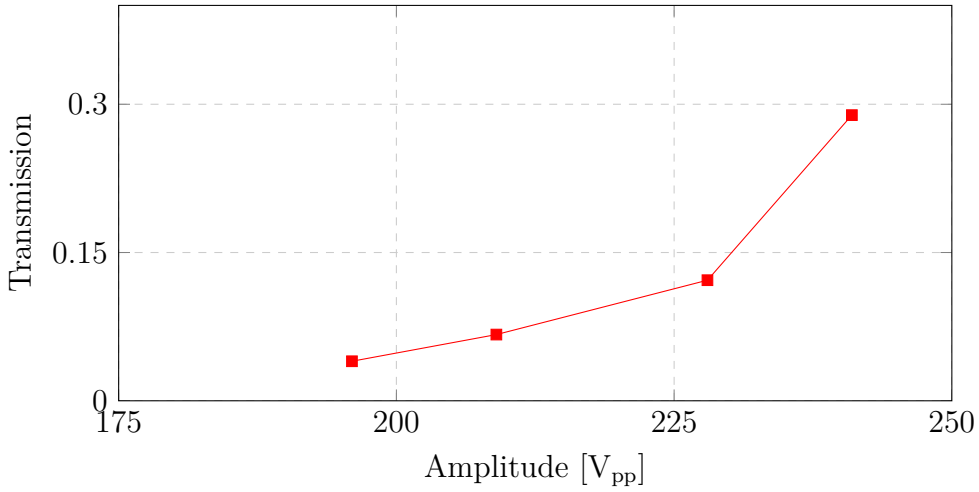

Figure 5.22: Transmission of the 100 hPa ion funnel measured at different voltage amplitudes (@ 10 MHz) using nitrogen for the DBD ion source.

The ion transmission of the 100 hPa ion funnel has been measured in the presents of nitrogen in the DBD ion source. As shown in figure 5.22, a transmission of 29 % has been reached, which is in good agreement with the simulation presented in section 5.3.1. The voltage amplitude was limited to 240 V_{pp} because the driving circuit is a prototype. Applying a higher voltage amplitudes leads to higher transmissions. The limitation is caused by a mismatch of the driving circuit and the ion funnel, which causes an increased power consumption.

Red. field strength [Td]	Voltage Amplitude 100 hPa, 0.25 mm [V_{pp}]	Voltage Amplitude 5 hPa, 0.5 mm [V_{pp}]
323	200	20
404	250	25
484	300	30

Table 5.5: Voltage amplitudes of the 5 hPa and the 100 hPa ion funnel for a given reduced field strength.

The transferred ions are collimated by collisions; a measure for the energy of the collisions is the reduced field strength. Figure 5.5 shows the reduced field strength reached in the ion funnels at a given voltage amplitude. The reduced field strength is a factor of 10 lower in the 100 hPa ion funnel compared to the 5 hPa ion funnel. It follows that the collision energy induced in the 5 hPa ion funnel using 30 V_{pp} is comparable to the collision energy induced in the 100 hPa ion funnel using 300 V_{pp}. So the transfer through the 100 hPa ion funnel is comparably soft. Here, a 300 V_{pp} voltage amplitude should lead to the sift of the water cluster system, and protonation, e.g. of toluene, but no dissociative proton attachment ($[T\text{-}H]^+$ (m/z 91)) should be possible, which needs 2.3 eV, as discussed in section 5.3.2.2.

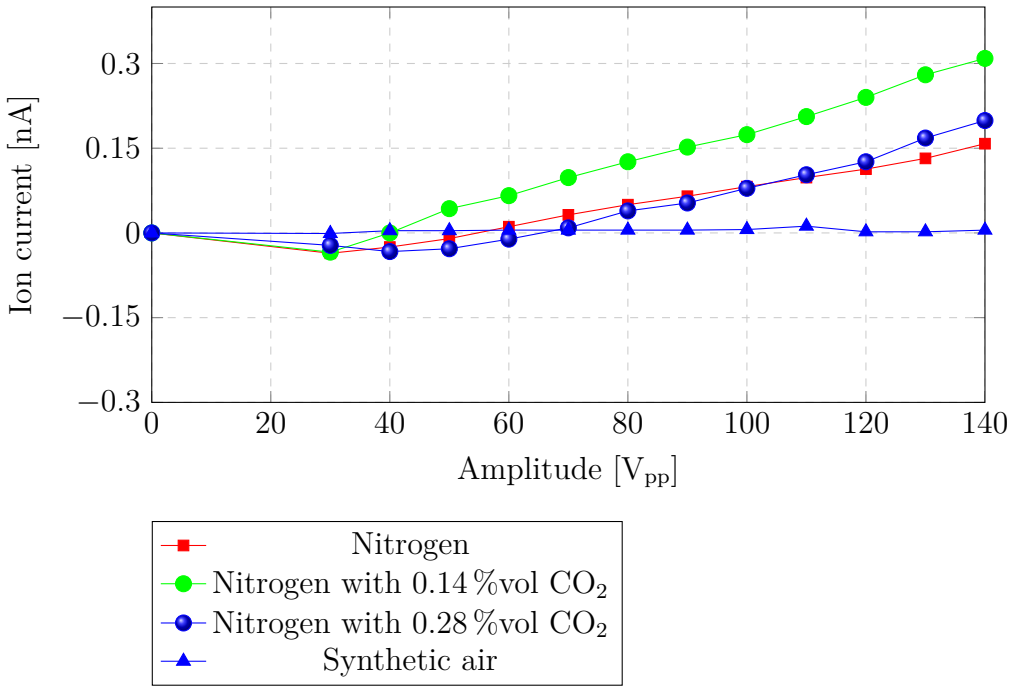

Figure 5.23: Transmission of the 5 hPa ion funnel measured at different voltage amplitudes (@ 1.8 MHz) using different gases in the DBD ion source.

Different gases have been used to measure the transmission of the 5 hPa ion funnel because the equilibrium of negative and positive charges changes using different gases in the DBD but no significant differences in transmission have been observed. Positioning the Faraday cup downstream of the ion funnel (behind the nozzle), the transmission curves shown in figure 5.23 have been measured. Accordingly the resulting transmission is given in table 5.6. This

Gas	Ion current (DBD) [nA]	Transmission (140 V_{pp}) [%]
synthetic air	0.007	71
nitrogen	0.478	33
nitrogen with 0.14 %vol CO_2	0.378	82
nitrogen with 0.28 %vol CO_2	0.354	56

Table 5.6: Transmission of the 5 hPa ion funnel operated at 120 V_{pp} and 1.8 MHz measured using different gas mixtures. Additionally the measured ion current of the DBD upstream the ion funnel is given.

agrees well with the SIMION simulations presented in chapter 5.3.2 and shows a high transmission is possible at a voltage amplitude of 120 V_{pp}. The flow into the ion funnel should be further reduced to reach a transmission of 1 with lower voltage amplitudes leading to a somewhat softer transfer.

For the measurement of the quadrupole transmission the Faraday cup has been placed behind the nozzle downstream of the segmented quadrupole with the ion funnel driven at a fixed voltage amplitude of 120 V_{pp}. The result is related to the ion current measured behind the ion funnel and resulting transmissions are plotted in figure 5.24. An ion transmission as high as 50 % is reached. The ion current limiting element is the exit nozzle of the quadrupole; as discussed in section 5 the ion beam has a diameter, which is too large.

As shown in table 5.7 a transfer stage with three transfer elements should be feasible. Further improvements of the transfer parameters are possible but nevertheless compared to a transfer stage without transfer elements signal improvements by two orders of magnitude are gained by the 5 hPa ion funnel and three orders of magnitude are gained by the segmented quadrupole.

An measurement error is mainly caused by variations of the ion source, which is approximately 50 %. The electrometer operated in the course of measurements with good stability, as discussed in section 4.3.2.1. The ion mass is a further parameter affecting the transmission, which is a topic for forthcoming measurements. In nitrogen (purity 99.999 %) mainly smaller gas phase ions are present, e.g. H_2O; the transmission for each species differs.

In this work a transmission of 50 % has been reached through a standard ion

funnel driven at a pressure of 5 hPa; similar transmission efficiencies have been reported by Kim et al. [67]. They reported a transmission of 60 % through a single ion funnel. Using the current configuration of the transfer stage a total ion transmission of 5 % is feasible. Increasing the voltage amplitude of the 100 hPa ion funnel and decreasing the flow through the 5 hPa ion funnel a total ion transmission above 10 % through three transfer elements appear to be realistic.

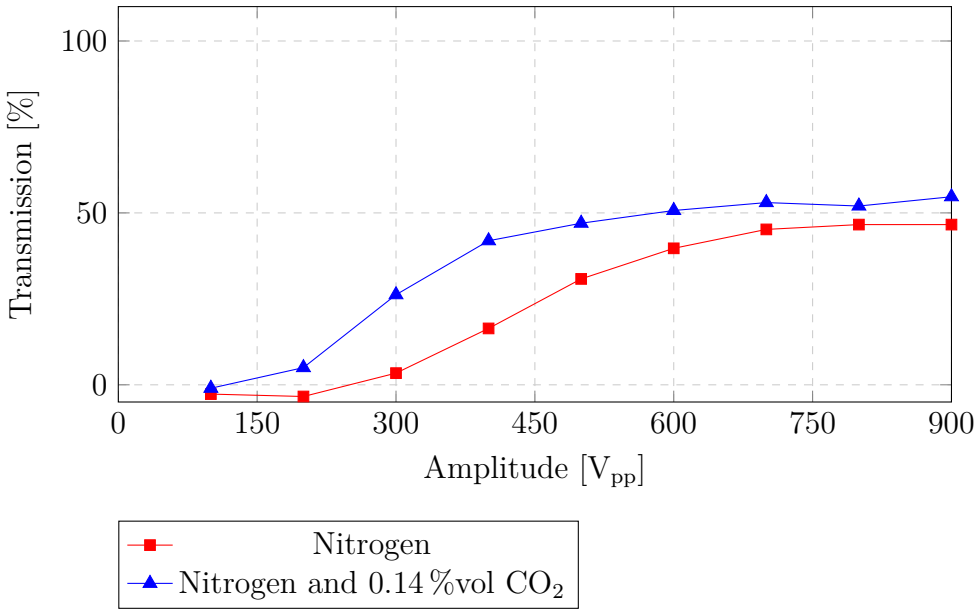

Figure 5.24: Transmission of the segmented quadrupole measured at different voltage amplitudes (@ 4.6 MHz) using different gases in the DBD ion source.

Stage	0	1	2	TOF
Gas flow in [sccm]	2000 - 10000	410	81	0.07
Downstream nozzle diameter [mm]	0.5	1	1	-
Pressure [hPa]	100	5	8×10^{-3}	7×10^{-7}
Measured ion transmission	>0.2	0.5	0.5	-

Table 5.7: Parameters of a possible transfer stage with three pressure reduction stages using the characterized transfer elements.

5.3.6 Limits of the ion funnel

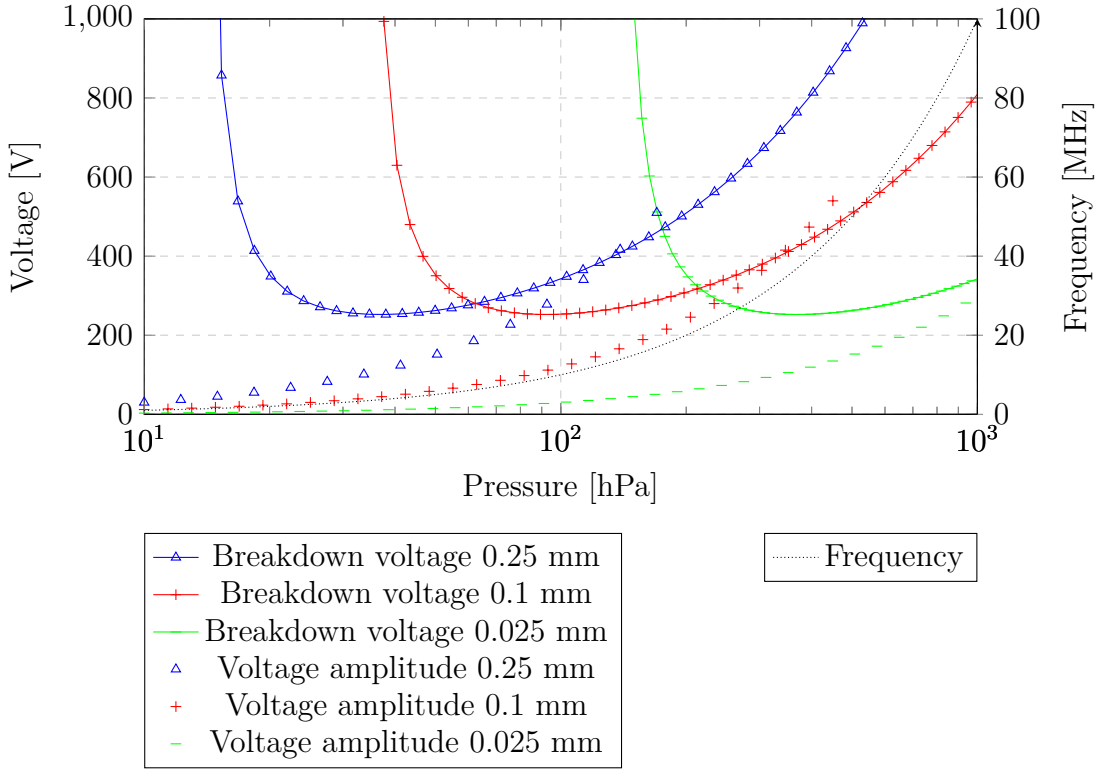

Figure 5.25: Limits of operation for an ion funnel. The experimental results are scaled to a wider pressure range using the equations discussed in section 5.1.2. Additionally the breakdown voltages for given electrode distances are plotted.

In figure 5.25, the simulation results for the 100 hPa ion funnel (using 300 V_{pp} at 10 MHz with a transmission of 50 % at m/z = 100) are scaled to other pressures and electrode distances, respectively. The following assumptions are made for the scaling: The flow velocity is constant; this means that the mass flow increases with increasing pressure. The frequency has been scaled up linearly with the pressure (keeping $\gamma = 0.6$, c.f. equation 5.8), to keep the damping of the electrostatic field by diffusion constant; Thus the efficiency of the RF-field is reduced but also the power consumption is reduced, which is a crucial parameter.

The breakdown voltages for nitrogen are calculated using the equations of Burm [14]. Comparing the breakdown voltage and the required voltage amplitude shows that the constructed 100 hPa ion funnel is operating at its

limit with an electrode distance of 0.25 mm. If the electrode distance is reduced to approximately 25 µm, the operation at AP may be possible. This is hardly realized with an standard ion funnel but the design of the planar ion funnel could enable even an operation at atmospheric pressure.

Chapter 6

Conclusions and Outlook

In this work two newly designed mass spectrometric ion transfer stages and a brilliant dielectric barrier discharge (DBD) ion source have been developed, assembled and characterized.

For atmospheric as well as may other research fields reliable measurements of ultra-trace species are crucial. In this regard chemical ionization mass spectrometry provides a highly sensitive tool. Most mass spectrometers deployed for these measurements operate with multiple quadrupole mass analyzers, which cannot provide fast measurements, if a broad range of masses is to be recorded. This is particularly true for airborne instruments where fast measurements are much better suited for in-situ measurements since time of flight instruments can monitor a wide mass range with fast measurement cycles. However, more efficient transfer stages are required for TOF instruments for optimum performance because the analyzer needs lower background pressures to work properly as compared to quadrupole analyzers. Without further measures this results in higher losses in the transfer stage and reduced sensitivity. High transmission can be achieved using ion funnels, which work optimal for ion focusing at pressures above 1 hPa [125]. Ion funnels feature a relatively small distance between the electrodes, so a high effective potential is generated. Therefore ion funnels operate very efficiently at relatively high pressure compared to multi poles. In this work a transfer stage with four transfer elements using two ion funnels, one at 100 hPa and one at 5 hPa, has been developed, assembled and characterized. Optimization of the ion funnels with respect to ion transmission was achieved by a combination of fluid mechanical and electrostatic simula-

tions. It has been shown that a high transmission can be reached and critical parameters determining ion transmission as well as collision induced processes have been discussed. An ion ion funnel working efficiently at 100 hPa in a mass spectrometer was not presented before.

In addition sensitivity is gained by the use of a brilliant ion source, therefore a DBD ion source has been optimized. The plasma ion source can be operated with several gases. This enables generation of dopant ions in the plasma. The DBD replaces the logistically challenging radioactive ion source. An approach to combine the ion funnel working at 100 hPa efficiently with the ion source is presented.

This approach is a route towards in-situ measurements of a multiplicity of analytes. Further work is needed to construct a fully operational airborne instrument. However, the critical fundamental components that are required to generate primary ions and guide them into the mass analyzer with high transmission have been developed, assembled and characterized.

The second transfer stage developed addresses the thermal sampling of cluster ions, i. e. the softest possible transfer into the mass analyzer. It enables studies of collision induced processes as well as CID-free measurement of ion clusters in order to study fundamental processes occurring in chemical ionization sources. This transfer stage also offers the opportunity to closely study the processes in the expansion downstream of pressure restricting devices. Additionally reactions induced by electrostatic fields can be identified.

Several important parameters of the transfer stage can be controlled, which are not accessible with standard transfer stages but have a major impact on ion reactions. Various electric fields can be tuned in order to diagnose their influence on e.g. ion clusters generated in the source and transmitted to the mass spectrometer. The distance and the pressure between the first nozzle and the inlet capillary can be adjusted, as well as the voltages applied to each nozzle and the capillary tip. The transfer stage has been tested and characterized employing the well described proton bound water cluster system. Critical parameters for the measured cluster distribution have been identified and compared with a thermodynamic model, demonstrating that the measured cluster mass signals closely represent a thermally equilibrated cluster system. The measurements show that for reliable mass spectral data, especially for

reliable ion cluster measurements, care must be taken of the processes within and downstream the expansions. Also at lower pressure energetic collisions induced by electrostatic fields play an important role. The setup has yielded valuable data on the clustering processes in the positive ion mode [68] as well as in the negative mode [24]. In both publications important ion and ion cluster reactions in the ion source have been identified. The details of the set-up of the transfer stage have been published recently [1].

In conclusion, this transfer stage enables detailed studies of the cluster chemistry typically present in chemical ionization processes. Especially the study of ion reactions with and without electrostatic fields is promising for further studies of AP ion source reaction cascades.

6.1 Outlook

The results presented in this work may lead to the setup of a truly unique and versatile airborne CIMS instrument. This will take place over the next 1.5 years with a possible first deployment in an aircraft campaign in August 2016. First measurements within the framework of a ground-based campaign are envisioned to characterize the instrument. For an optimum airborne instrument the following improvements need to be implemented:

1. Instrument sensitivity needs to be optimized by a proper choice of TOF mass spectrometer.

2. A quantitative measurements through calibration are crucial. For the relatively sticky sulfuric acid the development of an new online calibration procedure is challenging but working units already exist [74]. Less sticky species are easier calibrated, e.g. by the use of permeation tubes. Mixing of the online calibration gas into the inlet air flow is a critical factor, which has to be carefully addressed.

3. Full automation of the instrument with proper failure strategies must be implemented to enable fail-save measurements.

4. The inlet stage of the instrument should be characterized with regard to wall loss for sticky and reactive species as well as with regard to adverse chemical reactions.

5. The thermal sampling transfer stage should be used to characterize several chemical ionization reaction cascades typically used in API mass spectrometry.

Bibliography

[1] S. Albrecht, S. Klopotowski, V. Derpmann, S. Klee, K. J. Brockmann, F. Stroh, and T. Benter. "Studies of the mechanism of the cluster formation in a thermally sampling API MS". *Review of Scientific Instruments* 85.1 (2014), p. 014102.

[2] A. D. Appelhans and D. A. Dahl. "SIMION ion optics simulations at atmospheric pressure". *International Journal of Mass Spectrometry* 244.1 (2005), pp. 1–14.

[3] E. Arijs, A. Barassin, E. Kopp, C. Amelynck, V. Catoire, H. P. Fink, C. Guimbaud, U. Jenzer, D. Labonnette, W. Luithardt, et al. "Stratospheric chemical ionization mass spectrometry: nitric acid detection by different ion molecule reaction schemes". *International Journal of Mass Spectrometry* 181.1 (1998), pp. 99–111.

[4] F. Arnold, H. Böhringer, and G. Henschen. "Composition measurements of stratospheric positive ions". *Geophysical Research Letters* 5.8 (1978), pp. 653–656.

[5] R. Asundi, G. Schulz, and P. Chantry. "Studies of N_4^+ and N_3^+ Ion Formation in Nitrogen Using High-Pressure Mass Spectrometry". *The Journal of Chemical Physics* 47.5 (1967), pp. 1584–1591.

[6] I. Barnes, H. Kersten, W. Wissdorf, T. Pohler, H. Honen, S. Klee, K. Brockmann, and T. Benter. "Novel laminar flow ion source for LC- and GC-API MS". *Proceedings of the 58th ASMS Conference on Mass Spectrometry and Allied Topics; Salt Lake City, UT, USA* (2010).

[7] H. Berresheim, T. Elste, C. Plass-Dülmer, F. L. Eisele, and D. J. Tanner. "Chemical ionization mass spectrometer for long-term measurements of

atmospheric OH and H_2SO_4". *International Journal of Mass Spectrometry* 202.1 (2000), pp. 91–109.

[8] R. S. Blake, P. S. Monks, and A. M. Ellis. "Proton-transfer reaction mass spectrometry". *Chemical Reviews* 109.3 (2009), pp. 861–896.

[9] R. Bombach, J. Dannacher, and J. P. Stadelmann. "Energy and time dependence of the decay processes of toluene molecular cations". *Journal of the American Chemical Society* 105.13 (1983), pp. 4205–4211.

[10] L. Böswirth, S. Bschorer, and T. Buck. *Technische Strömungslehre–Lehr-und Übungsbuch. 8. überarbeitete und erweiterte Auflage*. Vieweg + Teubner Verlag / GWV Fachverlage GmbH, Wiesbaden, Germany, 2010.

[11] A. E. Bourassa, A. Robock, W. J. Randel, T. Deshler, L. A. Rieger, N. D. Lloyd, E. J. T. Llewellyn, and D. A. Degenstein. "Large volcanic aerosol load in the stratosphere linked to Asian monsoon transport". *Science* 337.6090 (2012), pp. 78–81.

[12] M. T. Bowers, ed. *Gas phase ion chemistry*. Vol. 1. Academic Press, New-York, USA, 1979.

[13] A. P. Bruins. "Mass-spectrometry with ion sources operating at atmospheric pressure". *Mass Spectrometry Reviews* 10.1 (1991), pp. 53–77.

[14] K. T. A. L. Burm. "Calculation of the Townsend Discharge Coefficients and the Paschen Curve Coefficients". *Contributions to Plasma Physics* 47.3 (2007), pp. 177–182.

[15] M. Busman, J. Sunner, and C. R. Vogel. "Space-charge-dominated mass spectrometry ion sources: Modeling and sensitivity". *Journal of the American Society for Mass Spectrometry* 2.1 (1991), pp. 1–10.

[16] V. J. Caldecourt, D. Zakett, and J. C. Tou. "An Atmospheric-Pressure Ionization Mass-Spectrometer". *International Journal of Mass Spectrometry and Ion Processes* 49.2 (1983), pp. 233–251.

[17] C. D. Cappa and M. J. Elrod. "A computational investigation of the electron affinity of CO_3 and the thermodynamic feasibility of $CO_3^-(H_2O)_n^+$ ROOH reactions". *Physical Chemistry Chemical Physics* 3.15 (2001), pp. 2986–2994.

[18] A. W. Castleman and R. G. Keesee. "Ionic Clusters". *Chemical Reviews* 86.3 (1986), pp. 589–618.

[19] I. Cermak. "Compact radio-frequency power supply for ion and particle guides and traps". *Review of Scientific Instruments* 76.6 (2005), p. 063302.

[20] L. Cheng, Z. Zhitao, Z. Xiaofeng, and Y. Yan. "A study of the aging of $\alpha - Al_2O_3$ dielectric material in DBD plasma". *Plasma Science and Technology* 8.6 (2006), p. 693.

[21] J. Curtius, B. Sierau, F. Arnold, M. Reus, J. Ström, H. A. Scheeren, and J. Lelieveld. "Measurement of aerosol sulfuric acid: 2. Pronounced layering in the free troposphere during the second Aerosol Characterization Experiment (ACE 2)". *Journal of Geophysical Research: Atmospheres* 106.D23 (2001), pp. 31975–31990.

[22] P. H. Dawson. *Quadrupole mass spectrometry and its applications*. Elsevier Amsterdam, NL, 1976.

[23] X. T. Deng and M. G. Kong. "Frequency range of stable dielectric-barrier discharges in atmospheric He and N_2". *IEEE Transactions on Plasma Science* 32.4 (2004), pp. 1709–1715.

[24] V. Derpmann, S. Albrecht, and T. Benter. "The role of ion-bound cluster formation in negative ion mass spectrometry". *Rapid Communications in Mass Spectrometry* 26.17 (2012), pp. 1923–1933.

[25] F. L. Eisele, E. R. Lovejoy, E. Kosciuch, K. F. Moore, R. L. Mauldin, J. N. Smith, P. H. McMurry, and K. Iida. "Negative atmospheric ions and their potential role in ion-induced nucleation". *Journal of Geophysical Research: Atmospheres* 111.D4 (2006), p. D04305.

[26] F. L. Eisele and D. J. Tanner. "Ion-assisted tropospheric OH measurements". *Journal of Geophysical Research* 96.D5 (1991), pp. 9295–9308.

[27] F. L. Eisele and D. J. Tanner. "Measurement of the gas phase concentration of H_2SO_4 and methane sulfonic acid and estimates of H_2SO_4 production and loss in the atmosphere". *Journal of Geophysical Research: Atmospheres* 98.D5 (1993), pp. 9001–9010.

[28] *Electrical Properties of Fused Quartz*. Momentive Performance Materials Inc. URL: `http://www.momentive.com/WorkArea/DownloadAsset.aspx?id=24700` (visited on 01/09/2014).

[29] M. J. Elrod, R. F. Meads, J. B. Lipson, J. V. Seeley, and M. J. Molina. "Temperature dependence of the rate constant for the HO_2 + BrO reaction". *The Journal of Physical Chemistry* 100.14 (1996), pp. 5808–5812.

[30] B. Ernstberger, H. Krause, and H. J. Neusser. "Metastable decay and binding energies of van der Waals cluster ions". *Zeitschrift für Physik D Atoms, Molecules and Clusters* 20.1 (1991), pp. 189–192.

[31] J. B. Fenn. "Mass spectrometric implications of high-pressure ion sources". *International Journal of Mass Spectrometry* 200.1-3 (2000), pp. 459–478.

[32] S. Foner and R. Hudson. "Mass spectrometric studies of metastable nitrogen atoms and molecules in active nitrogen". *The Journal of Chemical Physics* 37.8 (1962), pp. 1662–1667.

[33] D. Gerlich. "Inhomogeneous, RF fields: a versatile tool for the study of processes with slow ions". *Advances in Chemical Physics* 82 (1992), pp. 1–176.

[34] *GESTIS Database*. Institut für Arbeitsschutz der Deutschen Gesetzlichen Unfallversicherung. URL: `http://gestis.itrust.de` (visited on 09/06/2014).

[35] N. Gherardi, G. Gouda, E. Gat, A. Ricard, and F. Massines. "Transition from glow silent discharge to micro-discharges in nitrogen gas". *Plasma Sources Science and Technology* 9.3 (2000), pp. 340–346.

[36] K. Giles, S. D. Pringle, K. R. Worthington, D. Little, J. L. Wildgoose, and R. H. Bateman. "Applications of a travelling wave-based radio-frequency-only stacked ring ion guide". *Rapid Communications in Mass Spectrometry* 18.20 (2004), pp. 2401–2414.

[37] N. Gimelshein, S. Gimelshein, T. Lilly, and E. Moskovets. "Numerical modeling of ion transport in an ESI-MS system". *Journal of the American Society for Mass Spectrometry* 25.5 (2014), pp. 820–831.

[38] R. J. Gordon, Y. T. Lee, and D. R. Herschbach. "Supersonic molecular beams of alkali dimers". *The Journal of Chemical Physics* 54 (1971), p. 2393.

[39] S. Guan and A. G. Marshall. "Stacked-ring electrostatic ion guide". *Journal of the American Society for Mass Spectrometry* 7.1 (1996), pp. 101–106.

[40] X. Guo, A. P. Bruins, and T. R. Covey. "Characterization of typical chemical background interferences in atmospheric pressure ionization liquid chromatography-mass spectrometry". *Rapid Communications in Mass Spectrometry* 20.20 (2006), pp. 3145–3150.

[41] M. Hanke, J. Uecker, T. Reiner, and F. Arnold. "Atmospheric peroxy radicals: ROXMAS, a new mass-spectrometric methodology for speciated measurements of HO_2 and $\sum RO_2$ and first results". *International Journal of Mass Spectrometry* 213.2 (2002), pp. 91–99.

[42] M. Hanke, B. Umann, J. Uecker, F. Arnold, and H. Bunz. "Atmospheric measurements of gas-phase HNO_3 and SO_2 using chemical ionization mass spectrometry during the MINATROC field campaign 2000 on Monte Cimone". *Atmospheric Chemistry and Physics* 3.2 (2003), pp. 417–436.

[43] D. R. Hanson and A. R. Ravishankara. "Investigation of the reactive and nonreactive processes involving nitryl hypochlorite and hydrogen chloride on water and nitric acid doped ice". *The Journal of Physical Chemistry* 96.6 (1992), pp. 2682–2691.

[44] A. N. Hayhurst and N. R. Telford. "The occurrence of chemical reactions in supersonic expansions of a gas into a vacuum and its relation to mass spectrometric sampling". *Proceedings of the Royal Society of London. A. Mathematical and Physical Sciences* 322.1551 (1971), pp. 483–507.

[45] M. Hopfner, N. Glatthor, U. Grabowski, S. Kellmann, M. Kiefer, A. Linden, J. Orphal, G. Stiller, T. von Clarmann, B. Funke, and C. D. Boone. "Sulfur dioxide (SO_2) as observed by MIPAS/Envisat: temporal development and spatial distribution at 15-45 km altitude". *Atmospheric Chemistry and Physics* 13.20 (2013), pp. 10405–10423.

[46] F.-S. Huang and R. C. Dunbar. "Time-resolved photodissociation of toluene ion". *International Journal of Mass Spectrometry and Ion Processes* 109 (1991), pp. 151–170.

[47] L. G. Huey, D. R. Hanson, and C. J. Howard. "Reactions of SF_6^- and I^- with atmospheric trace gases". *The Journal of Physical Chemistry* 99.14 (1995), pp. 5001–5008.

[48] L. G. Huey, D. J. Tanner, D. L. Slusher, J. E. Dibb, R. Arimoto, G. Chen, D. Davis, M. P. Buhr, J. B. Nowak, R. L. Mauldin Iii, et al. "CIMS measurements of HNO_3 and SO_2 at the South Pole during ISCAT 2000". *Atmospheric Environment* 38.32 (2004), pp. 5411–5421.

[49] K. L. Hunter and B. J. McIntosh. "An improved model of the fringing fields of a quadrupole mass filter". *International Journal of Mass Spectrometry and Ion Processes* 87.2 (1989), pp. 157–164.

[50] G. Hurst, T. Bortner, and R. E. Glick. "Ionization and excitation of argon with alpha particles". *The Journal of Chemical Physics* 42.2 (1965), pp. 713–719.

[51] Y. Ibrahim, K. Tang, A. V. Tolmachev, A. A. Shvartsburg, and R. D. Smith. "Improving mass spectrometer sensitivity using a high-pressure electrodynamic ion funnel interface". *Journal of the American Society for Mass Spectrometry* 17.9 (2006), pp. 1299–1305.

[52] *Intergovernmental Panel on Climate Change, Fourth Assessment Report: Climate Change 2007: The AR4 Synthesis Report.* Chapter 2. Geneva: IPCC, 2007.

[53] *Intergovernmental Panel on Climate Change, Fourth Assessment Report: Climate Change 2007: The AR4 Synthesis Report*. Chapter 7.4.5. Geneva: IPCC, 2007.

[54] J. T. Jayne, U. Pöschl, Y.-m. Chen, D. Dai, L. T. Molina, D. R. Worsnop, C. E. Kolb, and M. J. Molina. "Pressure and temperature dependence of the gas-phase reaction of SO_3 with H_2O and the heterogeneous reaction of SO_3 with H_2O/H_2SO_4 surfaces". *The Journal of Physical Chemistry A* 101.51 (1997), pp. 10000–10011.

[55] N. R. Jensen, D. R. Hanson, and C. J. Howard. "Temperature Dependence of the Gas Phase Reactions of CF_3O with CH_4 and NO". *The Journal of Physical Chemistry* 98.34 (1994), pp. 8574–8579.

[56] W. P. Jesse and J. Sadauskis. "Ionization in pure gases and the average energy to make an ion pair for alpha and beta particles". *Physical Review* 97.6 (1955), pp. 1668–1670.

[57] C. E. Junge, C. W. Chagnon, and J. E. Manson. "Stratospheric aerosols". *Journal of Meteorology* 18.1 (1961), pp. 81–108.

[58] H. Kambara and I. Kanomata. "Collision-induced dissociation of water cluster ions at high pressure". *International Journal of Mass Spectrometry and Ion Physics* 25.2 (1977), pp. 129–136.

[59] P. Kebarle, S. K. Searles, A. Zolla, J. Scarboro, and M. Arshadi. "Solvation of hydrogen ion by water molecules in gas phase heats and entropies of solvation of individual reactions - $H^+(H_2O)_{n-1} + H_2O \rightarrow H^+(H_2O)_n$". *Journal of the American Chemical Society* 89.25 (1967), pp. 6393–6399.

[60] A. Kellerbauer, T. Kim, R. B. Moore, and P. Varfalvy. "Buffer gas cooling of ion beams". *Nuclear Instruments and Methods in Physics Research Section A: Accelerators, Spectrometers, Detectors and Associated Equipment* 469.2 (2001), pp. 276–285.

[61] R. T. Kelly, A. V. Tolmachev, J. S. Page, K. Tang, and R. D. Smith. "The ion funnel: theory, implementations, and applications". *Mass Spectrometry Reviews* 29.2 (2010), pp. 294–312.

[62] H. Kersten. "Development of an Atmospheric Pressure Ionization source for in situ monitoring of degradation products of atmospherically relevant volatile organic compounds". PhD thesis. University of Wuppertal, Germany, 2011.

[63] H. Kersten, V. Derpmann, I. Barnes, K. Brockmann, R. O'Brien, and T. Benter. "A novel APPI-MS setup for in situ degradation product studies of atmospherically relevant compounds: capillary atmospheric pressure photo ionization (cAPPI)". *Journal of the American Society for Mass Spectrometry* 22 (11 2011), pp. 2070–2081.

[64] J. Kestin and W. Leidenfrost. "An absolute determination of the viscosity of eleven gases over a range of pressures". *Physica* 25.7 (1959), pp. 1033–1062.

[65] S. Kim, L. G. Huey, R. E. Stickel, D. J. Tanner, J. H. Crawford, J. R. Olson, G. Chen, W. H. Brune, X. Ren, R. Lesher, et al. "Measurement of HO_2NO_2 in the free troposphere during the intercontinental chemical transport experiment–North America 2004". *Journal of Geophysical Research: Atmospheres* 112.D12 (2007), D12S01.

[66] T. Kim, A. V. Tolmachev, R. Harkewicz, D. C. Prior, G. Anderson, H. R. Udseth, R. D. Smith, T. H. Bailey, S. Rakov, and J. H. Futrell. "Design and implementation of a new electrodynamic ion funnel". *Analytical Chemistry* 72.10 (2000), pp. 2247–2255.

[67] T. Kim, H. R. Udseth, and R. D. Smith. "Improved ion transmission from atmospheric pressure to high vacuum using a multicapillary inlet and electrodynamic ion funnel interface". *Analytical Chemistry* 72.20 (2000), pp. 5014–5019.

[68] S. Klee, S. Albrecht, V. Derpmann, H. Kersten, and T. Benter. "Generation of ion bound solvent clusters as reactant ions in dopant assisted APPI and APLI". *Analytical and Bioanalytical Chemistry* 405.22 (2013), pp. 6933–6951.

[69] D. Kley, J. M. R. III, and C. Phillips, eds. *SPARC Report No2: Upper Tropospheric and Stratospheric Water Vapour*. 2000.

[70] S. Klopotowski, Y. Brachthaeuser, D. Mueller, H. Kersten, W. Wissdorf, K. J. Brockmann, and T. Benter. "Characterization of API-MS inlet capillary flow: Examination of transfer times and choked flow conditions". *Proceedings of the 60th ASMS Conference on Mass Spectrometry and Allied Topics, Vancouver, BC, Canada* (2012).

[71] S. Klopotowski, Y. Brachthaeuser, D. Mueller, H. Kersten, W. Wissdorf, V. Derpmann, K. J. Brockmann, U. Janoske, and T. Benter. "API-MS transfer capillary flow: Examination of the downstream gas expansion". *Proceedings of the 59th ASMS Conference on Mass Spectrometry and Allied Topics, Denver, CO, USA* (2011).

[72] U. Kogelschatz, B. Eliasson, W. Egli, et al. "From ozone generators to flat television screens: history and future potential of dielectric-barrier discharges". *Pure and Applied Chemistry* 71.10 (1999), pp. 1819–1828.

[73] K. Kozlov, H. Wagner, R. Brandenburg, and P. Michel. "Spatio-temporally resolved spectroscopic diagnostics of the barrier discharge in air at atmospheric pressure". *Journal of Physics D: Applied Physics* 34.21 (2001), pp. 3164–3176.

[74] A. Kuerten, L. Rondo, S. Ehrhart, and J. Curtius. "Calibration of a chemical ionization mass spectrometer for the measurement of gaseous sulfuric acid". *Journal of Physical Chemistry A* 116.24 (2012), 6375–6386.

[75] E. E. Kunhardt. "Generation of large-volume, atmospheric-pressure, nonequilibrium plasmas". *IEEE Transactions on Plasma Science* 28.1 (2000), pp. 189–200.

[76] Y. K. Lau, S. Ikuta, and P. Kebarle. "Thermodynamics and kinetics of the gas-phase reactions - $H_3O^+(H_2O)_{n-1} + H_2O = H_3O^+(H_2O)_n$". *Journal of the American Chemical Society* 104.6 (1982), pp. 1462–1469.

[77] H. M. Lee, M. B. Chang, and K. Y. Wu. "Abatement of sulfur hexafluoride emissions from the semiconductor manufacturing process by atmospheric-pressure plasmas". *Journal of the Air & Waste Management Association* 54.8 (2004), pp. 960–970.

[78] M. Li, C. Li, H. Zhan, J. Xu, and X. Wang. "Effect of surface charge trapping on dielectric barrier discharge". *Applied Physics Letters* 92.3 (2008), p. 031503.

[79] S. Li and E. R. Bernstein. "Toluene-water clusters: Ion fragmentation and chemistry". *The Journal of Chemical Physics* 97.2 (1992), pp. 792–803.

[80] J. Liao, H. Sihler, L. G. Huey, J. A. Neuman, D. J. Tanner, U. Friess, U. Platt, F. M. Flocke, J. J. Orlando, P. B. Shepson, et al. "A comparison of Arctic BrO measurements by chemical ionization mass spectrometry and long path-differential optical absorption spectroscopy". *Journal of Geophysical Research: Atmospheres* 116.D1 (2011), D00R02.

[81] J. Liao, L. G. Huey, E. Scheuer, J. E. Dibb, R. E. Stickel, D. J. Tanner, J. A. Neuman, J. B. Nowak, S. Choi, Y. Wang, et al. "Characterization of soluble bromide measurements and a case study of BrO observations during ARCTAS". *Atmospheric Chemistry and Physics* 12.3 (2012), pp. 1327–1338.

[82] D. Lide. *CRC Handbook of Chemistry and Physics 75 th Ed.* Boca Raton, London, GB, 1995.

[83] B. Lin and J. Sunner. "Ion transport by viscous gas flow through capillaries". *Journal of the American Society for Mass Spectrometry* 5.10 (1994), pp. 873–885.

[84] H. Lindner, H. Bauer, and C. Lehmann. *Taschenbuch der Elektrotechnik und Elektronik*. Hanser Fachbuchverlag, Leipzig, Germany, 2004.

[85] E. R. Lovejoy, D. R. Hanson, and L. G. Huey. "Kinetics and products of the gas-phase reaction of SO3 with water". *The Journal of Physical Chemistry* 100.51 (1996), pp. 19911–19916.

[86] G. Markovich, R. Giniger, M. Levin, and O. Cheshnovsky. "Photoelectron spectroscopy of iodine anion solvated in water clusters". *The Journal of Chemical Physics* 95.12 (1991), pp. 9416–9419.

[87] J. Marti and K. Mauersberger. "A survey and new measurements of ice vapor pressure at temperatures between 170 and 250 K". *Geophysical Research Letters* 20.5 (1993), pp. 363–366.

[88] F. Massines, N. Gherardi, N. Naude, and P. Segur. "Glow and Townsend dielectric barrier discharge in various atmosphere". *Plasma Physics and Controlled Fusion* 47.12B (2005), B577.

[89] F. Massines, P. Segur, N. Gherardi, C. Khamphan, and A. Ricard. "Physics and chemistry in a glow dielectric barrier discharge at atmospheric pressure: diagnostics and modelling". *Surface and Coatings Technology* 174 (2003), pp. 8–14.

[90] R. L. Mauldin, G. J. Frost, G. Chen, D. J. Tanner, A. S. H. Prevot, D. D. Davis, and F. L. Eisele. "OH measurements during the First Aerosol Characterization Experiment (ACE 1): Observations and model comparisons". *Journal of Geophysical Research: Atmospheres* 103.D13 (1998), pp. 16713–16729.

[91] R. L. Mauldin, D. J. Tanner, and F. L. Eisele. "A new chemical ionization mass spectrometer technique for the fast measurement of gas phase nitric acid in the atmosphere". *Journal of Geophysical Research: Atmospheres* 103.D3 (1998), pp. 3361–3367.

[92] R. L. Mauldin, D. J. Tanner, J. A. Heath, B. J. Huebert, and F. L. Eisele. "Observations of H_2SO_4 and MSA during PEM-Tropics-A". *Journal of Geophysical Research: Atmospheres* 104.D5 (1999), pp. 5801–5816.

[93] J. M. Meek and J. D. Craggs. *Electrical breakdown of gases*. John Wiley and Sons, Ltd., New York, USA, 1978.

[94] A. Meiners, M. Leck, and B. Abel. "Efficiency enhancement of a dielectric barrier plasma discharge by dielectric barrier optimization". *Review of Scientific Instruments* 81.11 (2010), p. 113507.

[95] F. R. Menter. "Two-equation eddy-viscosity turbulence models for engineering applications". *AIAA Journal* 32.8 (1994), pp. 1598–1605.

[96] A. Michalke. "Beitrag zur Rohrströmung kompressibler Fluide mit Reibung und Wärmeübergang". *Ingenieur-Archiv* 57.5 (1987), pp. 377–392.

[97] P. E. Miller and M. B. Denton. "The transmission properties of an RF-only quadrupole mass filter". *International Journal of Mass Spectrometry and Ion Processes* 72.3 (1986), pp. 223–238.

[98] M. Miyazaki, A. Fujii, T. Ebata, and N. Mikami. "Infrared spectroscopy of hydrated benzene cluster cations,$[C_6H_6\text{-}(H_2O)_n]^+$(n= 1–6): Structural changes upon photoionization and proton transfer reactions". *Physical Chemistry Chemical Physics* 5.6 (2003), pp. 1137–1148.

[99] O. Möhler, T. Reiner, and F. Arnold. "A novel aircraft-based tandem mass spectrometer for atmospheric ion and trace gas measurements". *Review of Scientific Instruments* 64.5 (1993), pp. 1199–1207.

[100] D. M. Murphy and D. W. Fahey. "Mathematical treatment of the wall loss of a trace species in denuder and catalytic converter tubes". *Analytical Chemistry* 59.23 (1987), pp. 2753–2759.

[101] J. A. Neuman, J. B. Nowak, L. G. Huey, J. B. Burkholder, J. E. Dibb, J. S. Holloway, J. Liao, J. Peischl, J. M. Roberts, T. B. Ryerson, E. Scheuer, H. Stark, R. E. Stickel, D. J. Tanner, and A. Weinheimer. "Bromine measurements in ozone depleted air over the Arctic Ocean". *Atmospheric Chemistry and Physics* 10.14 (2010), pp. 6503–6514.

[102] J. B. Neumayr, P. G. Thirolf, D. Habs, S. Heinz, V. S. Kolhinen, M. Sewtz, and J. Szerypo. "Performance of the MLL-IonCatcher". *Review of Scientific Instruments* 77.6 (2006), p. 065109.

[103] A. M. P. Nicholas, R. J. Boyd, and D. R. Arnold. "Thermochemical parameters for organic radicals and radical ions. Part 2. The protonation of hydrocarbon radicals in the gas phase". *Canadian Journal of Chemistry* 60.24 (1982), pp. 3011–3018.

[104] J. S. Page, R. T. Kelly, K. Tang, and R. D. Smith. "Ionization and transmission efficiency in an electrospray ionization–mass spectrometry interface". *Journal of the American Society for Mass Spectrometry* 18.9 (2007), pp. 1582–1590.

[105] J. D. Payzant and P. Kebarle. "Kinetics of reactions leading to $O_2^-(H_2O)_N$ in moist oxygen". *Journal of Chemical Physics* 56.7 (1972), pp. 3482–3487.

[106] V. V. Pervukhin. "Effect of additives in a carrier gas on the behavior of ions in an ion-mobility increment spectrometer". *Journal of Analytical Chemistry* 63.12 (2008), pp. 1182–1190.

[107] W. Pfeiffer. "High-frequency voltage stress of insulation. Methods of testing". *IEEE Transactions on Electrical Insulation* 26.2 (1991), pp. 239–246.

[108] I. Radu, R. Bartnikas, G. Czeremuszkin, and M. R. Wertheimer. "Diagnostics of dielectric barrier discharges in noble gases: atmospheric pressure glow and pseudoglow discharges and spatio-temporal patterns". *IEEE Transactions on Plasma Science* 31.3 (2003), pp. 411–421.

[109] T. Reiner and F. Arnold. "Laboratory investigations of gaseous sulfuric acid formation via $SO_3 + H_2O + M \rightarrow H_2SO_4 + M$: Measurement of the rate constant and product identification". *The Journal of Chemical Physics* 101 (1994), pp. 7399–7407.

[110] A. Robock, A. Marquardt, B. Kravitz, and G. Stenchikov. "Benefits, risks, and costs of stratospheric geoengineering". *Geophysical Research Letters* 36.19 (2009), p. L19703.

[111] L. Ruby. "Applications of the Mathieu equation". *American Journal of Physics* 64.1 (1996), pp. 39–44.

[112] D. Salcedo, P. W. Villalta, V. Varutbangkul, J. C. Wormhoudt, R. C. Miake-Lye, D. R. Worsnop, J. O. Ballenthin, W. F. Thorn, A. A. Viggiano, T. M. Miller, et al. "Effect of relative humidity on the detection of sulfur dioxide and sulfuric acid using a chemical ionization mass spectrometer". *International Journal of Mass Spectrometry* 231.1 (2004), pp. 17–30.

[113] R. W. Saunders, S. Dhomse, W. S. Tian, M. P. Chipperfield, and J. M. C. Plane. "Interactions of meteoric smoke particles with sulphuric acid in the Earth's stratosphere". *Atmospheric Chemistry and Physics* 12.10 (2012), pp. 4387–4398.

[114] A. A. Scaife, T. Spangehl, D. R. Fereday, U. Cubasch, U. Langematz, H. Akiyoshi, S. Bekki, P. Braesicke, N. Butchart, M. P. Chipperfield, A. Gettelman, S. C. Hardiman, M. Michou, E. Rozanov, and T. G. Shepherd. "Climate change projections and stratosphere-troposphere interaction". *Climate Dynamics* 38.9-10 (2012), pp. 2089–2097.

[115] S. Schmidt, M. F. Appel, R. M. Garnica, R. N. Schindler, and T. Benter. "Atmospheric pressure laser ionization. An analytical technique for highly selective detection of ultralow concentrations in the gas phase". *Analytical Chemistry* 71.17 (1999), pp. 3721–3729.

[116] J. Schneider, V. Bürger, and F. Arnold. "Methyl cyanide and hydrogen cyanide measurements in the lower stratosphere: Implications for methyl cyanide sources and sinks". *Journal of Geophysical Research: Atmospheres* 102.D21 (1997), pp. 25501–25506.

[117] D. Schröder, H. Schwarz, P. Milko, and J. Roithová. "Dissociation routes of protonated toluene probed by infrared spectroscopy in the gas phase". *The Journal of Physical Chemistry A* 110.27 (2006), pp. 8346–8353.

[118] D. L. Schweickart, J. C. Horwath, L. L. Hatfield, H. Krompholz, and L. C. Walko. "The relevancy of environmental parameter space for electrical insulation design in aerospace vehicles". *Conference Record of the Twenty-Sixth International Power Modulator Symposium and High-Voltage Workshop, Piscataway, USA*. IEEE. 2004, pp. 30–33.

[119] M. Schwell, F. Dulieu, C. Gée, H.-W. Jochims, J.-L. Chotin, H. Baumgärtel, and S. Leach. "Photoionization mass spectrometry of six isomers of C_7H_8 in the 7–22 eV photon energy range". *Chemical Physics* 260.1 (2000), pp. 261–279.

[120] *Scientific Assessment of Ozone Depletion: 2010, Global Ozone Research and Monitoring Project-Report No. 52*. WMO (World Meteorological Organization), Geneva, Switzerland, 2011.

[121] G. Scoles, ed. Vol. 1. Atomic and molecular beam methods. Oxford University Press, New-York, USA, 1988.

[122] J. Q. Searcy and J. B. Fenn. "Clustering of water on hydrated protons in a supersonic free jet expansion". *The Journal of Chemical Physics* 61.12 (1974), pp. 5282–5288.

[123] J. V. Seeley, R. A. Morris, and A. A. Viggiano. "Rate constants for the reactions of $CO_3^-(H_2O)$ n= 0–5+ SO_2: Implications for CIMS detection of SO_2". *Geophysical Research Letters* 24.11 (1997), pp. 1379–1382.

[124] J. H. Seinfeld and S. N. Pandis. *Atmospheric chemistry and physics: from air pollution to climate change*. John Wiley & Sons, Hoboken, USA, 2006.

[125] S. A. Shaffer, A. Tolmachev, D. C. Prior, G. A. Anderson, H. R. Udseth, and R. D. Smith. "Characterization of an improved electrodynamic ion funnel interface for electrospray ionization mass spectrometry". *Analytical Chemistry* 71.15 (1999), pp. 2957–2964.

[126] M. W. Siegel and W. L. Fite. "Terminal ions in weak atmospheric-pressure plasmas - applications of atmospheric-pressure ionization to trace impurity analysis in gases". *Journal of Physical Chemistry* 80.26 (1976), pp. 2871–2881.

[127] *Simion*. www.simion.com. Scientific Instrument Services Inc. 8.0. (Visited on 09/06/2014).

[128] J. D. Skalny, J. Orszagh, N. J. Mason, J. A. Rees, Y. Aranda-Gonzalvo, and T. D. Whitmore. "Mass spectrometric study of negative ions extracted from point to plane negative corona discharge in ambient air at atmospheric pressure". *International Journal of Mass Spectrometry* 272.1 (2008), pp. 12–21.

[129] D. L. Slusher. "Techniques for measuring pernitric acid, peroxyacyl nitrates, and dinitrogen pentoxide by chemical ionization mass spectrometry". PhD thesis. Georgia Institute of Technology, Atlanta, USA, 2003.

[130] D. L. Slusher, L. G. Huey, D. J. Tanner, F. M. Flocke, and J. M. Roberts. "A thermal dissociation–chemical ionization mass spectrometry (TD-CIMS) technique for the simultaneous measurement of peroxyacyl nitrates and dinitrogen pentoxide". *Journal of Geophysical Research: Atmospheres* 109.D19 (2004), p. D19315.

[131] N. J. Smith, B. Rangarajan, M. T. Lanagan, and C. G. Pantano. "Alkali-free glass as a high energy density dielectric material". *Materials Letters* 63.15 (2009), pp. 1245–1248.

[132] S. Solomon, R. W. Portmann, R. R. Garcia, W. Randel, F. Wu, R. Nagatani, J. Gleason, L. Thomason, L. R. Poole, and M. P. McCormick. "Ozone depletion at mid-latitudes: Coupling of volcanic aerosols and temperature variability to anthropogenic chlorine". *Geophysical Research Letters* 25.11 (1998), pp. 1871–1874.

[133] M. Sudakov, N. Konenkov, D. Douglas, and T. Glebova. "Excitation frequencies of ions confined in a quadrupole field with quadrupole excitation". *Journal of the American Society for Mass Spectrometry* 11.1 (2000), pp. 10–18.

[134] J. A. Syage. "Mechanism of $[M+H]^+$ formation in photoionization mass spectrometry". *Journal of the American Society for Mass Spectrometry* 15.11 (2004), pp. 1521–1533.

[135] V. L. Talrose, P. S. Vinogradov, and I. K. Larin. *On the rapidity of ion-molecule reactions*. Ed. by M. T. Bowers. p. 305. Academic Press, New York, USA, 1979.

[136] D. J. Tanner and F. L. Eisele. "Present OH measurement limits and associated uncertainties". *Journal of Geophysical Research* 100.D2 (1995), pp. 2883–2892.

[137] D. J. Tanner, A. Jefferson, and F. L. Eisele. "Selected ion chemical ionization mass spectrometric measurement of OH". *Journal of Geophysical Research* 102.D5 (1997), pp. 6415–6425.

[138] A. V. Tolmachev, I. V. Chernushevich, A. F. Dodonov, and K. G. Standing. "A collisional focusing ion guide for coupling an atmospheric pressure ion source to a mass spectrometer". *Nuclear Instruments and Methods in Physics Research Section B: Beam Interactions with Materials and Atoms* 124.1 (1997), pp. 112–119.

[139] A. V. Tolmachev, H. R. Udseth, and R. D. Smith. "Charge capacity limitations of radio frequency ion guides in their use for improved ion accumulation and trapping in mass spectrometry". *Analytical Chemistry* 72.5 (2000), pp. 970–978.

[140] A. Tolmachev, I. Chernushevich, A. Dodonov, and K. Standing. "A collisional focusing ion guide for coupling an atmospheric pressure ion source to a mass spectrometer". *Nuclear Instruments and Methods in Physics Research Section B: Beam Interactions with Materials and Atoms* 124.1 (1997), pp. 112–119.

[141] F. H. W. Van Amerom, A. Chaudhary, and T. R. Short. *Planar ion funnel*. US Patent 20,130,120,894. 2013.

[142] J. Viidanoja, T. Reiner, and F. Arnold. "Laboratory investigations of negative ion molecule reactions of formic and acetic acids: implications for atmospheric measurements by ion-molecule reaction mass spectrometry". *International Journal of Mass Spectrometry* 181.1 (1998), pp. 31–41.

[143] A. A. Vostrikov and D. Y. Dubov. "Clustering in molecular gases freely expanding into vacuum". *Journal of Experimental and Theoretical Physics* 98.2 (2004), pp. 197–206.

[144] H.-E. Wagner, R. Brandenburg, K. V. Kozlov, A. Sonnenfeld, P. Michel, and J. F. Behnke. "The barrier discharge: basic properties and applications to surface treatment". *Vacuum* 71.3 (2003), pp. 417–436.

[145] X. Wang, M. Rong, D. Liu, B. Su, D. Wang, and Y. Wu. "Structural optimization of multi-needle to plane electrodes for dielectric barrier discharge". *17th International Conference on Gas Discharges and Their Applications, Cardiff, GB*. 2008, pp. 309–312.

[146] P. Warneck. *Chemistry of the Natural Atmosphere*. Vol. 71. Academic press, San Diego, USA, 1999.

[147] R. J. Weber, K. Moore, V. Kapustin, A. Clarke, R. L. Mauldin, E. Kosciuch, C. Cantrell, F. Eisele, B. Anderson, and L. Thornhill. "Nucleation in the equatorial Pacific during PEM-Tropics B: Enhanced boundary layer H_2SO_4 with no particle production". *Journal of Geophysical Research: Atmospheres* 106.D23 (2001), pp. 32767–32776.

[148] R. J. Weber, P. H. McMurry, L. Mauldin, D. J. Tanner, F. L. Eisele, F. J. Brechtel, S. M. Kreidenweis, G. L. Kok, R. D. Schillawski, and D. Baumgardner. "A study of new particle formation and growth involving

biogenic and trace gas species measured during ACE 1". *Journal of Geophysical Research: Atmospheres* 103.D13 (1998), pp. 16385–16396.

[149] S. Wuetrich. *TOFWERK AG, Uttigenstrasse 22, 3600 Thun, Switzerland*. www.tofwerk.com. Private Communication, 2011.

[150] M. Wutz, H. Adam, and W. Walcher. *Theorie und Praxis der Vakuumtechnik*. Vol. 4. Friedr. Vieweg und Sohn, Braunschweig, Germany, 1988.

[151] Y. Zhang, B. Gu, W. Wang, D. Wang, and X. Peng. "Experimental investigation on large-area dielectric barrier discharge in atmospheric nitrogen and air assisted by the ultraviolet lamp". *Spectrochimica Acta Part A: Molecular and Biomolecular Spectroscopy* 72.3 (2009), pp. 460–464.

[152] J. Zheng, A. Khalizov, L. Wang, and R. Zhang. "Atmospheric pressure-ion drift chemical ionization mass spectrometry for detection of trace gas species". *Analytical Chemistry* 82.17 (2010), pp. 7302–7308.

[153] D. R. Zook and E. P. Grimsrud. "Measurement of ion clustering equilibria of proton hydrates by atmospheric pressure ionization mass spectrometry". *Journal of Physical Chemistry* 92.22 (1988), pp. 6374–6379.

Appendix A

Details of the HS1 and SDS simulations

A.1 Boundary conditions of the fluid dynamic simulations

100 hPa ion funnel

- Reference pressure 100 hPa
- Fluid air (ideal gas) at 100 hPa and 25 °C
- Inlet pressure 200 hPa
- Mass flow (inlet) 5 slm
- Outlet (nozzle) 5 hPa
- Outlet (pump) 90 hPa
- Solver settings:
  - Heat transfer set to total energy
  - Turbulence set to Shear Stress Transport (SST) model
  - High speed wall heat transfer model
  - Advection scheme blend 0.7

  - Turbulence numerics high resolution
  - Solver double precision

5 hPa ion funnel

- Reference pressure 5 hPa
- Fluid air (ideal gas) at 5 hPa and 25 °C
- Inlet pressure 100 hPa
- Mass flow (inlet) 2 slm
- Outlet (nozzle) 0 hPa
- Outlet (pump) 5 hPa
- Solver settings:
  - Heat transfer set to total energy
  - Turbulence set to SST model
  - High speed wall heat transfer model
  - Advection scheme blend 0.7
  - Turbulence numerics high resolution
  - Solver double precision

A.2 100 hPa ion funnel

Electrostatic simulation using the Simion with the SDS collision model have been made to understand the ion movement in the ion funnel at 100 hPa.

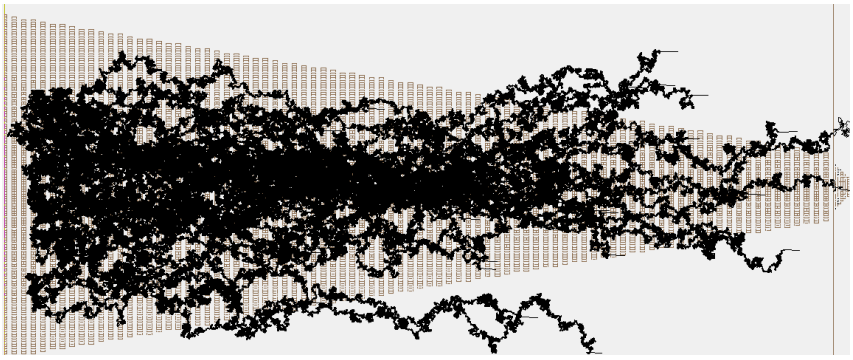

Figure A.1: A cut through the Simion SDS ion trajectory simulations of the ion funnel at 100 hPa driven with 200 V_{pp} and 10 MHz. In black the ion trajectories of 40 ions with mass 100 u are shown.

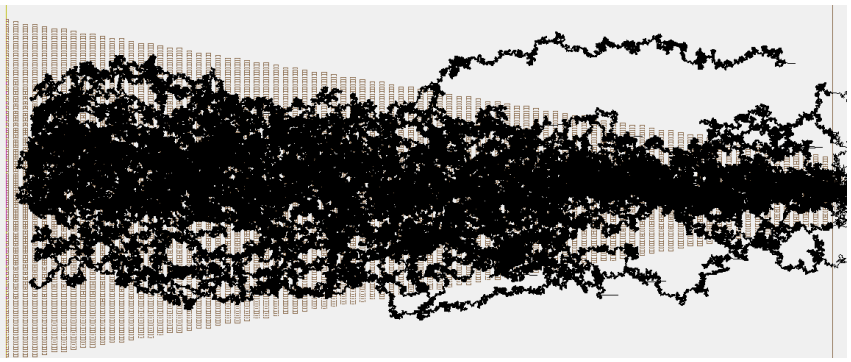

Figure A.2: As figure A.1 but for 300 V_{pp}.

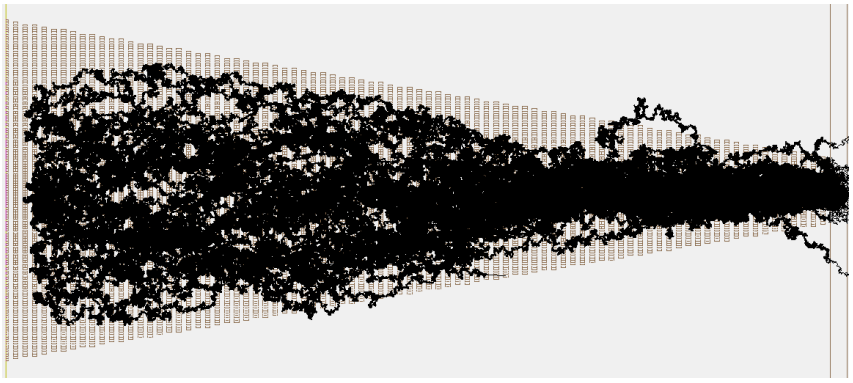

Figure A.3: As figure A.1 but for 400 V_{pp}.

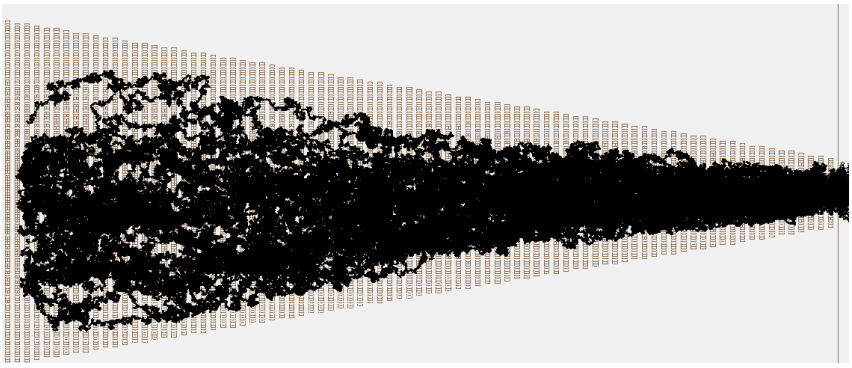

Figure A.4: As figure A.1 but for 500 V_{pp}.

A.3 5 hPa ion funnel

Electrostatic simulation using SIMION with the HS1 collision model have been made to understand the ion movement in the ion funnel at 5 hPa.

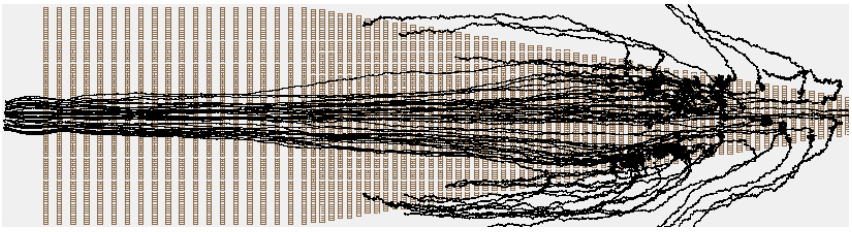

Figure A.5: A cut through the SIMION HS1 ion trajectory simulations of the ion funnel at 5 hPa driven with 60 V_{pp} and 1.8 MHz. In black the ion trajectories of 40 ions with mass 100 are shown. The velocity vector is multiplied by 0.5.

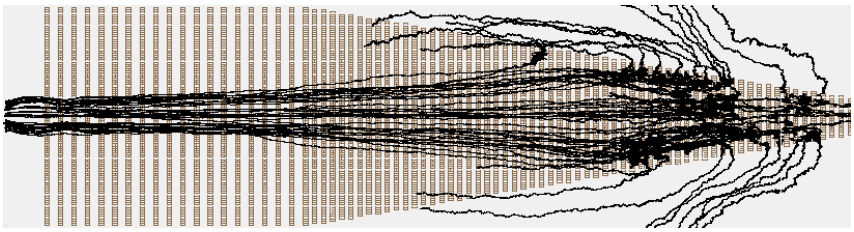

Figure A.6: Same as figure A.5 but for 120 V_{pp}.

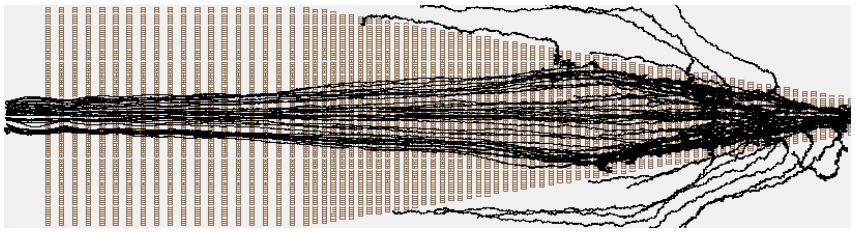

Figure A.7: Same as figure A.5 but for 180 V_{pp}.

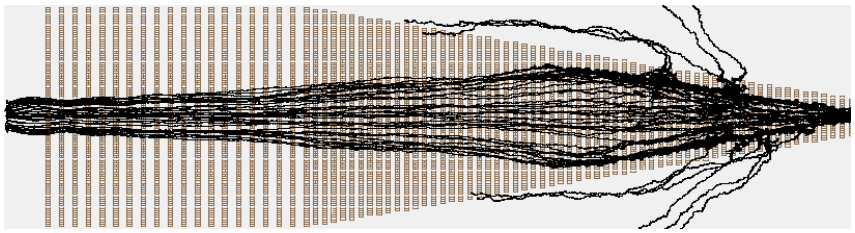

Figure A.8: Same as figure A.5 but for 240 V_{pp}.

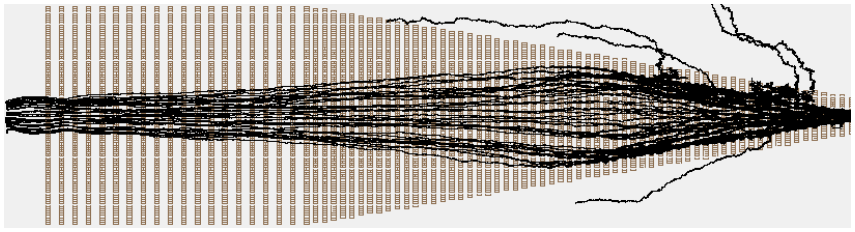

Figure A.9: Same as figure A.5 but for 300 V_{pp}.

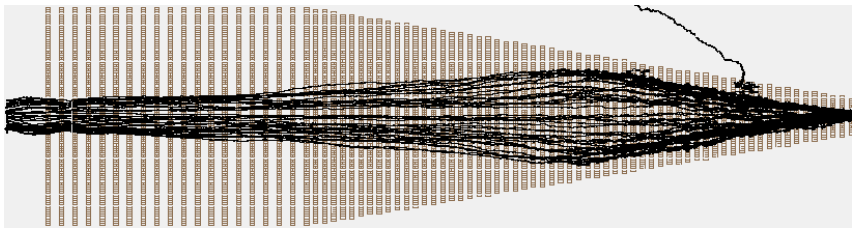

Figure A.10: Same as figure A.5 but for 360 V_{pp}.

A.4 5 hPa ion funnel with reduced velocity

Figures A.11, A.12 and A.13 show the simulated ion trajectories for the ion funnel but with reduced velocities compared to the simulations presented in section A.3.

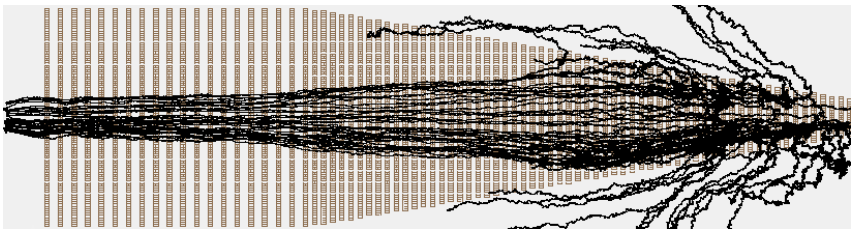

Figure A.11: A cut through the Simion HS1 ion trajectory simulations of the ion funnel at 5 hPa driven with 60 V_{pp} and 1.8 MHz. In black the ion trajectories of 40 ions with mass 100 are shown. The velocity vector is multiplied by 0.5.

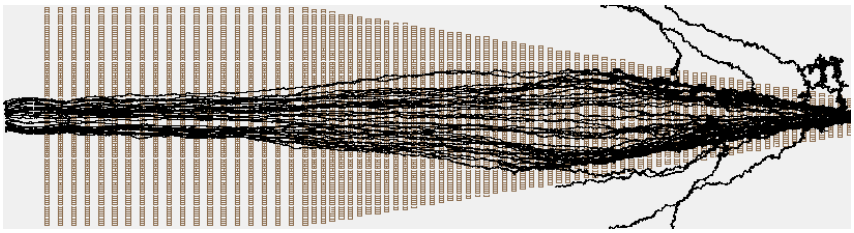

Figure A.12: Same as figure A.11 but for 120 V_{pp}.

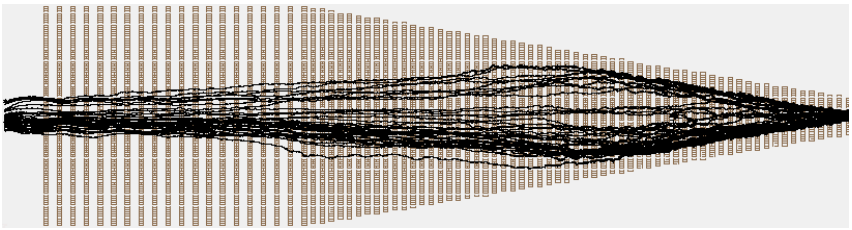

Figure A.13: Same as figure A.11 but for 180 V_{pp}.

A.5 Short 5 hPa ion funnel

Figures A.14, A.15 and A.16 show the simulated ion trajectories for a shorter version of the ion funnel (59.5 mm long) operated at the same boundary conditions as the ion funnel presented in section A.3. The following figures A.17, A.18 and A.19 show results of the underlying fluid dynamic simulations.

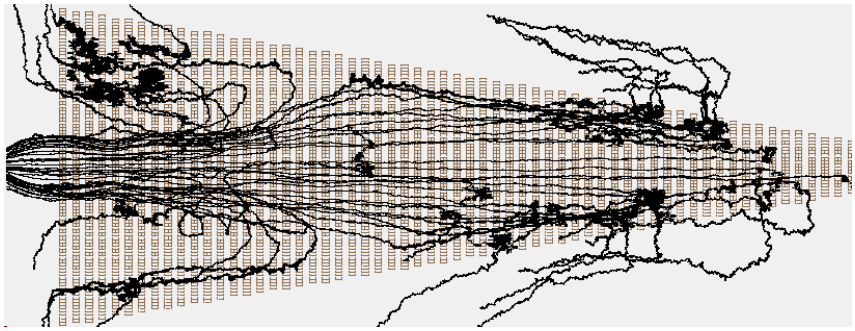

Figure A.14: A cut through the Simion HS1 ion trajectory simulations of the short ion funnel at 5 hPa driven with 120 V_{pp} and 1.8 MHz. In black the ion trajectories of 40 ions with mass 100 are shown.

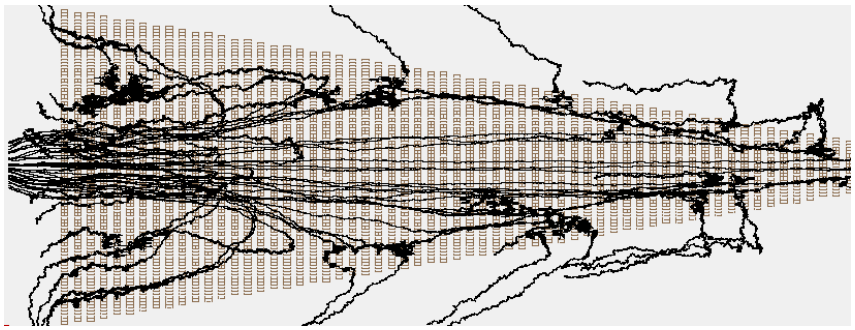

Figure A.15: Same as figure A.14 but for 180 V_{pp}.

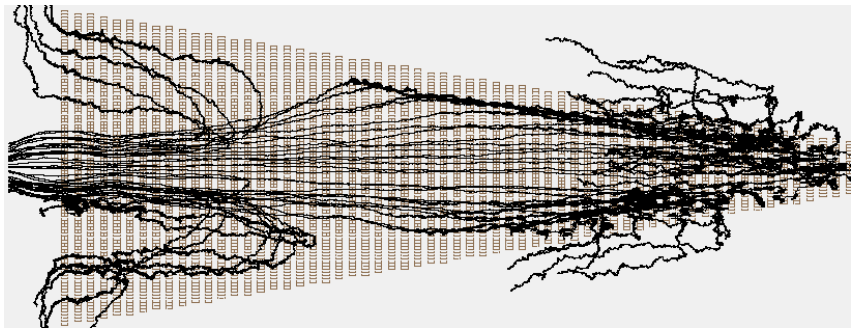

Figure A.16: Same as figure A.14 but for 240 V_{pp}.

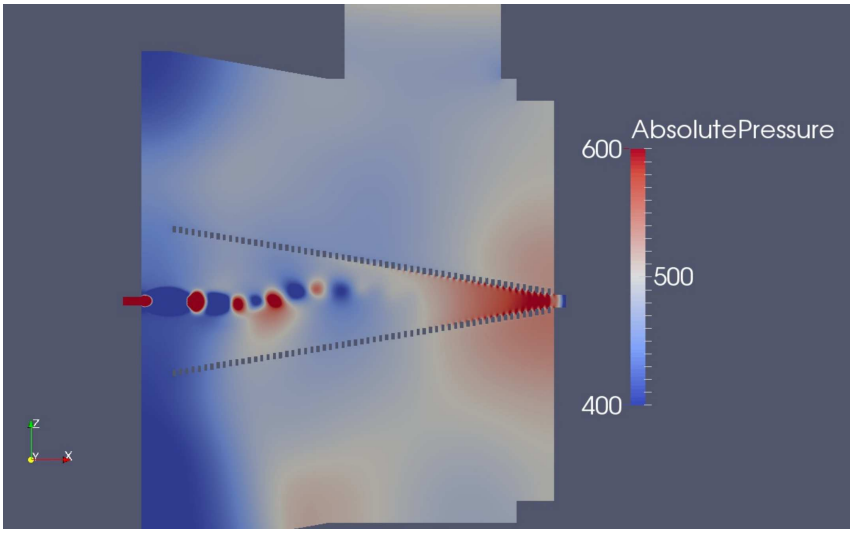

Figure A.17: A cut through the fluid dynamic simulation of a shorter ion funnel at 5 hPa with the pressure in Pa.

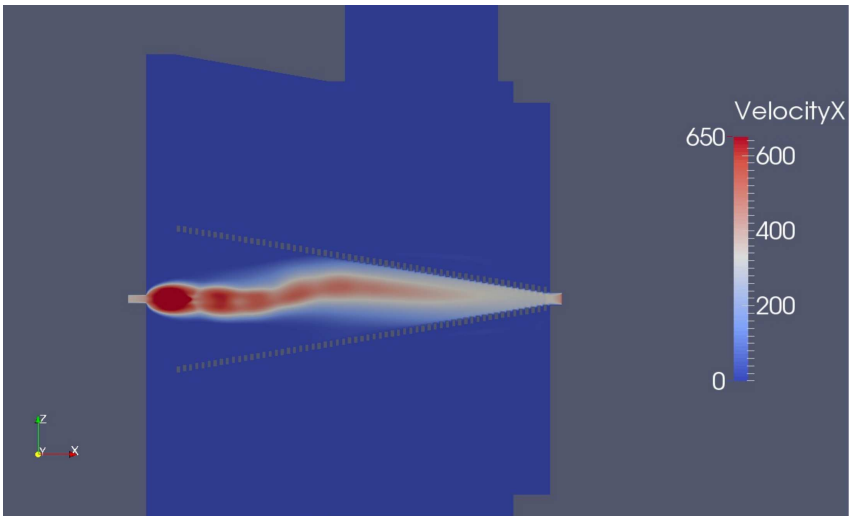

Figure A.18: Same as figure A.17 but for the velocity in x-direction in $\mathrm{m\,s^{-1}}$.

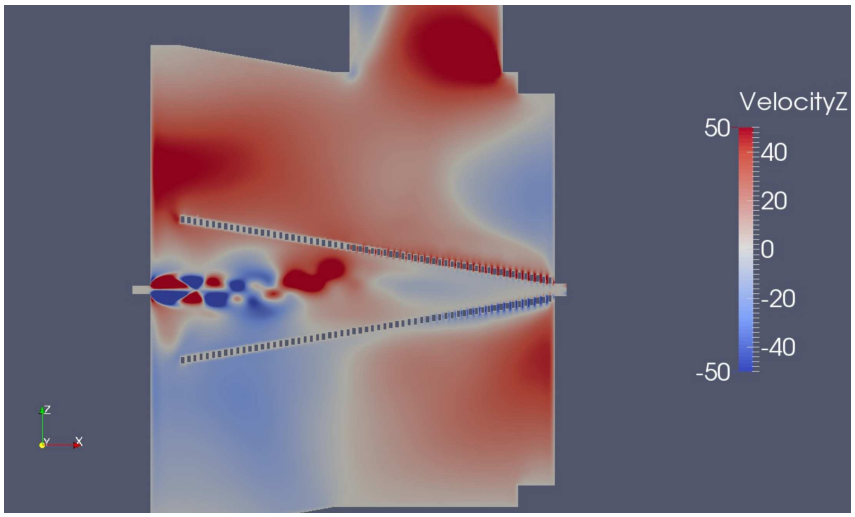

Figure A.19: Same as figure A.17 but for the velocity in z-direction in $\mathrm{m\,s^{-1}}$.

Appendix B

Python program listings

This Python code is used to fit the fluid dynamic data to the Simion mesh.

File: exportCFDSolutions.py

```
 """
This script starts the interpolation of the data.
The pickle package is used to get a binary datafile,
which can be loaded much faster than ASCI file.
The interpolated field can be chosen by the size
of the Simion field (simionPaLimits) and its scale.
The chosen field can be positioned with "shifts".
The size of the interpolated sub cubes can be
chosen with "interpolateVolume" in Simion grid units.

Authors: Walter Wissdorf, Sascha Albrecht
"""
import numpy as np
import sys

import pickle
#add package path if translation scripts are in a different
#directory from exportSDSParamFilesFromScatteredMesh import *

#run this lines to get a binary version of the data.
#It can be loaded faster than the ASCI Data.
#dat = np.loadtxt('Y-Slice0.csv', comments='"',delimiter=',')
#pickle.dump( dat, open( "CFD_daten.p", "wb" ) )
dat = pickle.load( open( "CFD_daten.p", "rb" ) )

ip={}

ip['simionPaLimits'] = np.array([[0,511],[0,357],[0,358]])
ip['shifts'] = np.array([9,178,178])
ip['scale'] = 0.00025
ip['cylindricalArray'] = 0
ip['interpolateVolume'] = 20
#in grid units f.e. insert 20 to interpolate in volumes of 20x20x20.
#if you chose a volume containing to many points you will get
#an memory error

ip['x'] = dat[:,5]
ip['y'] = dat[:,6]
ip['z'] = dat[:,7]

shift_x_mm = 99
shift_y_mm = 40
shift_z_mm = 40
```

```
ip['vx'] = dat[:,2]
ip['vy'] = dat[:,3]
ip['vz'] = dat[:,4]
ip['temp'] = dat[:,1]
ip['press'] = dat[:,0]

#------------Output for control ----------
print("Dim[m] original: ", min(ip['x']), max(ip['x']),
 min(ip['y']), max(ip['y']), min(ip['z']), max(ip['z']))
x1 = min(ip['x'])+(ip['shifts'][0])*ip['scale']
x2 = min(ip['x'])+(ip['shifts'][0]+ip['simionPaLimits'][0,1])*ip['scale']
y1 = min(ip['y'])+(ip['shifts'][1])*ip['scale']
y2 = min(ip['y'])+(ip['shifts'][1]+ip['simionPaLimits'][1,1])*ip['scale']
z1 = min(ip['z'])+(ip['shifts'][2])*ip['scale']
z2 = min(ip['z'])+(ip['shifts'][2]+ip['simionPaLimits'][2,1])*ip['scale']
print("Interpolate area [m] (original): ", x1, x2, y1, y2, z1, z2)
ip['x'] = (shift_x_mm/1000)+ip['x']
ip['y'] = (shift_y_mm/1000)+ip['y']
ip['z'] = (shift_z_mm/1000)+ip['z']
print("Dim[m] shifted: ", min(ip['x']), max(ip['x']),
 min(ip['y']), max(ip['y']), min(ip['z']), max(ip['z']))


exportSDSParamFilesFromScatteredMesh(ip)
```

File: exportSDSParamFilesFromScatteredMesh.py

```
 # -*- coding: utf8 -*-
# Tested with Python 3.2.4, Numpy 1.7.1,
#Matplotlib 1.2.0, Scipy 0.12.0

import numpy as np
import pylab as pl
from scipy.interpolate import griddata
from writeSDSFile import *

def reduceData_col(values,col,cmin,cmax):
    """This function is used to find the data lying in an area,
    to reduce the input for the interpolation routine.
    Arguments:
    values = a struct of parameters with the vectors of scalar values
    (at the irregular point positions)
    col = the index of the vector of parameters that should be reduced
    cmin, cmax = the minimum and maximum of the range of
        values that we are searching

    Returns:
    A list of pointers to the searched values.

    Author: Sascha Albrecht
    """
    ind=[]
    L=[]
    ind.extend(np.where((values[col]>=cmin)&(values[col]<=cmax)))
    for j in range(0,8):
        L.append(values[j][ind[0]])
    print("L: ",np.shape(L))
    return L


def interpolateData(values,xi,yi,zi,gridpoints):
    """Interpolates a scalar field on a volume (2d or 3d) from values at irregular,
    arbitrary points to the scalar values at a grid with the numpy "griddata"
    method (see the griddata documentation for details)

    Note:
    The fill value (value for positions outside ) is not zero as SDS fails with
    exactly zero values in the pressure data
```

```
Arguments:
values = a struct of parameters with the vectors of scalar values
(at the irregular point positions)
xi,yi,zi = vectors of regular point positions [m]
---
gridpoints = node positions of the grid (given as list of meshgrids)

Returns:
The interpolated scalar values

Author: Walter Wissdorf

Edited by: Sascha Albrecht

The function has been modified to cut the data grid
and the simion grid in smaller cubes to reduce the Ram-usage.
Which makes it impossible to interpolate meshes bigger than a critical size.
The interpolated sub cubes are put together after the interpolation.
"""

xLen = values['simionPaLimits'][0,1]-values['simionPaLimits'][0,0]+1
yLen = values['simionPaLimits'][1,1]-values['simionPaLimits'][1,0]+1
zLen = values['simionPaLimits'][2,1]-values['simionPaLimits'][2,0]+1
values_interp_vx = np.empty((xLen,yLen,zLen))
values_interp_vy = np.empty((xLen,yLen,zLen))
values_interp_vz = np.empty((xLen,yLen,zLen))
values_interp_temp = np.empty((xLen,yLen,zLen))
values_interp_press = np.empty((xLen,yLen,zLen))

#change to array
ii = len(values['z'])
values_2D=np.empty((8,ii))
values_2D[0,:]=values['x']
values_2D[1,:]=values['y']
values_2D[2,:]=values['z']
values_2D[3,:]=values['vx']
values_2D[4,:]=values['vy']
values_2D[5,:]=values['vz']
values_2D[6,:]=values['press']
values_2D[7,:]=values['temp']

subcubeLength = values['interpolateVolume']
area = subcubeLength*values['scale']
#the area that will be interpolated within each step

#in each loop the data are reduced in one dimension to reduce the overhead of the search
for i in range(0, (len(xi)-1), subcubeLength):
        print("xi: ", i, xi[i])
        # i, imax are the range of interpolated area in x-direction (in Simion grid units)
        imax = i + subcubeLength
        if imax >= len(xi): imax = len(xi) - 1
        # To get a good overlap for the interpolation a
        # bigger area of the irregular data has been chosen, e.g.
        # Interpolate regular data in the range of i, imax;
        # use the irregular data in the range of position(i)-0.3*subarea, position(imax)+0.3*subarea
        valuesSlice = list(reduceData_col(values_2D, 0, (xi[i]-area*0.3), (xi[i]+area*1.3)))
        for j in range(0, (len(yi)-1), subcubeLength):
                jmax = j + subcubeLength
                if jmax >= len(yi): jmax = len(yi) - 1
                valuesRow = list(reduceData_col(valuesSlice, 1, (yi[j]-area*0.3), (yi[j]+area*1.3)))
                for k in range(0, (len(zi)-1), subcubeLength):
                        kmax = k + subcubeLength
                        if kmax >= len(zi): kmax = len(zi) - 1
                        values_2D_cube = list(reduceData_col(valuesRow, 2, (zi[k]-area*0.3), (zi[k]+area*1.3)))
                            (yi[j]-area*0.3),(yi[j]+area*1.3),(zi[k]-area*0.3),(zi[k]+area*1.3)))
                        if (len(values_2D_cube[0])) < 100: print("Weniger als 100 Punkte zum interpolieren!")
                        # Interpolation of  the parameters for each subarea
                        values_interp_vx[i:imax,j:jmax,k:kmax] =
                              (interp(values_2D_cube,3,i,imax,j,jmax,k,kmax,gridpoints))
                        values_interp_vy[i:imax,j:jmax,k:kmax] =
```

```
                                    (interp(values_2D_cube,4,i,imax,j,jmax,k,kmax,gridpoints))
                                values_interp_vz[i:imax,j:jmax,k:kmax] =
                                    (interp(values_2D_cube,5,i,imax,j,jmax,k,kmax,gridpoints))
                                values_interp_press[i:imax,j:jmax,k:kmax] =
                                    (interp(values_2D_cube,6,i,imax,j,jmax,k,kmax,gridpoints))
                                values_interp_temp[i:imax,j:jmax,k:kmax] =
                                    (interp(values_2D_cube,7,i,imax,j,jmax,k,kmax,gridpoints))

    values_interp = {}
    values_interp[3] = values_interp_vx
    values_interp[4] = values_interp_vy
    values_interp[5] = values_interp_vz
    values_interp[6] = values_interp_press
    values_interp[7] = values_interp_temp
    return(values_interp)

def interp(values,v,xmin,xmax,ymin,ymax,zmin,zmax,gridpoints):
    """ A sub function, that calls the interpolation function with the needed parameters.

     Author: Sascha Albrecht
    """
    points = (values[0],values[1],values[2])
    qx = gridpoints[0]
    qy = gridpoints[1]
    qz = gridpoints[2]
    x = qx[xmin:xmax,ymin:ymax,zmin:zmax]
    y = qy[xmin:xmax,ymin:ymax,zmin:zmax]
    z = qz[xmin:xmax,ymin:ymax,zmin:zmax]
    grid = (x,y,z)
    return griddata(points, values[v], grid, method='linear',fill_value=1e-8)

def rearrangeDataForSDSFile(values,ip,paLen,dim3d):
    """ Linearize gridded data in the right shape for SDS input files

    Arguments:
    values = the array of scalar values to reorganize
    ip = the configuration object which contains the configuration of the interpolation
    paLen = array of SIMION potential array lenghts (one entry per spatial dimension)
    dim3d = flag if we do a 3d interpolation

    Author: Walter Wissdorf
    """
    n = 0

    resVec = np.zeros([paLen[0]*paLen[1]*paLen[2],1])
    for i in range(0,ip['simionPaLimits'][2,1]-ip['simionPaLimits'][2,0]+1):
        for j in range(0,ip['simionPaLimits'][1,1]-ip['simionPaLimits'][1,0]+1):
            for k in range(0,ip['simionPaLimits'][0,1]-ip['simionPaLimits'][0,0]+1):
                resVec[n] = values[k,j,i]
                n=n+1

    print("elements reoganized: "+str(n))
    return(resVec)

def exportSDSParamFilesFromScatteredMesh(ip):
    """exportSDSParamFilesFromScatteredMesh: Exports SIMION / SDS Fluid Flow fields
     from an exported Comsol 4.x solution
       This function transforms a Comsol4 flow field (exported as text file in
       "spreadsheet" notation, which contains the locations of the mesh nodes
       and some dependent values like u,v (velocities in x and y direction))
       to SIMION / SDS Flow field files.

    the main argument is a dictionary (interpolation config "ip")
    with the following fields:

     x= 1st dimension location coordinates
     y= 2nd dimension location coordinates
     z= 3rd dimension location coordinates

     vx= velocity in x direction
```

```
 vy= velocity in y direction
 vz= velocity in z direction

 simionPaLimits = limits of the simion potential array [xmin xmax; ymin ymax]
 shifts = shifts of the SIMION geometry relative to the input Geometry (in simion units)
 scale = scaling factor between comsol solution and simion potential array
   (0.1 means, 1 gridunit in SIMION is converted to 0.1 m in input data)

 cylindricalArray = if == 1 the data is considered as 2dim axi-symmetric
 parameterValue = if this is != 'none' this is considered as variable
   parameter value (like the time of the input data)

 filenameTag = additional tag for the resulting filenames (like a number
   for timedepentend solutions)

   Author: Walter Wissdorf
"""

dims = ip['simionPaLimits'].shape[0]
#get the dimensions from the PA definition

if dims == 3:
    dim3d = True
else:
    dim3d = False

#determine number of elements in the PA for the inidividual dimensions:
paLen = [ip['simionPaLimits'][0,1]-ip['simionPaLimits'][0,0]+1,
         ip['simionPaLimits'][1,1]-ip['simionPaLimits'][1,0]+1,
         ip['simionPaLimits'][2,1]-ip['simionPaLimits'][2,0]+1]
paLen = np.array(paLen)

#create (unscaled) limits of exported area in comsol coordinate system
comLim = np.zeros((3,2))

#upper  limits have +1 because of zero starting indexing in numpy's range
comLim[0,0] = ip['simionPaLimits'][0,0] + ip['shifts'][0]
comLim[0,1] = ip['simionPaLimits'][0,1]+1 + ip['shifts'][0]
comLim[1,0] = ip['simionPaLimits'][1,0] + ip['shifts'][1]
comLim[1,1] = ip['simionPaLimits'][1,1]+1 + ip['shifts'][1]
comLim[2,0] = ip['simionPaLimits'][2,0] + ip['shifts'][2]
comLim[2,1] = ip['simionPaLimits'][2,1] +1 + ip['shifts'][2]

# construct scaled meshgrid (points of the SIMION PA
# Array in the comsolcoordinate system)

# create meshgrids:
qx,qy,qz = np.mgrid[
        comLim[0,0]:comLim[0,1],
        comLim[1,0]:comLim[1,1],
        comLim[2,0]:comLim[2,1]
]

# scale meshgrids:
qxs = qx*ip['scale']
qys = qy*ip['scale']
qzs = qz*ip['scale']

gridpoints = (qxs,qys,qzs)

# construct dimension string for SDS file
if dim3d:
    dimStr = str(paLen[0])+","+str(paLen[1])+","+str(paLen[2])
elif ip['cylindricalArray'] == 1:
    dimStr = str(paLen[0])+","+str(paLen[1])+",0"
else:
    dimStr = str(paLen[0])+","+str(paLen[1])+",1"

print(dimStr)
```

```
# do the interpolation

xi = np.linspace( comLim[0,0]*ip['scale'],
  comLim[0,1]*ip['scale'],comLim[0,1]-comLim[0,0])
yi = np.linspace( comLim[1,0]*ip['scale'],
  comLim[1,1]*ip['scale'],comLim[1,1]-comLim[1,0])
zi = np.linspace( comLim[2,0]*ip['scale'],
  comLim[2,1]*ip['scale'],comLim[2,1]-comLim[2,0])

idata = interpolateData(ip,xi,yi,zi,gridpoints)

# write classic SDS parameter file
print("write vx")
st_vx = "vx_defs.dat"
rivx= rearrangeDataForSDSFile(idata[3],ip,paLen,dim3d)
writeSDSFile(st_vx,dimStr,rivx)
writePAFile('funnel_vx.pa',ip['simionPaLimits'],idata[3],ip['scale'])

print("write vy")
st_vy = "vy_defs.dat"
rivy= rearrangeDataForSDSFile(idata[4],ip,paLen,dim3d)
writeSDSFile(st_vy,dimStr,rivy)
writePAFile('funnel_vy.pa',ip['simionPaLimits'],idata[4],ip['scale'])

print("write vz")
st_vz = "vz_defs.dat"
rivz= rearrangeDataForSDSFile(idata[5],ip,paLen,dim3d)
writeSDSFile(st_vz,dimStr,rivz)
writePAFile('funnel_vz.pa',ip['simionPaLimits'],idata[5],ip['scale'])

print("write Temperature")
st_temp = "temp_defs.dat"
ritemp= rearrangeDataForSDSFile(idata[7],ip,paLen,dim3d)
writeSDSFile(st_temp,dimStr,ritemp)
writePAFile('funnel_t.pa',ip['simionPaLimits'],idata[7],ip['scale'])

print("write Pressure")
st_press = "press_defs.dat"
ripress= rearrangeDataForSDSFile(idata[6],ip,paLen,dim3d)
writeSDSFile(st_press,dimStr,ripress)
writePAFile('funnel_p.pa',ip['simionPaLimits'],idata[6],ip['scale'])

#visualize the interpolated flowfield with matplotlib (for control)
zPlane = 40
yPlane = 40
xPlane = 5

pl.figure()
pl.subplot(1,3,1)
X= qx[:,:,zPlane]
Y= qy[:,:,zPlane]
#V= np.sqrt(ivx[:,:,zPlane]**2 + ivy[:,:,zPlane]**2 + ivz[:,:,zPlane]**2)
V= np.sqrt(idata[3][:,:,zPlane]**2)
pl.contourf(X,Y,V,20)
pl.title("XY")

pl.subplot(1,3,2)
X= qx[:,yPlane,:]
Z= qz[:,yPlane,:]
#V= np.sqrt(ivx[:,yPlane,:]**2 + ivy[:,yPlane,:]**2 + ivz[:,yPlane,:]**2)
V= np.sqrt(idata[3][:,yPlane,:]**2)
pl.contourf(X,Z,V,20)
pl.title("XZ")

pl.subplot(1,3,3)
Y= qy[xPlane,:,:]
Z= qz[xPlane,:,:]
#V= np.sqrt(ivx[xPlane,:,:]**2 + ivy[xPlane,:,:]**2 + ivz[xPlane,:,:]**2)
V= np.sqrt(idata[3][xPlane,:,:]**2)
pl.contourf(Y,Z,V,20)
```

```
    pl.title("YZ")
    pl.show()
```

File: writeSDSFile.py

```
File: writeSDSFile.py
\lstset{language={Python},
                                basicstyle=\ttfamily\tiny,
                                showstringspaces=false,
                keywordstyle=\color{blue},
                stringstyle=\color{red},
                commentstyle=\color{cyan},
                                identifierstyle=\color{gray},
                morecomment=[l][\color{magenta}]{\#}
}
\begin{lstlisting}

import numpy as np
from SIMION.PA import PA
# copy folder "C:\Program Files\SIMION-8.1\lib\python\SIMION" to
# "C:\Python32\Lib\site-packages"
#
#Syntax Error: Except error, e:
#remove parameter "e" -->works

def writeSDSFile(filename,dimStr,vec):
        """  writeSDSFile, exports a vector file for SDS

        Arguments:
        filename: the filename of the SDS file
        dimStr: a string which contains the dimension definition of the
                  file to export
        vec: the datavector

        Author: Walter Wißdorf
        """

        fh = open(filename, 'w')
        fh.write(dimStr+"\n")

        #output is writtend blocked =>
        #1000 elements are blocked and then written to the result file
        output = ""

        # The matlab version contains a check for NaN which is
        # not required here, because the numpy griddata method is able
        # to give any desired value back for "undefined" interpolated
        # values)

        for k in range(1,vec.size):
                output = output + str(float(vec[k]))+"\n"
                #if bufferstring is 1000 lines long => write and flush
                if (k%1000) == 0:
                        #print(k)
                        fh.write(output)
                        output = ""

        #if there is some lines left in the buffer => write them
        if output != "":
                fh.write(output)

        fh.close()

def writePAFile(filename,dim,values,gu_size):
    """  writePAFile, exports a PA file for HS1

        Arguments:
        filename: the filename of the PA file
        dim: contains the dimension in grid units of the export
```

```
    values: the data
gu_size: the size of the simion grid units

    Author: Sascha Albrecht
    """

pa = PA(nx = dim[0,1]-dim[0,0]+1, ny = dim[1,1]-dim[1,0]+1,
  nz = dim[2,1]-dim[2,0]+1, symmetry = 'planar',
  dx_mm = gu_size*1000, dy_mm = gu_size*1000,
  dz_mm = gu_size*1000, fast_adjustable = 0)
for x in range(0, pa.nx()):
    for y in range(0, pa.ny()):
        for z in range(0, pa.nz()):
            pa.potential(x, y, z, values[x,y,z])
pa.save(filename)
print("File ",filename," written: ",pa.header_string())
```

Appendix C

Program code for SDS @ 100 hPa

```
--  SIMION Lua workbench user program for ion funnels.
--

simion.workbench_program()

-- Minimum number of time-steps per waveform period.
-- Overrides T.Qual if non-zero.
adjustable wave_timesteps = 100

-- Period of waveform (usec)
adjustable wave_period = 0.1

-- import standard SDS collision model from this directory.
local SDS = simion.import("collision_sds.lua")

adjustable SDS_faims_mode = 0

--_Use_P_field_scale_factor = 0.0075006375541921

function SDS.temperature(x,y,z) --
  return 295 --K
end

function SDS.pressure(x,y,z) --
  return 75 --Torr
end

-- adjustable during flight

local M = {}
M.segment = {}

adjustable SDS_collision_gas_mass_amu = 28.94515
adjustable SDS_collision_gas_diameter_nm = 0.366

adjustable pe_update_each_usec  = 0.001         -- PE display update period (in usec)

-- adjustable at beginning of flight

adjustable _freqency_hz_min         = 10E6      -- RF frequency of funnel (in Hz)
adjustable _freqency_hz_max         = 10E6      -- RF frequency of funnel (in Hz)
adjustable _freqency_step           = 10E6
                                                --   CAREFUL: time-step sizes should
```

```
                                        -- be some fraction below period.
adjustable phase_angle_deg      = 0.0   -- entry phase angle of ion (deg)
adjustable _RF_amplitude_min        = 100   -- RF peak-to-ground voltage (in V)
adjustable _RF_amplitude_max        = 250   -- RF peak-to-ground voltage (in V)
adjustable _RF_amplitude_step       = 50
adjustable _DC_Gradient_V_min    = 0        -- DC gradient of electrode 1-15 (in V/cm)
adjustable _DC_Gradient_V_max    = 0        -- DC gradient of electrode 1-15 (in V/cm)
adjustable _DC_Gradient_step      = -400


-- internal variables
local freq = _freqency_hz_min           -- rf frequency
local omega  = freq * 6.28318E-6        -- frequency in radians / usec
local theta                             -- phase offset in radians
local last_pe_update = 0.0              -- last potential energy surface update time (usec)
local fh                                -- file for output
local dc = _DC_Gradient_V_min           -- DC Gradient
local rf = _RF_amplitude_min            -- rf amplitude
local x_reached = 0                     -- counter for the ions reaching
                                        --a given position at the end of flight
local rr= 0                             -- data plotted für this run?
local ion_pos_term_x = {}
local ion_pos_term_y = {}
local ion_pos_term_z = {}               -- stores the last position of the ions
local shot = 0

function segment.init_p_values()
   if rr == 1 then

        --plot data of the last run to file
        fh = assert(io.open("Transmission1.txt", "a+"))
        fh:write(x_reached)
        fh:write(' ')
        fh:write(omega / 6.28318E-6)
        fh:write(' ')
        fh:write(dc)
        fh:write(' ')
        fh:write(rf)
        fh:write('\n')
        fh:close()

        freq =( freq + _freqency_step )
        if freq > _freqency_hz_max then
                freq = _freqency_hz_min
                rf = (rf + _RF_amplitude_step)
                if rf > _RF_amplitude_max then
                        rf = _RF_amplitude_min
                        dc = (dc + _DC_Gradient_step)
                        if dc < _DC_Gradient_V_max then
                                rerun = 0
                        end
                end
        end

        print(freq, "Hz ", rf, "Vpp ", dc, "V")
        omega = freq  * 6.28318E-6
        rr=0
        x_reached = 0
   end

ion_pos_term_x = {}
ion_pos_term_y = {}
ion_pos_term_z = {}
end

function segment.fast_adjust()
    -- Initialize constants once.
    if not theta then
          mz = ion_mass
        theta = phase_angle_deg * (3.141592 / 180)
```

```
        omega = freq * 6.28318E-6
        fh = assert(io.open("Transmission1.txt", "a+"))
        fh:write('Transmission[ions] Frequency[Hz] DC-Voltage[V] RF-Amplitude[Vp0]\n')
        fh:close()
        print(freq, "Hz ", rf, "Vpp ", dc, "V")
    end

    ion_pos_term_x[ion_number] = ion_px_mm
    ion_pos_term_y[ion_number] = ion_py_mm
    ion_pos_term_z[ion_number] = ion_pz_mm

    -- Apply RF+DC to each electrode (see README file for explanation).
    adj_elect01 = rf * sin(ion_time_of_flight * omega + theta)
    adj_elect02 = dc  --V/cm
end

function segment.terminate()
-- SIMION terminate segment.  Called on particle termination.
  local pos_y = ion_pos_term_y[ion_number]
  local pos_z = ion_pos_term_z[ion_number]
  pos_y = pos_y - 20
  pos_z = pos_z - 20
  if (ion_pos_term_x[ion_number] > 86) and (pos_y*pos_y+pos_z*pos_z < 15)
      then x_reached=x_reached+1 end
  if rr==0 then rr=1 end
  -- sim_rerun_flym = rerun
end


-- Time-step control.  Must be a sufficiently small fraction
-- of period to fully represent wave form.
function segment.tstep_adjust()
    wave_period = 1E6/freq
    ion_time_step = wave_period / wave_timesteps
end

-- merge segments with any previous ones.
function M.install_segment(newsegment)
  for name,new in pairs(newsegment) do
    local old = segment[name]
    segment[name] = old and (function() old(); new() end) or new
  end
end
M.install_segment(M.segment)

return M
```

Appendix D

Program code for HS1 @ 5 hPa

```
--  SIMION Lua workbench user program for ion funnel.
--

simion.workbench_program()

local HS1 = simion.import "collision_hs1.lua"   -- Import HS1 collision model
local pa_vx = simion.pas:open('funnel_vx.pa')   -- Import velocity in x-direction
local pa_vy = simion.pas:open('funnel_vy.pa')   -- Import velocity in y-direction
local pa_vz = simion.pas:open('funnel_vz.pa')   -- Import velocity in z-direction
local pa_t = simion.pas:open('funnel_t.pa')     -- Import temperature
local pa_p = simion.pas:open('funnel_p.pa')     -- Import pressure

-- adjustable during flight

-- Mass of background gas particle (amu)
adjustable _gas_mass_amu = 28.94515

-- Collision-cross section (m^2)
adjustable _sigma_m2 = 2.27E-18

-- Mean number of time steps per MFP.
adjustable _steps_per_MFP = 50.0

-- Collision marker flag.
adjustable _mark_collisions = 0

adjustable pe_update_each_usec  = 0.05                  -- PE display update period (in usec)

-- adjustable at beginning of flight

adjustable _freqency_hz_min             = 1.8E6         -- RF frequency of funnel (in Hz)
adjustable _freqency_hz_max             = 1.8E6
adjustable _freqency_step               = 5E5
                                                        --   CAREFUL: time-step sizes should
                                                        --   be some fraction below period.
adjustable phase_angle_deg              = 0.0           -- entry phase angle of ion (deg)
adjustable _RF_amplitude_min            = 50            -- RF peak-to-ground voltage (in V)
adjustable _RF_amplitude_max            = 200
adjustable _RF_amplitude_step           = 50
adjustable _DC_Gradient_V_min           = 0             -- DC gradient
adjustable _DC_Gradient_V_max           = 0
adjustable _DC_Gradient_step            = 0


-- internal variables
local freq = _freqency_hz_min                   -- rf frequency
local omega  = freq * 6.28318E-6                -- frequency in radians / usec
```

```
local theta                                     -- phase offset in radians
local last_pe_update = 0.0                      -- last potential energy surface update time (usec)
local fh                                        -- file for output
local dc = _DC_Gradient_V_min                   -- DC Gradient
local rf = _RF_amplitude_min                    -- rf amplitude
local x_reached = 0                             -- counter for the ions reaching a given position at the end of flight
local rr= 0                                     -- data plotted für this run?
local ion_pos_term_x = {}                       -- stores the last position of the ions
local ion_pos_term_y = {}
local ion_pos_term_z = {}
local rerun = 1

function HS1.velocity(x_gu, y_gu, z_gu)         -- Parabolic velocity vector profile.  -- m/s -> mm/usec
return pa_vx:potential(x_gu,y_gu,z_gu)*0.001, pa_vy:potential(x_gu,y_gu,z_gu)*0.001, pa_vz:potential(x_gu,y_gu,z_gu)*0.001
end

function HS1.pressure(x_gu, y_gu, z_gu)         -- Parabolic velocity vector profile.
  return pa_p:potential(x_gu,y_gu,z_gu)         -- in Pa
end

function HS1.temperature(x_gu, y_gu, z_gu)      -- Parabolic velocity vector profile.
  return pa_t:potential(x_gu,y_gu,z_gu)         -- in K
end

function segment.init_p_values()
   if rr == 1 then

        --plot data of the last run to file
        fh = assert(io.open("Transmission1.txt", "a+"))
        fh:write(x_reached)
        fh:write(' ')
        fh:write(omega / 6.28318E-6)
        fh:write(' ')
        fh:write(dc)
        fh:write(' ')
        fh:write(rf)
        fh:write('\n')
        fh:close()

        freq =( freq + _freqency_step )
        if freq > _freqency_hz_max then
                freq = _freqency_hz_min
                rf = (rf + _RF_amplitude_step)
                if rf > _RF_amplitude_max then
                        rf = _RF_amplitude_min
                        dc = (dc + _DC_Gradient_step)
                        if dc < _DC_Gradient_V_max then
                                rerun = 0
                        end
                end
        end

        print(freq, "Hz ", rf, "Vpp ", dc, "V")
        omega = freq  * 6.28318E-6
        rr=0
        x_reached = 0

   end
ion_pos_term_x = {}
ion_pos_term_y = {}
ion_pos_term_z = {}
end

function segment.fast_adjust()
    -- Initialize constants once.
    if not theta then
          mz = ion_mass
        theta = phase_angle_deg * (3.141592 / 180)
        omega = freq * 6.28318E-6
        fh = assert(io.open("Transmission1.txt", "a+"))
```

```
        fh:write('Transmission[ions] Frequency[Hz] DC-Voltage[V] RF-Amplitude[Vp0]\n')
        fh:close()
    end


    ion_pos_term_x[ion_number] = ion_px_mm
    ion_pos_term_y[ion_number] = ion_py_mm
    ion_pos_term_z[ion_number] = ion_pz_mm

    -- Apply RF+DC to each electrode (see README file for explanation).
    adj_elect01 = rf * sin(ion_time_of_flight * omega + theta)
    adj_elect02 = dc  --V/cm

end

function segment.terminate()
-- SIMION terminate segment.  Called on particle termination.
  local pos_y = ion_pos_term_y[ion_number]
  local pos_z = ion_pos_term_z[ion_number]
  pos_y = pos_y - 12.5
  pos_z = pos_z - 12.5
  if (ion_pos_term_x[ion_number] > 64.7) and (pos_y*pos_y+pos_z*pos_z < 5) then x_reached=x_reached+1 end
  if rr==0 then rr=1 end
  sim_rerun_flym = rerun
end

local previous_other_actions = segment.other_actions
function segment.other_actions()
    -- Run previously defined segment.
    previous_other_actions()

    -- Update PE surface display.
    if abs(ion_time_of_flight - last_pe_update) >= pe_update_each_usec then
        last_pe_update = ion_time_of_flight
        sim_update_pe_surface = 1    -- Request a PE surface display update.
    end
end
```

Appendix E

Images

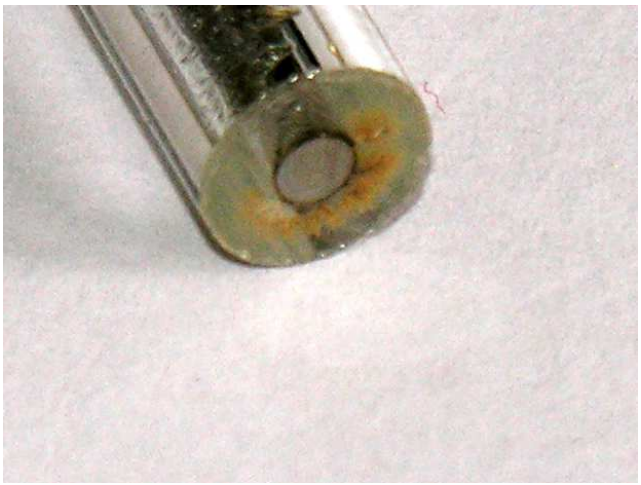

Figure E.1: Photograph of the first version of the DBD electrode with the dielectric window (silica glass) glued onto the high voltage electrode, the formation of brown palls after less than 10 h of operation demonstrates evidence of a secondary plasma eroding the glue between the dielectric window and the high voltage electrode.

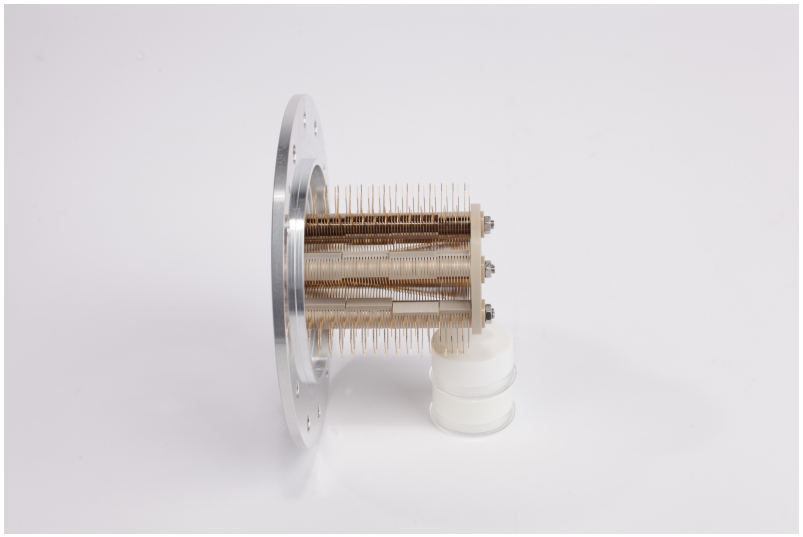

Figure E.2: Photograph of the 100 hPa ion funnel before the printed circuit boards are attached.

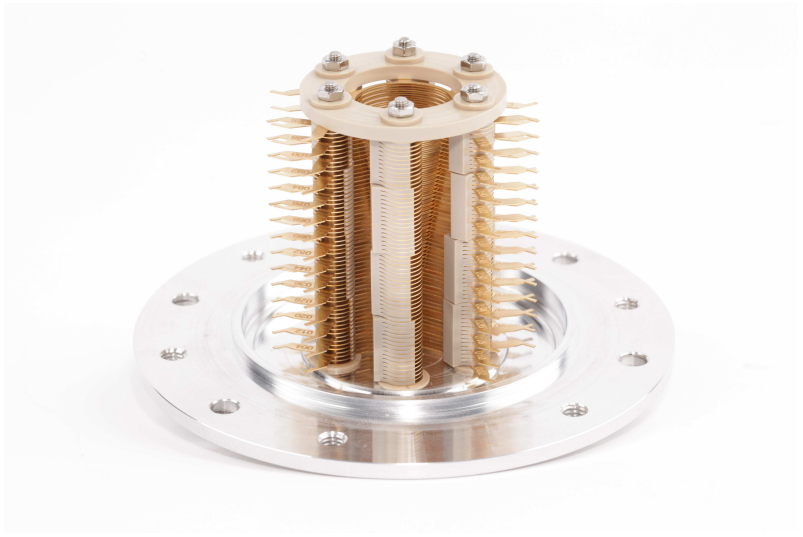

Figure E.3: Photograph of the 100 hPa ion funnel before the printed circuit boards are attached.

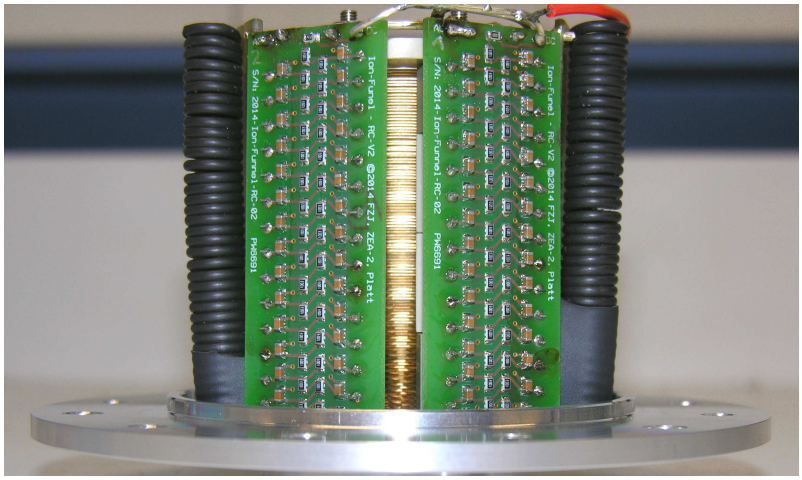

Figure E.4: Photograph of the 100 hPa ion funnel with the printed circuit boards attached.